

Diss. ETH Nr. 17653

Experimental Investigation and Population Balance Modeling of Aggregation and Breakage of Polymer Colloids in Turbulent Flow

A dissertation submitted to
THE SWISS FEDERAL INSTITUTE OF TECHNOLOGY ZURICH
ETH ZURICH

For the degree of
Doctor of Sciences
Dr. Sc. ETH Zürich

Presented by
Amgad Salah Moussa
B.Eng. (Honours), Chemical Engineering, Cairo University, Egypt, 2000
DEA, Chemical Engineering, Rovira i Virgili University, Spain, 2003
Born on the 29th of June 1978
Citizen of Egypt

Accepted on the recommendation of
Prof. Dr. Massimo Morbidelli, supervisor and examiner
Prof. Dr. Wendelin Jan Stark, co-examiner

Zurich 2008

بِسْمِ اللّٰهِ الرَّحْمٰنِ الرَّحِیْمِ

Dedication

*To my parents for encouraging and nurturing my curiosity and
to Samira for making life so pleasant*

Abstract

The focus of this thesis is to provide deeper understanding of flow-induced aggregation of dilute colloidal suspensions and other processes that accompany it, i.e., breakage of aggregates. For this purpose we designed an experimental setup where aggregation in a stirred tank (the coagulator) is monitored on-line using small angle static light scattering (SASLS). From SASLS measurements we obtain two independent moments of the cluster mass distribution (CMD) as well as information about the aggregate structure. Furthermore, our experimental setup allows for the introduction of controlled stimuli in the rotation speed and solid volume fraction to the coagulator. In all studies, surfactant-free polystyrene latex particles were used as a model system because polystyrene has a specific gravity of 1.05, which allows us to isolate flow-induced aggregation from aggregation due to differential settling. Moreover, solid recovery from polymer latexes is one of the most important industrial processes where flow-induced aggregation is the centrepiece. This makes understanding of flow-induced aggregation of polymer colloids very valuable and industrially relevant. Throughout this thesis, we considered only aggregation at salt concentration above the critical coagulation concentration (CCC).

In the first part we focused on the effect of the solid volume fraction on flow induced aggregation and breakage. This allowed us to elucidate the mechanism behind the attainment of a steady state CMD. The experiments showed that the steady state CMD in the system studied is controlled by dynamic equilibrium between aggregation (with second order kinetics in cluster concentration) and breakage (with first order kinetics in cluster concentration). The reversibility of this equilibrium was verified and later exploited to collect data about the dependency of the steady state CMD over a range of solid volume fraction in one experiment. This was done by diluting the coagulator after steady state CMD is attained. The rate of dilution was designed using time scale analysis to be slow enough such that equilibrium is maintained throughout the dilution. It was observed that the aggregate size reached an asymptotic value during this dilution, below which breakage is negligible. The existence of such a critical size is an important aspect of the breakage phenomenon that must be taken into account in any models of breakage rate.

In the second part the effect of the rotation speed, i.e., the volume average shear rate, G , on size and structure of the aggregates was investigated, as well as the response of the CMD to different stimuli in the shear rate. For this purpose, batch and dilution experiments were conducted at various values of the rotation speed. Detailed investigation of the initial kinetics

obtained from these experiments showed that the aggregation efficiency α depends on the shear rate according to $\alpha \propto G^{-n}$ with n equal to 0.18 in agreement with theoretical consideration. Moreover, it was found that the radius of gyration at steady state and that at infinite dilution scale with the shear rate with a power law exponent equal to -0.5. From these measurements we estimated the cohesive forces holding the aggregate together by assuming it to be equal to the hydrodynamic forces acting on aggregates having the critical aggregate size obtained via the dilution experiments. This force balance gave values independent of the aggregate size and equal to 6.2 ± 1 nN, in agreement with the literature data using micromanipulation approach. Further, response of the CMD to ramp and step changes in the rotation speed was also studied. It was found that the steady-state values of both measured moments of the CMD are fully reversible upon changing the stirring speed. In contrast to the shear-rate dependency of the steady-state values of the CMD moments, assessment of the aggregate structure by SASLS and image analysis using confocal laser scanning microscopy showed the aggregate structure to be independent of the applied shear rate, with values of the fractal dimension, d_f , equal to 2.62 ± 0.18 , in the studied range of stirring speeds.

In the third part we address the influence of the surface chemistry of the latex particles on flow-induced aggregation and breakage. We studied the influence of two surface attributes (i) the degree of ionization of surface groups and (ii) the area per charge groups. The first attribute was studied by carrying out aggregation experiments using carboxyl latexes at various pH values at salt concentration well above the CCC; in a fixed flow field and with the same solid volume fraction. The second attribute was studied by using latexes with various areas per charge group. Three remarkable observations were made: (i) for the same size of primary particles, initial kinetics is not affected by the different surface chemistry of used particles, (ii) qualitatively different behaviors of the temporal evolution of moments of the CMD were observed below certain pH values with ability of full-grown aggregates to respond to the variation of pH and (iii) aggregates sizes are mainly controlled by the surface chemistry of primary particles and not by their size. Based on our measurements and data in literature we concluded that structural forces (non-DLVO) and contact hysteresis play an important role in flow-induced aggregation and breakage above the CCC.

In the last part, we evaluated the suitability of different models of aggregation efficiency to model flow-induced aggregation of colloidal dispersions within the framework of the

population balance equation (PBE). This evaluation is done by comparing models' predictions and experimental data. The experimental data were collected from two kinds of experiments: initial aggregation of primary particles, and regrowth of pre-formed aggregates. The obtained data for various values of applied shear rate and primary particle size were used to evaluate the performance of four aggregation efficiency models: rectilinear model, curvilinear model, core-shell (CS) model, and uniformly permeable sphere (UPS) model, in addition to the empirical fitting of uniform aggregation efficiency. It was found that only the UPS model was able to predict the experimental data of both kinds of experiments.

Zusammenfassung

Die Zielsetzung dieser Doktorarbeit ist es ein tieferes Verständnis der strömungsinduzierten Aggregation verdünnter kolloidaler Dispersionen und damit einhergehenden Prozessen, wie z. B. dem Brechen von Aggregaten, zu schaffen. Für diesen Zweck haben wir einen experimentellen Aufbau entwickelt welcher die Durchführung von Aggregationsprozessen in einem Rührkessel (Koagulationseinheit) und deren Online-Beobachtung mittels statischer Kleinwinkel-Lichtstreuung ermöglicht. Die Messungen mittels statischer Kleinwinkel-Lichtstreuung liefern uns zwei unabhängige Momente der Aggregatgrößenverteilung sowie Informationen über die Aggregatstruktur. Des Weiteren gewährleistet der experimenteller Aufbau die genaue Kontrolle der Prozessvariablen Umdrehungszahl und Feststoffanteil. In allen Studien wurden als Modellsysteme tensidfreie Polystyrolpartikel verwendet, da diese eine spezifische Dichte von 1.05 besitzen (in Bezug auf Wasser) und uns somit ermöglicht ausschliesslich strömungsinduzierte Aggregation zu untersuchen, unter Vernachlässigung von Aggregation durch differentielle Sedimentation. Zudem ist die Feststoffrückgewinnung aus Kunststofflatexen einer der wichtigsten industriellen Prozesse mit der strömungsinduzierte Aggregation als Schlüsselschritt. Daher ist ein Verständnis der strömungsinduzierten Aggregation von polymeren Kolloiden wertvoll und von industrieller Relevanz. In dieser Arbeit untersuchen wird durchweg Aggregation bei Salzkonzentrationen überhalb der kritischen Koagulationskonzentration.

Im ersten Teil konzentrieren wir uns auf den Effekt des Feststoffanteils auf die durch Strömung induzierten Prozesse Aggregation und Bruch. Dies ermöglicht uns zu erläutern welche Mechanismen dem Erreichen einer stationären Aggregatgrößenverteilung zugrunde liegen. Die Experimente zeigen, dass im untersuchten System die stationäre Aggregatgrößenverteilung von einem dynamischen Gleichgewicht zwischen Aggregation (mit einer Kinetik zweiter Ordnung in Bezug auf die Aggregatkonzentration) und Bruch (mit einer Kinetik erster Ordnung in Bezug auf die Aggregatkonzentration) bestimmt wird. Nachdem die Reversibilität dieser Gleichgewichtszustände verifiziert wurde hat man diese ausgenutzt um Daten über die Abhängigkeit der Aggregatgrößenverteilung über einen weiten Bereich des Feststoffanteils vermittels eines einzigen Experimentes zu erhalten. Dies geschah indem man die Dispersions in der Koagulationseinheit nach Erreichen des Gleichgewichtszustandes verdünnte. Die Verdünnungsrate wurde durch eine Zeitskalenanalyse ermittelt und niedrige genug angesetzt,

sodass der Gleichgewichtszustand in Bezug auf die Aggregatgrößenverteilung während des Verdünnens zu jederzeit gewährleistet war. Dabei wurde beobachtet, dass sich die Aggregatgröße während des Verdünnens einem Wert, unter welchem Bruch vernachlässigbar ist, asymptotisch annähert. Die Existenz einer solchen kritischen Aggregatgröße ist ein wichtiger Aspekt des Bruchvorgangs und muss bei der Modellierung desselben berücksichtigt werden.

Im zweiten Teil wird die Auswirkung der Rührgeschwindigkeit, und damit der volumengemittelten Scherrate, G , auf die Größe und Struktur der Aggregate untersucht, sowie die Reaktion der Aggregatgrößenverteilung auf unterschiedliche Arten der Scherratenänderung. Zu diesem Zweck wurden Experimente im Batch-Verfahren und unter Verdünnung für verschiedene Rührgeschwindigkeiten durchgeführt. Ausführliche Untersuchung der durch diese Experimente erhaltenen Anfangskinetik zeigen, dass der Wirkungsgrad für Aggregation, α , proportional ist zu einer Potenz der volumengemittelten Scherrate gemäss $\alpha \propto G^{-n}$, mit einem n von 0.18, in Übereinstimmung mit theoretischen Betrachtungen. Ferner wurde beobachtet, dass im Gleichgewichtszustand der Trägheitsradius proportional ist zur Potenz der volumengemittelten Scherrate mit dem Exponenten gleich -0.5, dies sowohl bei angemessenen Feststoffanteil als auch unter höchster Verdünnung. Aufgrund dieser Messungen schätzten wir die Kohäsionskraft welche die Aggregate zusammenhält ab, indem wir annahmen, dass sie der hydrodynamischen Kraft welche auf Aggregate von kritischer Größe wirkt entspricht, wobei die kritische Aggregatgröße durch Verdünnungsexperimente ermittelt wurde. Aus diesem Vergleich ergibt sich eine von der Aggregatgröße unabhängige Kohäsionskraft gleich 6.2 ± 1 nN, in Übereinstimmung mit durch die Methode der Mikromanipulation erhaltenen Literaturwerten. Des Weiteren wurde die Reaktion der Aggregatgrößenverteilung auf lineare und stufenweise Veränderungen der Rührgeschwindigkeit untersucht. Dabei wurde festgestellt, dass die stationären Zustandswerte beider gemessenen Momente der Aggregatgrößenverteilung vollständig reversibel gegenüber einer Veränderung der Rührgeschwindigkeit sind. Im Gegensatz zu den von der Scherrate abhängigen Momenten der Aggregatgrößenverteilung zeigte eine Bestimmung der Aggregatstruktur mittels statischer Kleinwinkel-Lichtstreuung und Bildanalyse mit Hilfe konfokaler Laser-Raster-Mikroskopie eine von der Scherrate unabhängige Aggregatstruktur mit einer fraktalen Dimension, d_f , gleich 2.62 ± 0.18 (gültig im Bereich der untersuchten Rührgeschwindigkeiten).

Im dritten Teil adressieren wir den Einfluss der Oberflächenchemie der Latex Partikel. Wir untersuchten den Einfluss zweier Oberflächenmerkmale (i) den Ionisierungsgrad der Oberflächengruppen und (ii) die jeder Ladungsgruppe zur Verfügung stehende Fläche. Das erste Merkmal wurde in einer Reihe von Aggregationsexperimenten untersucht, wobei Carboxyllatexe verwendet wurden, bei verschiedenen pH-Werten, mit Salzkonzentrationen weit überhalb der kritischen Koagulationskonzentration, in einem bestimmten Strömungszustand und bei gleichem Feststoffanteil. Um das zweite Merkmal zu untersuchen wurden Latexe mit pro Ladungsgruppe zur Verfügung stehender Fläche unterschiedlicher Grösse verwendet. Drei nennenswerte Beobachtungen wurden gemacht: (i) die Anfangskinetik wird nicht durch die Unterschiede der Oberflächenchemie der Partikel beeinflusst, (ii) unterhalb bestimmter pH-Werte wurde qualitativ unterschiedliches Verhalten der zeitlichen Entwicklung der Momente der Aggregatgrößenverteilung beobachtet, wobei ausgewachsene Aggregate auf eine Änderung des pH-Wertes reagieren und (iii) die Aggregatgrösse wird hauptsächlich durch die Oberflächenchemie der Primärpartikel bestimmt und nicht durch deren Grösse. Aufgrund unserer Messungen und Literaturdaten stellen wir fest, dass strukturelle Kräfte und Kontakthysterese eine wichtige Rolle in den strömungsinduzierten Prozessen Aggregation und Bruch einnehmen, selbst bei Salzkonzentrationen überhalb der kritischen Koagulationskonzentration.

Im letzten Teil bewerten wir unterschiedliche Modelle zur Berechnung des Wirkungsgrads für Aggregation in Hinsicht auf ihre Eignung zur Simulation strömungsinduzierter Aggregation kolloider Dispersionen mit Hilfe von Populationsbilanzen. Die Auswertung erfolgt durch einen Vergleich der verschiedenen Modellvorhersagen mit experimentellen Daten. Die experimentellen Daten stammen von Versuchen zweierlei Art: Anfangskinetik von Primärpartikeln und erneutes Wachstum von schon gebildeten Aggregaten. Die auf diese Weise, für verschiedene Werte der volumengemittelten Scherrate und der Primärpartikelgrösse, erhaltenen Daten wurden verwendet um die Tauglichkeit vierer Modelle zur Berechnung des Wirkungsgrades für Aggregation zu evaluieren: geradliniges Modell, krummliniges Modell, Kern-Schalen-Modell und Modell gleichmässig permeabler Kugeln. Zusätzlich wurde die Simulation mittels eines empirisch angepassten gleichmässigen Wirkungsgrad für Aggregation in den Vergleich mit einbezogen. Dabei stellte man fest, dass allein Simulation mit dem Modell gleichmässig permeabler Kugeln die experimentellen Daten beider Versuchsarten beschreiben können.

Résumé

Le but de cette thèse est de fournir une explication profonde de l'agrégation induite par écoulement de suspensions colloïdales diluées ainsi que d'autres processus l'accompagnant, à savoir, la rupture des agrégats en dilution. A cet effet, nous avons conçu un dispositif expérimental selon lequel l'agrégation dans un mélangeur agité (le coagulateur) est suivie en ligne en utilisant la diffusion statique de la lumière aux bas angles (SASLS). A partir de mesures SASLS, nous obtenons deux moments indépendants de la distribution massique des amas (Cluster mass distribution- CMD) ainsi que de l'information sur la structure des agrégats. Notre dispositif expérimental permet, par ailleurs, l'introduction de stimuli contrôlés en vitesse de rotation et en fraction de volume du coagulateur. Dans toutes les études réalisées, les particules de latex de polystyrène sans surfactant sont utilisées comme un système modèle puisque le polystyrène a une densité spécifique de 1,05 qui permet d'isoler l'agrégation par écoulement induit de l'agrégation due au dépôt différentiel. D'autre part, la récupération du solide à partir des polymères de latex est l'un des procédés industriels les plus importants où l'agrégation par écoulement induit est l'opération centrale. Ce qui fait que la compréhension de l'agrégation par écoulement induit de polymères colloïdaux soit assez valorisée et pertinente pour l'industrie. Tout au long de cette thèse, nous avons considéré uniquement l'agrégation à une concentration de sel en dessus de la concentration critique de coagulation (CCC).

Dans la première partie, nous nous intéressons à l'effet de la fraction de volume du solide sur l'agrégation par écoulement induit et la rupture. Ceci nous a permis d'élucider le mécanisme qui mène à un état permanent CMD. Les expériences ont montré que l'état permanent CMD au sein du système étudié est régi par un équilibre dynamique entre l'agrégation (avec une concentration de l'amas au second ordre cinétique) et la rupture (avec une concentration de l'amas au premier ordre cinétique). La réversibilité de cet équilibre a été vérifiée et exploitée ultérieurement pour recueillir des données sur la dépendance du CMD sur tout un intervalle de la fraction de volume en une seule expérience. Ceci a été réalisé en diluant le coagulateur après que l'état permanent CMD soit atteint. Le taux de dilution a été déterminé en utilisant l'analyse des échelles de temps pour qu'elle soit suffisamment lente de manière à ce que l'équilibre soit maintenu à travers la dilution. Il a été observé que la dimension de l'agrégat atteignait, durant cette dilution, une valeur asymptotique en dessous de laquelle la rupture est négligeable.

L'existence d'une telle dimension critique est un aspect important du phénomène de rupture qui doit être pris en considération dans tout modèle de rupture.

Dans la deuxième partie, nous étudions l'effet de la vitesse de rotation, i.e. la vitesse de cisaillement par volume moyen, G , sur la structure des agrégats, ainsi que la réponse du CMD à différents stimuli en vitesse de cisaillement. A cet effet, des expériences en batch et en dilution ont été menées à différentes valeurs de vitesse de rotation. Une investigation détaillée de la cinétique initiale obtenue à partir de ces expériences a montré que l'efficacité de l'agrégation α dépend de la vitesse de cisaillement soit, $\alpha \propto G^{-n}$ où n est égal à 0,18, en accord avec les considérations théoriques. D'autre part, on a trouvé que le rayon de giration, à l'état permanent et à dilution infinie, est proportionnelle à la vitesse de cisaillement à la puissance -0,5. A partir de ces mesures, nous avons estimé les forces cohésives qui maintiennent l'agrégat en supposant qu'elles soient égales aux forces hydrodynamiques qui agissent sur l'agrégat ; la dimension critique de l'agrégat étant obtenue à partir des expériences en dilution. Ce bilan de forces a fournit des valeurs indépendantes de la dimension de l'agrégat et qui sont égales à $6,2 \pm 1$ nN, en accord avec les données de la littérature utilisant l'approche de micromanipulation. Ensuite, on a étudié la réponse du CMD aux changements de rampe et de pas dans la vitesse de rotation. Nous avons obtenu que les valeurs à l'état permanent des deux moments mesurés du CMD sont totalement réversibles suite au changement de la vitesse d'agitation. Ce qui indique que même si les moments de CMD à l'état permanent dépendent de la vitesse de cisaillement appliquée, la structure de l'agrégat est indépendante de la vitesse de cisaillement dans l'intervalle des vitesses d'agitation. Contrairement à la dépendance des valeurs des moments de CMD à l'état permanent, l'évaluation de la structure des agrégats par SASLS et traitement d'image utilisant la microscopie confocale à balayage laser (CLMS), a montré que la structure des agrégats est indépendante de la vitesse de cisaillement appliquée, avec des valeurs de dimension fractale, d_f , égales à $2,62 \pm 0,18$, pour l'intervalle des vitesses d'agitation étudié.

Dans la troisième partie, nous abordons l'influence de la composition chimique de surface des particules de latex. Ainsi nous avons étudié l'influence de deux caractéristiques de la surface : (i) le degré d'ionisation des groupes de surface et (ii) la superficie par groupes de charge. La première caractéristique est étudiée en réalisant des expériences d'agrégation utilisant des latex de carboxyle à différents pH et à une concentration de sel largement en dessus du CCC, dans un champ d'écoulement fixe et avec la même fraction de volume du solide. La deuxième

caractéristique est étudiée en utilisant des latex avec différentes superficies par groupe de charge. Trois observations remarquables ont été faites : (i) pour la même dimension de particules primaires, la cinétique initiale n'est pas affectée par les différentes compositions chimiques de surface des particules utilisées ; (ii) on a observé des comportements qualitativement différents de l'évolution temporelle des moments du CMD en dessous de certaines valeurs de pH avec une capacité d'agrégats pleinement épanouis pour répondre aux variations de pH et (iii) les dimensions des agrégats sont contrôlés essentiellement par la composition chimique de surface des particules primaires et non pas par leur dimension. En nous basant sur nos mesures et les données de la littérature, nous avons conclu que les forces de structure et l'hystérésis de contact jouent un rôle important dans l'agrégation par écoulement induit et la rupture en dessus du CCC.

Dans la dernière partie, nous évaluons compatibilité de différents modèles de l'efficacité de l'agrégation avec un modèle d'agrégation par écoulement induit de dispersions colloïdales dans le cadre de l'équation du bilan de population (population balance equation : PBE). Cette évaluation est réalisée en comparant des modèles de prédiction et des données expérimentales. Les données expérimentales ont été collectées à partir de deux types d'expériences : l'agrégation initiale de particules primaires, et la repousse d'agrégats préformés. Les données obtenues à différentes valeurs de la vitesse de cisaillement appliquée et de la dimension des particules primaires ont été utilisées pour évaluer la performance de quatre modèles d'efficacité de l'agrégation : le modèle rectiligne, le modèle curvilinéaire, le modèle core-shell (CS) et le modèle de sphère perméable (UPS) ; en plus de la compatibilité empirique de l'efficacité de l'agrégation uniforme. Nous avons trouvé que seul le modèle UPS était capable de prédire les données expérimentales des deux types d'expériences.

Acknowledgment

Some theses are results of solitary work; this thesis is not one of them, for the importance of Dr. Miroslav Šoóš continuous support to me in its coming into being. Thanks Miro. Other colleagues also contributed to my scientific development and production during the last four years. Dr. Matthäus Ulrich Bähler, the first one to discuss the basics of population balances with me on my first week in the ETH. Sharing the same office for the last two and half years with him was a wonderful opportunity to exchange many interesting conversations about almost everything, in particular science. I learned many things in these conversations, thanks The. I owe my lab mate Lyonel Ehrl sincere thanks for his rigor and German attention to details, which were vital to the functionality of the laboratory and the progress of experiments. Thanks Lyo, I agree with you *Ordnung muss sein*. Dr. Marco Lattuada with his clear clarifications and permanently open door saved me considerable struggles with tiny, yet thorny, issues. Thanks Marco. I cannot also forget Prof. Jan Sefcik efforts to push me in the field of colloids at the beginning of my work. Thanks, Jan.

Other members in the colloids team played an important role in making life enjoyable. I shall not forget the trip to the wild west courtesy of Cornelius Gaur neither shall I forget the Sola races captained by him, especially the one under the deluge, nor the rafting trip in the scenery Engadin. Thanks Corni for energizing the atmosphere. A perfect contrasting companion to these activities was the intellectual conversations with Alessio Zaccone, a professor in the making. Thanks Alessio for interesting discussions in the Technology room, near lac Léman, and around some of the most palatable indulgences I ever had. The honorable yoga master, Yogesh Harshe, with whom I shared the office in the last few months, deserves also a thank you for keeping the office a nice place to work and opening a window to the incredible India in HCI.

Another person from whom I learned was Dr. Zichen Jia. He taught with example how to be patient, serious and serene. He was with me in the most difficult day in the lab; I still keep pieces of that day's experiment. Thanks Zichen for your appropriate reactions. Another due thanks is to Dr. Hua Wu who gave me the opportunity to work with the students in the final year laboratory. I learned a lot from this experience, Thanks Hua. The two BSc students who did their BSc projects with me, Nathalie Casas and Dirk Mohn, also contributed to my experiences in the ETH. Thanks Nathalie and Dirk for giving me the enriching experience of advising you.

I am grateful for the overall friendly atmosphere of the whole group thanks to all the members especially the heart of the group Frau Christine Missak. You are all genuinely wonderful persons.

Saving the most important to the last, a big saluti e grazie to the Capitan of the ever-progressing ship, Professor Massimo Morbidelli, who let me enter this magnificent school and supported me in my not-so-smooth start. He is a living evidence that the leadership genes of the shrewd Roman generals are still well preserved and are yet better employed. Thanks Professor for being a skillful scientist and a benevolent boss.

Table of contents	
Abstract	5
Zusammenfassung	8
Résumé	11
Acknowledgment	14
Table of contents	15
1. Introduction	18
1.1. Motivation to study flow-induced aggregation	18
1.2. Outline of the thesis	19
1.3. Basics of modelling aggregation rate and aggregate structure	22
2. Experimental and measurement setup and methods	25
2.1. Equipment and materials	25
2.2. Experiment procedure	28
2.3. Measurement and characterization techniques	29
2.3.1. Small angle static light scattering (SASLS)	29
2.3.2. Connection between SASLS and moments of the CMD	31
2.3.3. Confocal scanning laser microscopy (CSLM) and image analysis	35
2.4. Tests and Validation	37
2.4.1. Effects of multiple light scattering	37
2.4.2. Validity of estimates of CMD moments based on the Guinier approximation	39
2.4.3. Validation of the on-line recirculation technique	41
2.4.4. Effect of deposition	45
2.5. Summary of CFD description of the stirred tank coagulator	47
3. Effect of solid volume fraction	49
3.1. Introduction and literature review	49
3.2. Batch experiments	51
3.3. Development and validation of the dilution experiment	55

3.3.1. Time scale analysis	55
3.3.2. Experimental validation	57
3.4. Critical aggregate size	65
3.5. Conclusions and summary	68
4. Effect of shear rate	69
4.1. Introduction	69
4.2. Batch experiments and aggregation efficiency	69
4.3. Analysis of aggregate structure	79
4.4. Dilution experiments and critical aggregate size	85
4.4.1. Force balance and estimation of Aggregate cohesive force	85
4.5. System response to the step and ramp changes in the stirring speed	89
4.6. Scaling of moment of the steady state CMD with shear rate	94
4.7. Conclusions and summary	97
5. Surface chemistry effects	99
5.1. Introduction and motivation	99
5.2. Materials and Equipment	100
5.3. Dependency of the CMD on the pH	102
5.4. Phenomena leading to the overshoot	113
5.5. Conclusions and summary	121
6. Comparison and experimental validation of aggregation efficiency models	122
6.1. Introduction	122
6.2. Aggregation efficiency models	123
6.2.1. Rectilinear model and empirical fitting of a scalar efficiency	123
6.2.2. Curvilinear model	124
6.2.3. Core-shell model	125

6.2.4. Uniformly permeable sphere model	126
6.3. Comparison with experiments	126
6.3.1. Initial aggregation experiments	129
6.3.2. Regrowth experiments	135
6.4. Conclusions and summary	141
7. Conclusions	142
References	144
CURRICULUM VITAE	151

1. Introduction

1.1. Motivation to study flow-induced aggregation

Colloidal dispersions are multiphase mixtures where one of the characteristic dimensions of the dispersed phase is between 1 nanometre and 1 micrometer. A subclass of these dispersions is aqueous colloidal suspensions, referred to hereafter as suspensions, where the continuous medium is water and the dispersed phase consists of spherical solid particles. Flowing suspensions can be found in a myriad of natural and artificial systems. Rivers, lakes and estuaries are examples of natural systems where flowing suspensions are encountered. In the chemical and allied industries flowing suspensions are at the core of commonplace unit operations and processes such as flocculation, emulsion and suspension polymerizations, and crystallization, to name a few. The first of these operations, flocculation, is the workhorse of the water/wastewater treatment and an essential step in the post-processing of suspensions from emulsion and suspension polymerization reactors. The purpose of this operation is to aggregate the submicron particles in the suspension to clusters that can be subsequently separated in hydrocyclones, settlers, filters, and other solid-liquid separation operations. Fig. 1.1 illustrates a typical flowsheet for solid/liquid separation in water treatment plants¹. The effectiveness of the solid recovery operations subsequent to flocculation depends on the cluster mass distribution (CMD) and the structure of the aggregates produced, which in turn are governed by aggregation phenomena. Besides its crucial role in the flocculation operations, aggregation also influences the performance of crystallizers, and suspension and emulsion polymerization reactors. Therefore, considerable research effort has been, and is being, dedicated to understanding and controlling aggregation in flowing suspensions.

Aggregation in flowing suspensions is partly due to Brownian motion, referred to as Brownian aggregation or perikinetic aggregation, and partly induced by the flow, referred to as flow-induced aggregation, orthokinetic aggregation or shear aggregation interchangeably. Aggregation due to differential settlings is relevant only for large particles and aggregates of materials significantly denser than the suspending fluid^{1, 2}, thus it does not play a significant role in the suspension studied in this work. Moreover, most of the solid-liquid separation operations are effective only when the sizes of the solid phase exceed 5 micrometers³. Notably, with the

increase in aggregate sizes outside the submicron range shear aggregation dominates the evolution of the CMD and overshadows Brownian aggregation¹². In other words, shear aggregation governs most of aggregation processes of industrial importance since aggregates much larger than one micrometer are required.

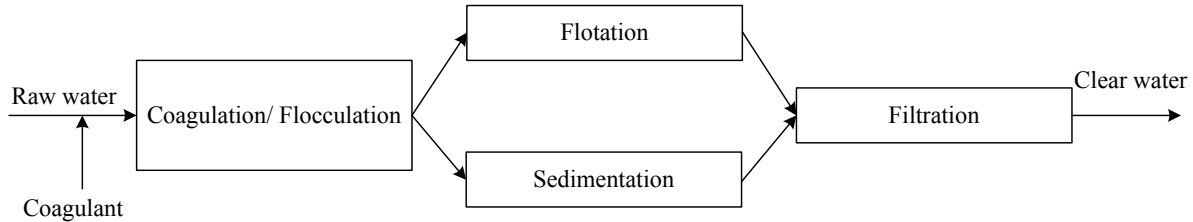


Figure 1.1: Typical flowsheet for particle separation in a water treatment plant¹. In some cases, solid-liquid separation takes place along with flocculation in the same equipment by gravity or by blowing air bubbles in the aggregating suspension and skimming the resulting froth.

Despite the importance of shear aggregation phenomena and its prevalence in many industrial processes, our current level of understanding of shear aggregation is still lacking, especially in comparison with our understanding of Brownian aggregation. This is due to the additional complexity introduced by the fluid flow and other phenomena that can take place only in flow such as breakage of aggregates. Additionally, in industrial units the flow is most frequently turbulent, to foster rates of transport phenomena, and almost invariably heterogeneous, due to spatial variations of the velocity gradients. Breakage, turbulence, and flow field heterogeneity add to the complexity of flow-induced aggregation and make it an outstanding problem that nevertheless must be tackled.

1.2. Outline of the thesis

The focus of this thesis is to provide deeper understanding of the shear aggregation phenomenon and other phenomena that accompany it and influence the CMD. For this purpose we had to impose four constraints on the systems object of study to reduce the effects of other

¹ The relative importance of Brownian and shear aggregation can be assessed by calculating the ratio between the rate constants $G\mu d^3/2k_B T$, where G is the velocity gradient, μ is the viscosity, k_B is Boltzmann's constant, T the temperature and d the characteristic aggregate size, note that this ratio increases with the size to power 3.

phenomena such as settling, and to facilitate system characterization. The constraints and the rationale behind them are explained in the following paragraphs.

First, the solid volume fraction was chosen to be low enough to allow for the use of light scattering on-line with little or no effects of multiple scattering. Light scattering was selected because it is a non-invasive particle characterization technique that gives reliable and extensive information about the CMD and the structure of aggregate. On-line characterization of the CMD enables us to study the dynamic response more closely. Another reason for focusing on dilute systems is that the aggregation rate in concentrated systems is so fast such that resolving aggregation dynamics before gelation is unfeasible.

Second, polystyrene latex was used as a model material since its specific gravity is close to unity, thus settling and aggregation due to differential settling of different aggregate sizes can be neglected². The existence of these two phenomena would confound any inferences we make about shear aggregation influence on the CMD, thus they ought to be avoided.

Third, the latex used was surfactant-free to make sure that phenomena like micelle formation and depletion flocculation do not influence our system. Moreover, only coagulation by the addition of inorganic salts, namely Al (NO₃)₃ and MgCl₂ were considered. The amount of salt added was many times that required to reach the critical coagulation concentration (CCC) for the latexes used. This was done to make sure that electrostatic forces are screened so that only attractive forces prevail between the particles⁴. Furthermore, other coagulants that might precipitate and enmesh the particles, e.g. polyaluminium chlorides and alum, or polymer flocculants that might degrade and change under shear were not considered.

Finally, the flow field was fixed in all studies to a stirred tank in turbulent flow regime. The geometry was selected because the stirred tank is arguably the most common piece of equipment that handles suspensions in the process industry, therefore the influences of the flow field heterogeneity in it on flow-induced aggregation should be considered. Furthermore, most flows of industrial importance, as well as natural flows are turbulent.

² The effect of particle inertia can be neglected when Stokes number $St = t_p G \ll 1$, where

$t_p = R^2 \left(\frac{2\rho_p}{\rho_f} + 1 \right) / 9\nu$, is the particle relaxation time, and ρ_p and ρ_f are the density of the aggregate and the surrounding fluid, respectively

Within the framework outlined above, we conducted the four studies presented in this thesis. First, we studied the effects of the solid volume fraction (ϕ) on the temporal evolution of sizes and the steady state CMD. This study allowed us to elucidate the breakage mechanism for the system at hand, which is necessary for any model of the breakage rate. Then we devised an efficient technique for measuring the dependency of the steady state CMD on a wide range of ϕ values in one experiment by continuous dilution after attainment of the steady state. We estimated the feasible dilution rate by time scale analysis, and experimentally validated the whole concept of dilution experiments as a mean to obtain steady state CMD as a function of ϕ . Additionally, we found out that we can assess the critical aggregate sizes below which breakage is negligible by continuously diluting the system until infinitesimally small values of ϕ . This study is presented in chapter three. Second we studied the effects of the rotation speed, i.e., shear rate (G), in both batch and dilution experiments. In this second study, we examined closely aggregates structure using two different techniques: light scattering, and confocal microscopy and compared the results of both. We also analyzed the dependency of the critical aggregate sizes on the shear rate to assess the forces required to rupture the aggregates, i.e., aggregate cohesive force. Chapter 4 is an account of this study. After detailed investigation of these two physical parameters (G and ϕ) we shifted our attention to the effects of the chemical composition of the medium and the particles' surface in the study presented in chapter 5. Studies of surface chemistry effects on shear aggregation of polymer colloids are very scarce in the open literature. Therefore, as a starting point, we decided to study the influence of only two surface attributes: the degree of ionization of surface groups and the area per charge groups. The first attribute was studied by carrying out aggregation experiments of surfactant-free carboxyl latex at various pH values in salt concentration well above the CCC; in a fixed flow field (same stirred tank at the same rpm) and ϕ . The second attribute was studied by repeating the experiments at various pH values for another surfactant-free carboxyl-modified latex with a smaller area per charge group albeit with smaller primary particle diameter. Sulphate latex with particle size similar to the carboxyl latex but with much larger area per charge group was also investigated. The bulk material for three latexes was polystyrene, the same as in the former two experimental studies. The experiments exhibited strong quantitative and qualitative dependency of the CMD on the two studied attributes. This suggests strong influence of structural forces and contact hysteresis, as detailed in chapter 5. In chapter 6 we shift the focus towards modeling flow-induced

aggregation. In this chapter we compare simulations using different aggregation efficiency models to aggregation kinetics obtained from two kinds of experiments; initial growth experiments and cluster regrowth experiments. The extensive set of experimental data allowed us to reach a conclusion as to which model is appropriate to model aggregation efficiency, hence to calculate rate of flow-induced aggregation. The thesis is terminated with conclusions and possible directions of future work.

1.3. Basics of modelling aggregation rate and aggregate structure

In a spatially uniform concentration and flow fields, the time evolution of the CMD of population of aggregates can be expressed through the following PBE

$$\frac{dN_i(t)}{dt} = \frac{1}{2} \sum_{k+j=i} K_{kj} N_j(t) N_k(t) - N_i \sum_{j=1}^{\infty} K_{ij} N_j(t) \quad (1.1)$$

where N_i is the number concentration of aggregates consisting of i primary particles, henceforth referred to as i -size aggregates, and K_{ij} is the aggregation rate function between i -size aggregates and j -size aggregates. As mentioned earlier, we focus on particles with net attractive interparticle potential, and negligible influence of gravity or inertia. For these conditions K_{ij} can be expressed as the sum of Brownian, K_{ij}^{Br} , and flow-induced, $\alpha_{ij} K_{ij}^{\text{sh}}$, aggregation rate functions⁵

$$K_{ij} = K_{ij}^{\text{Br}} + \alpha_{ij} K_{ij}^{\text{sh}} \quad (1.2)$$

The Brownian aggregation rate function K_{ij}^{Br} is given by

$$K_{ij}^{\text{Br}} = \frac{4\pi}{W_{ij}} (D_i + D_j) (R_{c,i} + R_{c,j}) \quad (1.3)$$

where W_{ij} is the stability ratio. In the current work $W_{ij} = 1$ since we focus on aggregation in the absence of an energy barrier^{2, 4}. $R_{c,i}$ is the collision radius of an i -size aggregate, and D_i is the diffusion coefficient, which can be calculated from Stokes-Einstein equation².

The rate function of flow-induced aggregation between i -size and j -size aggregates is represented as the product of the aggregation efficiency, α_{ij} , and the collision frequency function K_{ij}^{sh} . Usually the pioneering model of Smoluchowski^{2, 6} is assumed to represent K_{ij}^{sh} in laminar flow, while Saffman and Turner's model⁷ is used in turbulent flows. In both models, the collision frequency function takes the form:

$$K_{ij}^{sh} = k_o G (R_{c,i} + R_{c,j})^3 \quad (1.4)$$

where k_o is a numeric prefactor and G is the shear rate. The value of k_o and the equation to calculate G vary according to the macroscopic flow field around the aggregate. For simple shear flow $k_o = 4/3$ ^{2, 6}, where the velocity gradient represents the shear rate. For turbulent flow Saffman and Turner⁷ give $k_o = 1.294$, where G is related to the turbulent energy dissipation rate per unit mass, ε , and the kinematic viscosity ν according to

$$G = \left(\frac{\varepsilon}{\nu} \right)^{\frac{1}{2}} \quad (1.5)$$

Bäbler⁸, adopts a turbulent model where the flow on the length scale of the aggregate is assumed an axisymmetric extensional flow, which results in $k_o \approx 0.36$, and G is given by Eq. 1.5.

α_{ij} accounts for the distortion of the flow field by the aggregates, as well as the colloidal interactions between them. Models of α_{ij} are described in chapter 6.

Fractal scaling to describe aggregate structure

The fractal geometry of the aggregates² implies that the radius of gyration is related to the primary particle radius R_p via the scaling relation

$$R_{g,i} = k_g R_p i^{1/d_f} \quad (1.6)$$

where d_f is the fractal dimension and k_g is a prefactor with a value close to unity. For the sake of simplicity we can replace the hydrodynamic radius in Stokes-Einstein relation for D_i with $R_{g,i}$. $R_{c,i}$ can be assumed to be equal to $R_{g,i}$ ⁹ Such an approximation does not significantly change the Brownian aggregation rate for $d_f > 2$ ¹⁰. Additionally, once the aggregates exceed one micrometer, shear aggregation overshadows Brownian aggregation which diminishes the effects of any approximation in the Brownian aggregation term on the overall aggregation rate. Using the aforementioned scaling relation and Stokes-Einstein equation for D_i , and substituting $W_{ij} = 1$, results in the following expression for the Brownian aggregation rate function

$$K_{ij}^{Br} = \frac{2k_B T}{3\mu} (i^{1/d_f} + j^{1/d_f}) (i^{-1/d_f} + j^{-1/d_f}) \quad (1.7)$$

Where T is the temperature, k_B is Boltzmann constant and μ is the dynamic viscosity. Using the fractal scaling relation Eq. 1.6 in the collision frequency function results in

$$K_{i,j}^{sh} = k_o G R_p^3 (i^{1/df} + j^{1/df})^3 \quad (1.8)$$

Dimensionless number to characterize aggregation

Aggregation rate depends on the overall interaction potential between two aggregates¹¹. This potential is a complicated function of the surface chemistry, the liquid phase composition, and the bulk material⁴. In this thesis we focus on surfactant-free colloidal dispersions aggregating in aqueous electrolyte solution at concentrations well above the critical coagulant concentration (CCC). Under these circumstances one can assume that the only interparticle force of relevance to the aggregation process is the van der Waals force, which can be characterized by the Hamaker constant A_H . The effects of both the hydrodynamic forces and interparticle forces on flow-induced aggregation can be combined in one dimensionless group N_F ^{8, 12-14}.

$$N_F = \frac{A_H}{\mu R_p^3 G} \quad (1.9)$$

2. Experimental and measurement setup and methods

2.1. Equipment and materials

All experiments were carried out in the setup photographed in Fig. 2.1 and sketched in Fig. 2.2. At the heart of this setup is a 2.5 liter tank stirred with a six-blade radial flow Rushton impeller (the coagulator). Details of the tank are drawn in Fig. 2.3. The shaft of the impeller is fitted to a variable speed motor. The parameters of the motor speed controller are tuneable, thus the introduction of ramps in the rotation speed was possible, see chapter 4. Two valves are fitted to the bottom of this tank; one for filling the coagulator at the beginning of the experiment and draining it at the end, the other valve is used for coagulant injection and sample withdrawal for offline light scattering measurements and/or microscopy. A Lambda Vit-Fit programmable syringe pump was used for coagulant injection and sample withdrawal. Offline samples had a volume of 10 or 20 ml and were withdrawn, at speed slow enough to avoid breakage during sampling, into syringes previously filled with 50 or 40 ml of polyvinylalcohol (PVA) solution (100 mg L^{-1}) respectively. PVA works as a stabilizer to prevent further aggregation. Tests were carried out to confirm the absences of breakage during sampling and the stability of the samples. The larger sample size was used when the concentration inside the tank was very dilute.

Malvern Mastersizer 2000 instrument with 44 detectors was used for small angle static light scattering (SASLS) measurements. The location of the instrument relative to the tank is illustrated in Fig. 2.1. This instrument was used for off-line measurements of the samples as well as for on-line measurements. The on-line SASLS measurements were obtained by circulating a continuous stream from the tank through the measurement cell of the Mastersizer 2000. Flow in the circulation loop was driven by the membrane pump installed after the Mastersizer to minimize breakage of aggregates. The inconsequentiality of the circulation loop on aggregation in the tanks was tested by comparing off-line samples taken with and without the loop. Furthermore, pump speed was adjusted to ensure that the on-line SASLS measurements were a faithful representation of the CMD in the tank by comparing on-line and offline measurements. Details of the tests are given in section 2.4.

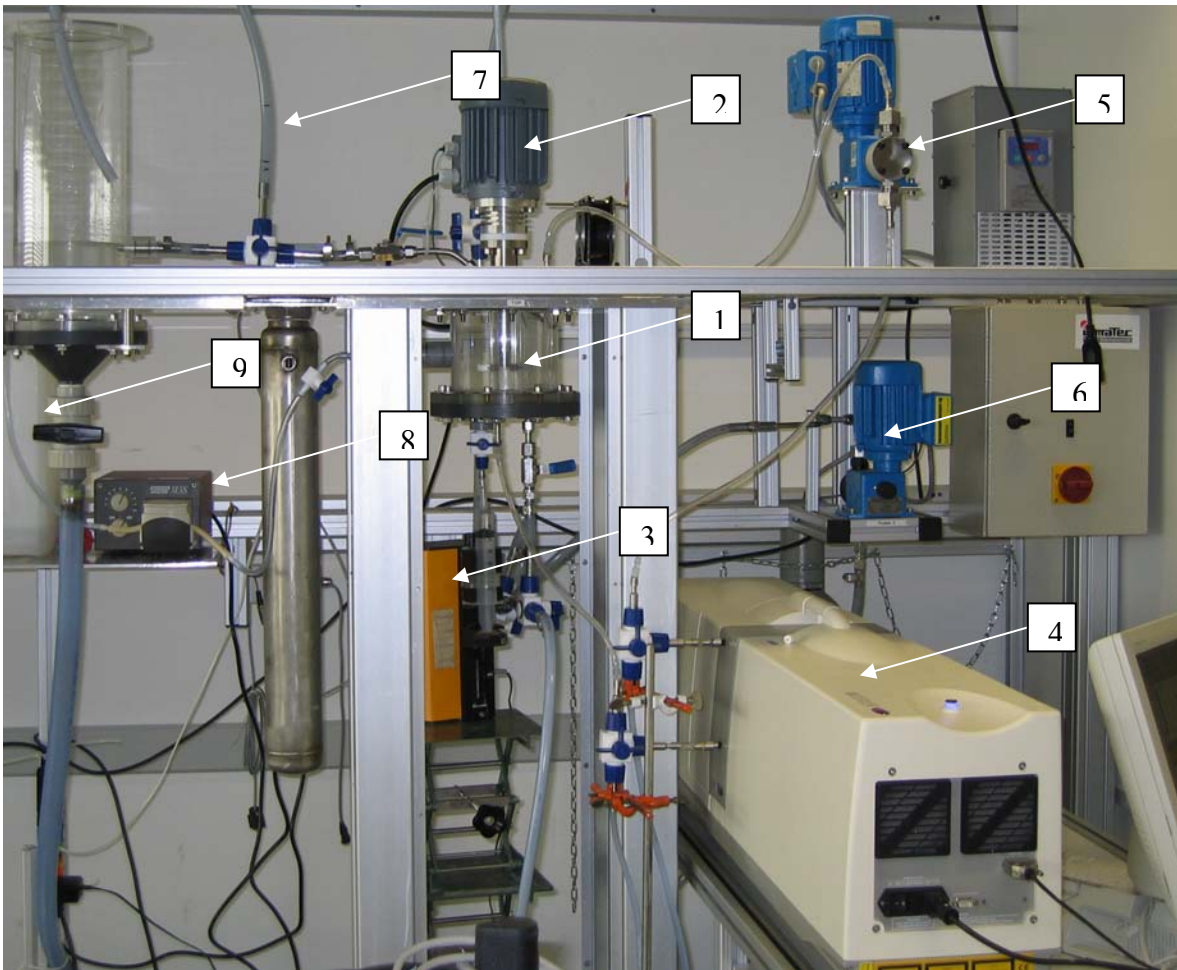


Figure 2.1: Photo of the experimental setup

- 1- Coagulator
- 2- Variable speed motor (speed controller not shown)
- 3- Syringe pump
- 4- Malvern Mastersizer 2000
- 5- Membrane pump for recirculation
- 6- Feed pump
- 7- Outlet tube that act as a reservoir
- 8- Peristaltic pump for dilution
- 9- Jerrican full of particle-free salt solution

An improvement was introduced to this configuration by changing the side feed port to the opposite side relative to the outlet tube. This means that the trajectory between the feed point and the outlet passes through the impeller region, which improves mixing during dilution.

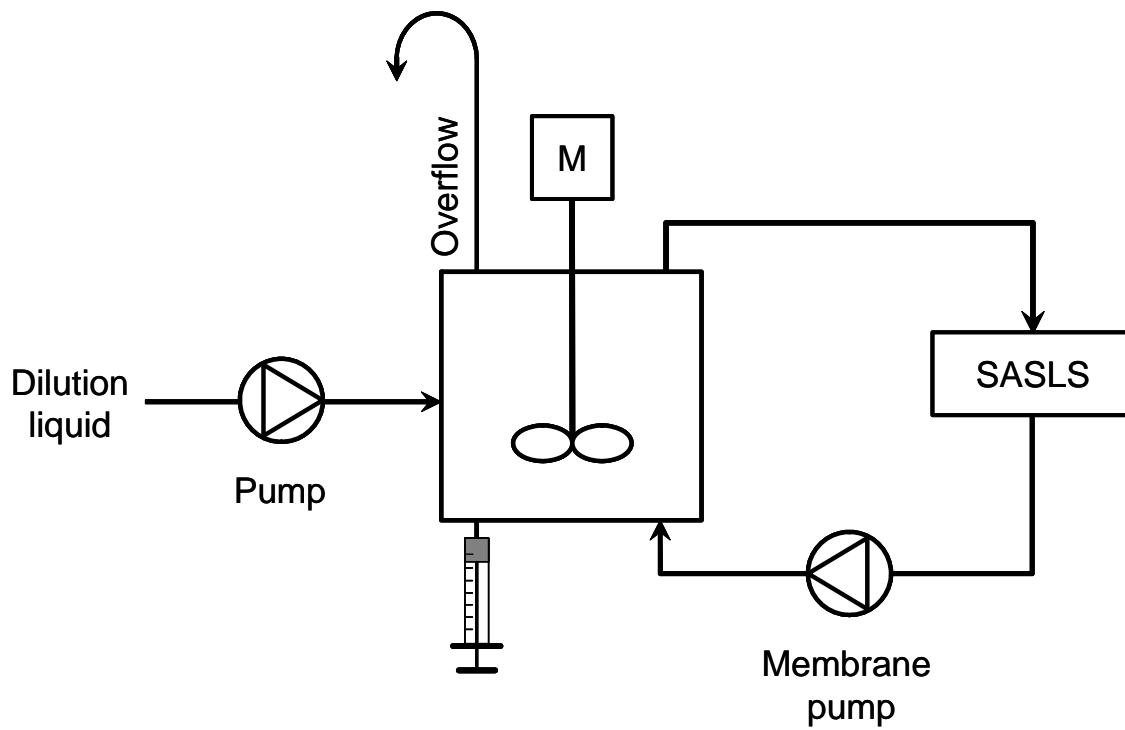


Figure 2.2: Sketch of the experimental setup

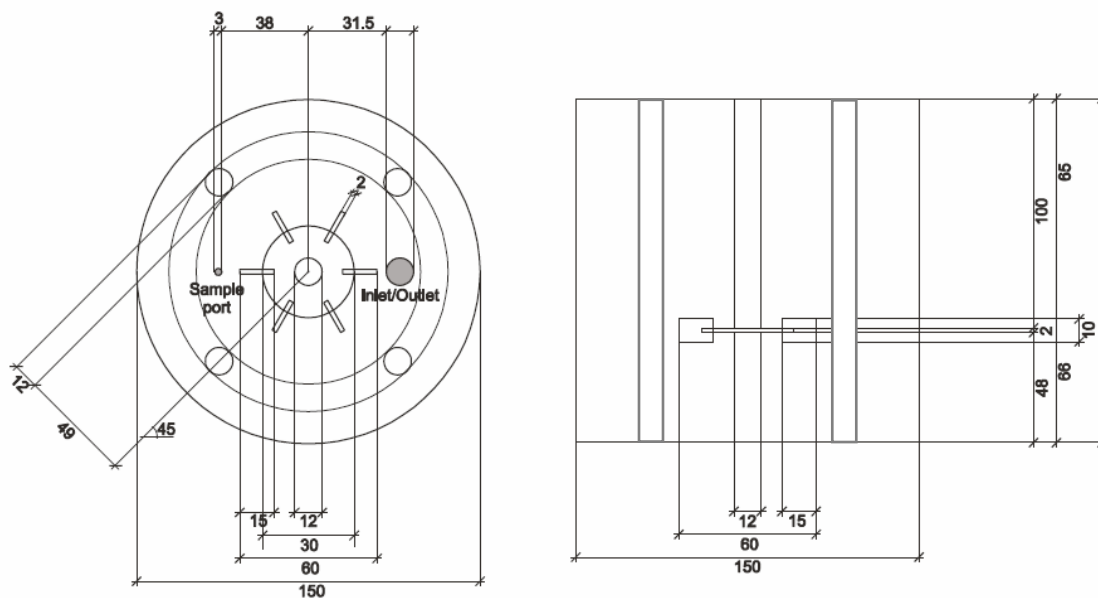


Figure 2.3: Bottom and side views of the coagulator, dimensions are in mm

The coagulator was also fitted with a side port to which a peristaltic pump was connected in the dilution experiments, see chapter 3. This side port was used to feed a stream of particle-free salt solution from the jerrican, placed on the left most side of Fig. 2.1. The flow rate of this side stream was controlled with this peristaltic pump. Finally, a 1 meter long tube was installed on the upper outlet of the coagulator to create a 100 ml reservoir that replenishes the coagulator after sample withdrawal and prevents air from entering the coagulator.

2.2. Experiment procedure

The initial suspensions with solid volume fractions in the range from 4×10^{-6} to 4×10^{-5} were obtained by diluting the original latex with appropriate amount of de-ionized water. The suspension was afterwards pumped from the storage tank into the coagulator using the feed pump, see Fig. 2.1. The coagulator was filled with care not to introduce air bubbles. After filling the coagulator, pumping continued with stirring to remove any air pockets and to fill the outlet tube that acts later as a reservoir. After filling the coagulator and removing the air, the initial suspension was stirred for approximately 15 minutes at 1000 rpm to ensure its stability and break any loose aggregates that might be present. Subsequently, the required stirring speed was set.

The aggregation process was started by introducing the required amount of a coagulant solution (30 mL of 20% w/w $\text{Al}(\text{NO}_3)_3$ in water or 60 mL of 35% w/w MgCl_2) to the coagulator using the syringe pump, see Fig. 2.1. The resulting salt concentration was well above the CCC for the given systems, i.e., the electrostatic repulsive forces between primary particles were fully screened and the particles were completely destabilized. Acids or bases were also added along with the salt solution in the experiments where we manipulated the pH, see chapter 5.

In order to achieve a good reproducibility of the initial aggregation kinetics, the syringe pump was always set to the same speed during salt injection. This speed was the maximum speed of the pump corresponding to N injection time of 15-30 seconds depending on the salt solution volume injected. A typical mixing time of the injected salt solution was about 5 seconds at 200 rpm (tested by dye measurements), which is an order of magnitude below the characteristic time of aggregation at all conditions considered in this work.

After salt injection the CMD starts to change until a steady state CMD is reached. Starting with this steady state CMD we carried out various types of stimulus response experiments. The first type of these experiments is the dilution experiments in which a particle-

free salt solution is fed to the coagulator via the side port using the peristaltic pump. Details of how the dilution rate is calculated are given in chapter 3. The second type of experiments is step response experiments in which the rotation speed was suddenly changed to a new value. The third and final type of experiments is the ramp experiments, in which the rotation speed was gradually and continuously changed at a rate slow enough to maintain equilibrium between aggregation and breakage. It was possible to induce sudden, step, or slow, ramp, changes in the rotation speed by tuning the parameters of the speed controller thus obtaining fast or slow response to manual change of the set point of the rpm.

2.3. Measurement and characterization techniques

2.3.1. Small angle static light scattering (SASLS)

The CMD in our experimental setup was characterized by SASLS, where the intensity of the scattered light, I , is measured at various scattering angles, θ . Each angle represents an inverse length scale, which is the amplitude of the scattering vector, q , to probe the scattering objects, see Fig. 2.4. Thus, the angular variation of the intensity, $I(q)$, provides information about the characteristic length scales of the scattering objects. $I(q)$ can be expressed as ¹⁵

$$I(q) = I(0)P(q)S(q) \quad (2.1)$$

where $I(0)$ is the zero angle intensity, $P(q)$ is the form factor (due to primary particles), $S(q)$ is the structure factor (due to the arrangement of primary particles within the aggregates), and q is defined as:

$$q = 4\pi \frac{n}{\lambda} \sin\left(\frac{\theta}{2}\right) \quad (2.2)$$

where n the refractive index of the dispersing fluid and λ the laser wavelength in vacuum.

Analysis of the measured scattered intensity, $I(q)$, in the Guinier region (for qR_g up to about unity) allows one to extract certain moments of the CMD, namely the root-mean-square radius of gyration, $\langle R_g \rangle$, and the zero angle intensity, $I(0)$, (corresponding to the mass weighted average mass ¹⁶).

In order to estimate the radius of gyration, the following approximation can be used in the Guinier region ¹⁵:

$$\frac{I(q)}{I(0)} \approx \exp(-q^2 \langle R_g^2 \rangle / 3) \quad (2.3)$$

However, the intensity of the scattered light depends on the detector location respective to the plane in which the incident light is polarized. Since it is not known to us whether in our instrument all the detectors are located in the same plane with respect to the polarization plane, we factor out this effect by measuring the form factor, $P(q)$, separately and then dividing the measured intensity, $I(q)$, to get the structure factor, $S(q)$. Thus, considering the Guinier approximation for the form factor, $P(q)$, of primary particles with radius of gyration, $R_{g,p}$:

$$P(q) \approx \exp(-q^2 \langle R_{g,p}^2 \rangle / 3) \quad (2.4)$$

we obtain for the structure factor, $S(q)$:

$$S(q) = \frac{I(q)}{I(0)P(q)} \approx \exp(-q^2 (\langle R_g^2 \rangle - \langle R_{g,p}^2 \rangle) / 3) \quad (2.5)$$

Taking the logarithm of both sides yields the following expression:

$$\ln \left(\frac{I(q)}{P(q)} \right) = \ln(I(0)) - \frac{q^2}{3} \langle R_g^2 \rangle_{S(q)} \quad (2.6)$$

where $\langle R_g^2 \rangle_{S(q)} = \langle R_g^2 \rangle - \langle R_{g,p}^2 \rangle$ and $I(0)$ can be determined from the slope and the intercept, respectively, of the linear relationship between $\ln(I(q)/P(q))$ and $q^2/3$. In order to obtain the average radius of gyration, $\langle R_g^2 \rangle$, we use the value of $\langle R_g^2 \rangle_{S(q)}$ determined from Eq. (2.6) and the radius of gyration of primary particles, $R_{g,p}$.

Moreover, if all aggregates exhibit a fractal scaling and they are in the limit of the Rayleigh-Debye-Gans (RDG) theory (rigorously valid within the following constraints $|m-1| \leq 1$ and $(4\pi R_p / \lambda) |m-1| \leq 1$, where m is the relative refractive index which for polystyrene equal to 1.195, and R_p is the radius of primary particle), where each primary particle in the aggregate scatters light independently from all the others, one can also estimate the fractal dimension of the aggregates, d_f , from the slope of the power law region of the log-log plot of $S(q)$ vs. q . However, as we will see later, some latex used in this thesis have primary particle size well outside the region of validity of the RDG theory. Therefore, we will denote the slope of the log-log plot $S(q)$

vs. q as the scaling exponent, SE , which is not necessarily equal to the fractal dimension, d_f , for the reasons mentioned above.

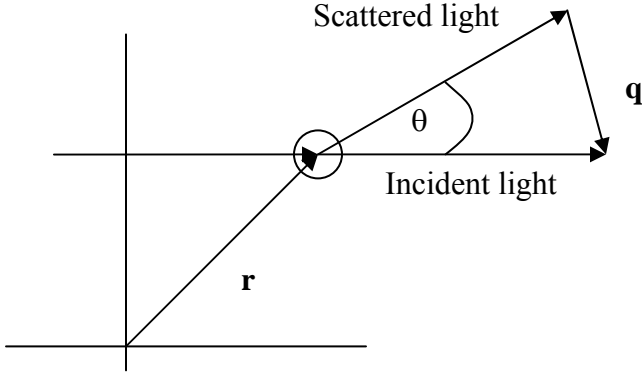


Figure 2.4, schematic illustration of scattering by an object at position \mathbf{r} to a detector at angle θ . \mathbf{q} is the scattering wave vector whose amplitude can be obtained from Eq. (2.2) for elastic scattering

2.3.2. Connection between SASLS and moments of the cluster mass distribution (CMD)

Soos et al⁹ propose a generalized expression to describe the scattering of the incident light by a population of aggregates:

$$I(q) \approx P(q) \sum_i N_i i^z S_i(q) \quad (2.7)$$

where $S_i(q)$ is the structure factor of aggregates consisting of i primary particles and z is the weighting exponent. The value of z depends on the primary particle size relative to the wave length of the incident light and on aggregate structure. In the limiting case where the RDG theory is valid for primary particles as well as for aggregates, $z = 2$, for other cases $z < 2$.

As mentioned earlier we can obtain two moments of the CMD from $I(q)$; these are the mean radius of gyration $\langle R_g \rangle$ and the zero angle scattered light intensity $I(0)$. These quantities are related to the CMD through

$$I(0) = C_{inst} \sum_i N_i i^z \quad (2.8)$$

$$\langle R_g \rangle = \left(\frac{\sum_i N_i i^z R_{g,i}^2}{\sum_i N_i i^z} \right)^{1/2} \quad (2.9)$$

During initial aggregation $z = 2$ is suitable to relate light scattering measurements and the CMD for the values of particle size used in this work. However, a smaller value has to be applied for the steady state CMD, where the population is mostly compact full-grown clusters. Ehrl et al¹⁷ give $z \approx 1.55$ for the clusters of the 810 nm primary particles, and $z \approx 1.78$ for clusters of the 120nm primary particle. These values were used in relating the experimental data of the regrowth experiments to the CMD in the simulation study presented in chapter 6.

To finalize this section we present an example of $I(q)$ and $S(q)$ obtained from experiments in Figs 2.5 and 2.6. Fig. 2.5 illustrates typical measurement during batch aggregation experiment. In this figure $I(q)$ at various time instances, during a typical experimental run at $\phi = 2 \times 10^{-5}$ and 200 rpm are shown. From these $I(q)$ spectra, as discussed above, the time evolution of the mean radius of gyration, the zero angle intensity and the scaling exponent are obtained. We can see in Fig 2.5, as the aggregation proceeds, the Guinier region, and the corresponding bend in $I(q)$ curve that occurs at $q \sim \langle R_g \rangle^{-1}$ (thus indicating the mean aggregate size), moves towards smaller values of q , which indicates larger mean sizes. On the other hand, the plateau value of the intensity $I(q)$ in the limit of $q = 0$, the intensity of scattered light at zero angle, increases. In Fig. 2.6 we illustrate a typical structure factor, $S(q)$ and indicate Guinier region for obtaining $\langle R_g \rangle$, the dotted line, and the power law region for obtaining SE , the solid line.

Furthermore, we have assessed the inaccuracy in the experimental data due to uncertainty in extracting $\langle R_g \rangle$ and $I(0)$ from the light scattering signal and found it to be in the range of $\pm 7\%$ in the values of $\langle R_g \rangle$ and $\pm 5\%$ in the values of $I(0)$. These values are within the experimental error, verified by several repetitions of each experiment.

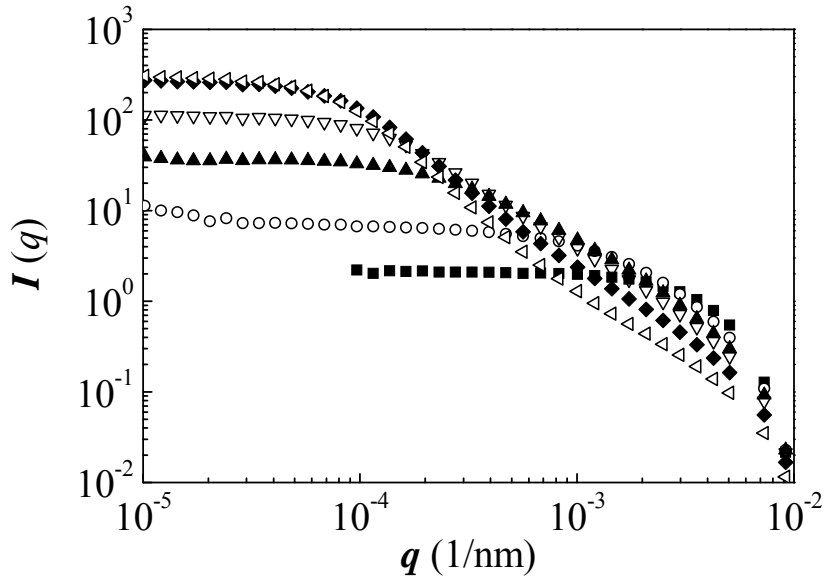


Figure 2.5: Time evolution of the intensity of scattered light $I(q)$ as a function of scattering wave vector q measured by SASLS instrument for the batch experiment with stirring speed 200 rpm and $\phi_0 = 2 \times 10^{-5}$. (solid square) $\tau = 0$, (open circle) $\tau = 1.3$, (solid up-triangle) $\tau = 2.6$, (open down-triangle) $\tau = 3.4$, (solid diamond) $\tau = 5.2$, (open left-triangle) $\tau = 10.4$. $\tau = Gt\phi$, where G is the volume averaged shear rate in sec^{-1} , t is time in sec, and ϕ the solid volume fraction.

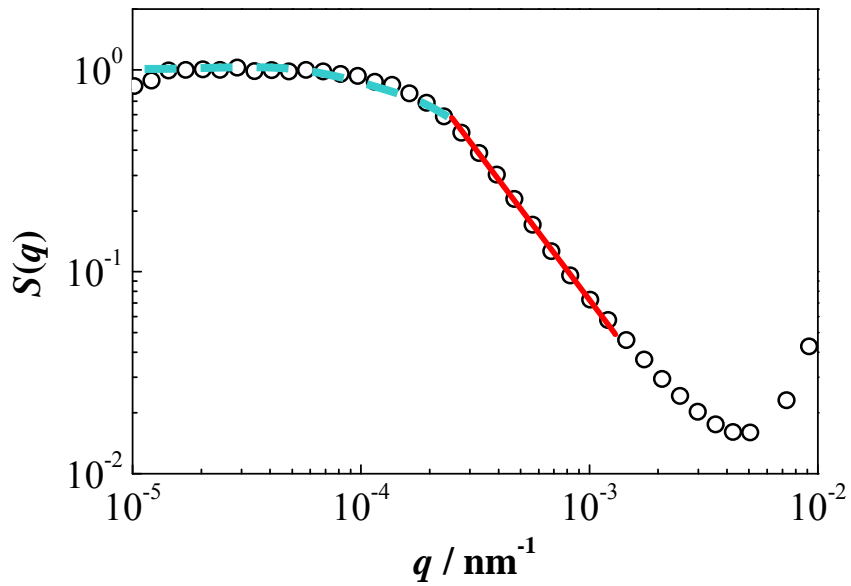


Figure 2.6: Illustration of the structure factor obtained from SASLS and the different region in it. The dotted line indicates Guinier region, from which we can obtain $\langle R_g \rangle$ and the solid line indicate the power law region used to get SE .

2.3.3. Confocal scanning laser microscopy and image analysis

Since the large size of the primary particles does not allow us to unequivocally determine the value of the fractal dimension from the light scattering measurement, d_f was independently obtained by image analysis of 2D CLSM pictures of aggregates, from samples withdrawn for off-line measurements at various operating conditions. The procedure to obtain these images was as follows. First, few drops of sample suspension were gently placed into a cut out of a 3 mm thick rubber band (used as a spacer), separating two cover slips. The rubber band prevents any damage of aggregates by capillary forces arising between cover slips without any spacing. Then, this sample holder was put on the stage of a confocal laser scanning microscope (Zeiss Axiovert 100) for capturing digital images of aggregates at various depths. Due to the low intensity of the reflected light from the surface of the particles the transmission mode was used to obtain 2D projections of the aggregates with the focal plane located approximately on the middle plane of the aggregates. Finally the zoom and contrast were adjusted to get reasonably clear-cut photos. From these images the structure of aggregates can be characterized by the perimeter fractal dimension, d_{pf} , obtained from the scaling of the projected surface area, A , vs. the perimeter, P , of the binary image of an aggregate,¹⁸⁻²¹

$$A \propto P^{2/d_{pf}} \quad (2.9)$$

Since d_{pf} depicts the surface morphology of the aggregate in two dimensional projection, its value varies between 1 (corresponding to a linear aggregate), and 2 (corresponding to a Euclidean aggregate). As was observed by several authors^{20, 22, 23}, typical values of d_{pf} at steady state for aggregates produced under turbulent conditions are in the range from 1.1 to 1.4. The d_f value can then be estimated using a correlation between perimeter fractal dimension and three dimensional fractal dimension developed by Lee and Kramer²⁴. Another piece of information extracted from the image analysis was the shape of the aggregates. We used the ratio between major and minor axis of the best fitted ellipse to describe the shape of the aggregate. All above mentioned quantities were obtained using the image analysis software ImageJ v1.34s (<http://rsb.info.nih.gov/ij/>). Raw images from the CSLM are shown besides the corresponding black and white images prepared for digitization and analysis using ImageJ are shown in Fig. 2.7. Table 2.1 is an excerpt of the spreadsheet used in processing the data.

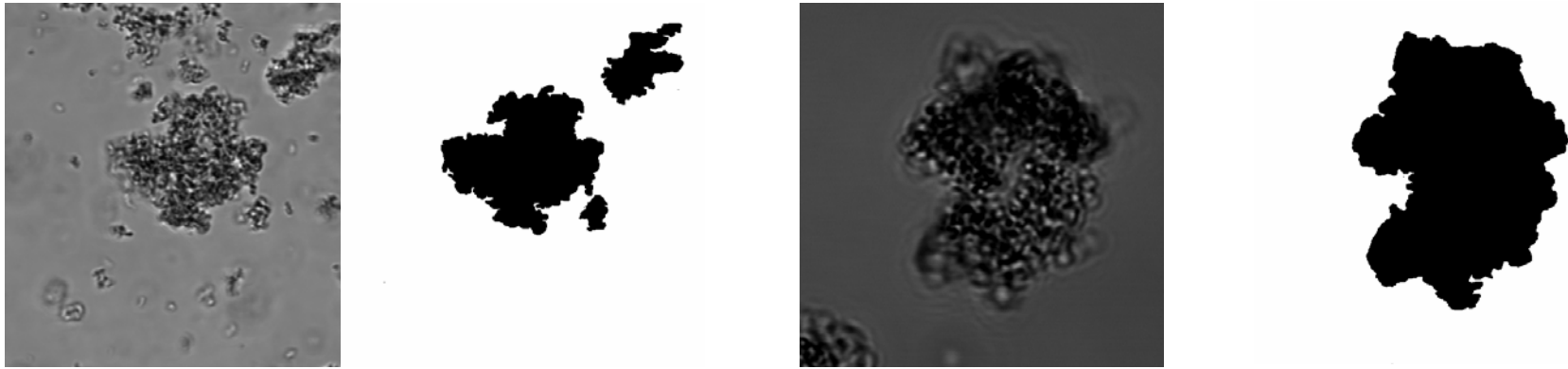


Figure 2.7: Examples of CSLM images and their black-white counterparts prepared for analysis using image J

Table 2.1: An excerpt of the spreadsheet used in processing data.

Nr.	Zoom Ratio	Area	Perimeter	L_max	L_min	Circularity	L_feret	L_Max-real (micron)	Aspect ratio

Zoom ratio – is the zoom ratio used in capturing the photo in CSLM, Area – is the area of selection (black region) in square pixels, Perimeter – is the length of the outside boundary of the selection, L_max, L_min, are the primary and secondary axis of the best fitting ellipse respectively. Circularity – is a measure of how smooth the perimeter is and is calculated as $4\pi \text{ (area/perimeter}^2\text{)}$. A value of 1.0 indicates a perfect circle. As the value approaches 0.0, it indicates an increasingly elongated polygon, and Feret's Diameter – is the longest distance between any two points along the selection boundary, also known as the caliper length. L_max-real is the maximum distance between two points on the perimeter according to the CSLM. The aspect ratio is the ratio between L_max, and L_min.

2.4. Tests and Validation

2.4.1. Effects of multiple light scattering

Multiple light scattering influences the measured moments of the CMD above a certain solid volume fraction. Therefore it is necessary to know the maximum solid concentration above which the used light scattering technique is influenced by multiple light scattering to ensure that our on-line measurements are meaningful. For this purpose we performed a series of light scattering measurements on suspensions of primary particles at various solid volume fractions of the latex having the larger primary particle size used in this thesis that is $D_p=810$ nm. In Fig. 2.8a,b we summarized the results in terms of the zero angle intensity $I(0)$ and the obscuration OB (i.e., the fraction of the incident light not transmitted to the detectors). In the absence of multiple scattering there should be a linear relationship between these measured quantities and the solid volume fraction (i.e., the concentration of primary particles). As we can see, the effect of multiple light scattering starts to be significant at the solid volume fraction $\phi = 3 \times 10^{-5}$ (when the obscuration exceeds 25%). There is about 10 % relative deviation from linearity for the zero angle intensity at the solid volume fraction $\phi = 4 \times 10^{-5}$. By comparing the results for $I(0)$ and OB in Fig. 2.8a,b one can see that the value of the zero angle intensity $I(0)$ is more sensitive to multiple light scattering than the obscuration OB , at least for the conditions investigated here. Since these measurements directly address only the effect of multiple light scattering for primary particles and not for larger aggregates, such as those observed at steady state, further tests were done to assess the effect of multiple scattering at steady state. This was done for all experimental conditions used in this work by measuring off-line samples withdrawn with a syringe, where the sample in the syringe was diluted 3-5 times compared to the original suspension in the tank. The scattered intensity of the on-line and off-line samples was always found to be proportional to the actual solid volume fraction in the measured sample for a given cluster distribution. Therefore we can safely neglect the effect of multiple scattering for on-line measurements in steady state conditions for solid volume fractions up to $\phi = 4 \times 10^{-5}$.

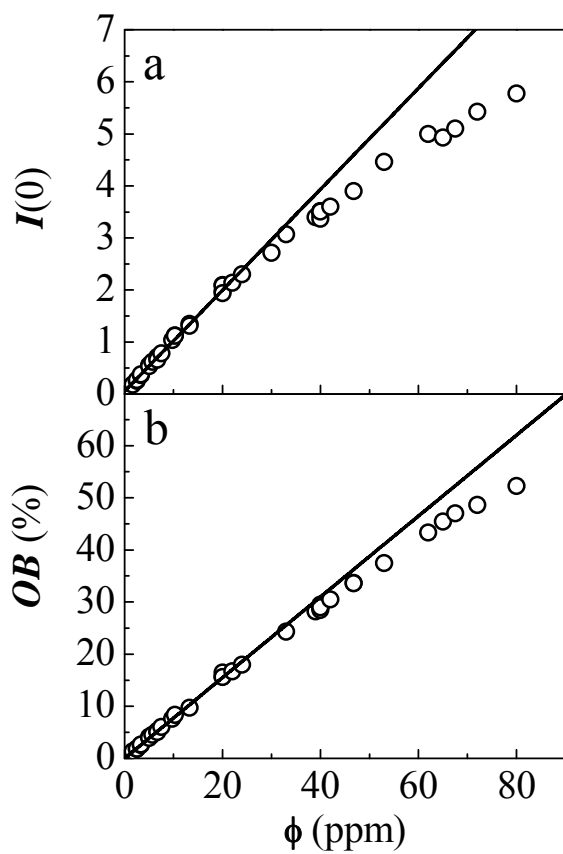


Figure 2.8: Deviation from the linear behavior as a function of the primary particle volume fraction for a) the zero angle intensity $I(0)$ and b) the obscuration OB

2.4.2. Validity of estimates of CMD moments based on the Guinier approximation

The value of the zero angle intensity $I(0)$ measured by light scattering is by definition independent of the scattering wave vector q and therefore it does not depend on the validity of the RDG approximation. On the other hand, the applicability of the fitting procedure using the Guinier approximation to determine the mean radius of gyration needs to be assessed for the large particles used in this thesis. Particles with a diameter of 810 nm were used in chapters 3 and 4. We used the Mie light scattering theory to calculate the dependency of the scattered intensity on the scattering wave vector amplitude q for spherical particles over a wide range of diameters, using the particle refractive index for polystyrene (1.59), the suspending medium refractive index for water (1.33) and the incident light wavelength $\lambda = 632.8$ nm, same as that of the laser in our instrument. Then we applied the fitting procedure as discussed above, section 2.3.1 to estimate the mean radius of gyration, using the linear regression (Eq. 2.6) in the interval $qR_g < 1.25$, which is the typical value used in the evaluation of $\langle R_g \rangle$ in our experiments. The data are shown in Fig. 2.9, where we compare the values of $\langle R_g \rangle$ estimated by fitting the $I(q)$ data, from Mie theory calculations, with the actual R_g of the sphere, indicate that the adopted procedure is valid even for large particles beyond the range of validity of the RDG theory.

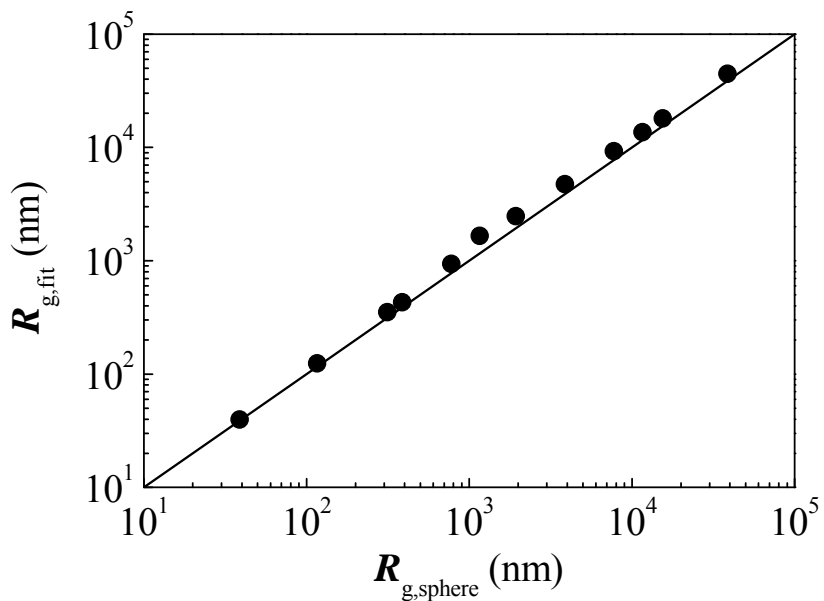


Figure 2.9: Radius of gyration estimated using the Guinier approximation Eq. (2.6) of the scattered intensity calculated from Mie theory for a sphere with a given (theoretical) radius of gyration; (solid circle) R_g estimated from the region $qR_g < 1.25$ which represents typical experimental condition

2.4.3. Validation of the on-line recirculation technique

The time evolution of the cluster distribution in the coagulator was monitored on-line using a recirculation loop through a light scattering instrument, as discussed earlier. Since aggregation and breakage processes studied here depend strongly on the shear rate, we need to assess the effect of the shear rate in the recirculation loop on the validity of the recirculation technique. In particular, we need to determine conditions under which: 1- the recirculation loop does not affect the CMD inside the coagulator, 2- the CMD does not change significantly before entering the measurement cell. The small volume of suspension in the recirculation loop compared to that in the coagulator ensures that any influence of the loop on the CMD in the coagulators is negligible. This was confirmed by comparing off-line samples taken from the coagulator at identical experimental conditions with and without the loop installed.

In principle, there are two possible ways how aggregates could be modified during their journey through the recirculation loop from the coagulator to the measuring cell of the light scattering instrument and back again to the coagulator. If the shear rate in the loop is larger than that in the tank aggregates could be broken into smaller fragments, which would lead to under prediction of the mean cluster size in the presence of the recirculation loop. On the other hand, if the shear rate in the loop is smaller than that in the tank and the residence time in the loop is long enough, then clusters can grow further by aggregation while in the recirculation loop, which would lead to over prediction of their mean size. This means that both the shear rate and the residence time in the loop need to be carefully chosen to prevent possible measurement artifacts.

The effects of shear rate $\langle G \rangle_{loop}$ and residence time in the recirculation loop on the measured quantities were evaluated through variation of the recirculation flow rate and tube diameter to cover a wide range of shear rates and residence times. The stirring speed was kept constant in order to always have the same cluster population in the tank. In Fig. 2.10a,b we show a comparison of the time evolution of two moments of the CMD, radius of gyration and the zero angle intensity, for various values of the shear rate in the loop, while the volume averaged shear rate in the tank was constant at $\langle G \rangle = 108 \text{ s}^{-1}$, corresponding to the stirring speed of 200 rpm. Since the flow in the loop was always laminar, the average value of the shear rate can be calculated as²⁵:

$$\langle G \rangle_{loop} = \sqrt{512} \frac{Q_{loop}}{\pi D_{tube}^3} \quad (2.10)$$

As can be seen in Fig. 2.10a,b the characteristic S-shape of the time evolution of both moments was observed for all tested conditions. At early times, when the cluster growth was controlled only by shear aggregation, as we will demonstrate later, the time evolution of both moments was the same for all tested conditions. This confirms that the residence time in the loop was short enough so that no significant additional aggregation occurs (dimensionless time in the loop was in the range of 0.035 – 0.15). At later stages, as time proceeds and aggregates grow further, the hydrodynamic forces acting on them increase and cause their breakup, which finally leads to a steady state. As can be seen in Fig 2.10a,b the measured steady state size strongly depends on the shear rate in the loop, even though the steady state size in the tank was always the same (this was verified with off-line measurements using a syringe). From this it is clear that if the shear rate in the loop is larger than the one in the tank, it can lead to significant underestimation of the cluster sizes. Obviously such artifacts must be eliminated from the measurement.

In order to validate the choice of flow parameters used in the recirculation loop for on-line measurements, we performed off-line measurements with a syringe for all our experiments. The average shear rate value in the sampling valve and in the syringe nozzle was always less or equal to 20 s^{-1} during sampling and the dimensionless time which each sample spent in the valve was very small. In order to prevent additional aggregation after sample withdrawal, the sample was simultaneously diluted and stabilized with PVA in the syringe²⁶ for subsequent measurement in the SASLS instrument. Example of the comparison between results obtained with on-line and off-line technique is shown in Fig. 2.11a,b for stirring speed 200 rpm and the solid volume fraction $\phi = 4 \times 10^{-5}$. In Fig. 2.11a,b we also summarized results of several repetitions of the same experiment in order to illustrate the reproducibility of the experiments. As one can see from Fig. 2.11a, the off-line measurements of normalized $\langle R_g \rangle$ agree well with the results obtained by the on-line technique. A small difference between the two techniques in terms of the normalized $I(0)$ in Fig. 2.11b at the steady state is caused by the fact that multiple light scattering slightly affects the measurement of the scattered light intensity for the primary particles used in this experiment (D_p 819nm) at $\phi = 4 \times 10^{-5}$ (see Fig. 2.8). This means that $I(0)$ at the steady state was normalized by the experimentally measured value of the $I(0)$ for primary particles, which is actually smaller by about 10% than the theoretical value for this solid volume fraction (see Fig. 2.8a). However, when we normalized the absolute value of $I(0)$ measured on-line at steady state by the theoretical

value of $I(0)_{t=0}$ from Fig. 2.8a, then the difference between the off-line (syringe) and on-line (loop) measurements vanishes.

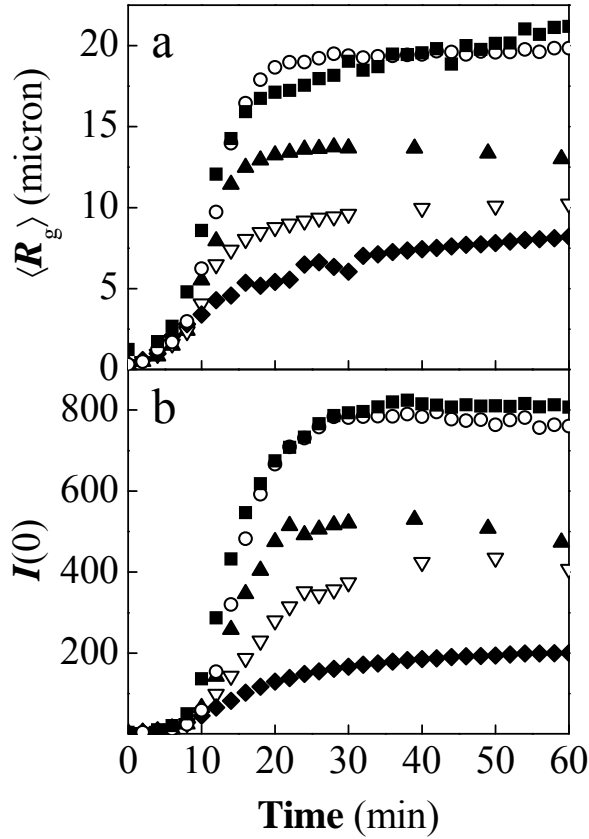


Figure 2.10: Effect of various values of the average shear rate inside the circulation loop on the time evolution of a) $\langle R_g \rangle$ and b) $I(0)$; (solid square) $\langle G \rangle_{loop} = 85 \text{ s}^{-1}$, (open circle) $\langle G \rangle_{loop} = 108 \text{ s}^{-1}$, (solid triangle) $\langle G \rangle_{loop} = 300 \text{ s}^{-1}$, (open down-triangle) $\langle G \rangle_{loop} = 600 \text{ s}^{-1}$, (solid diamond) $\langle G \rangle_{loop} = 900 \text{ s}^{-1}$; stirring speed 200 rpm ($\langle G \rangle_{loop} = 108 \text{ s}^{-1}$), $\phi_0 = 4 \times 10^{-5}$

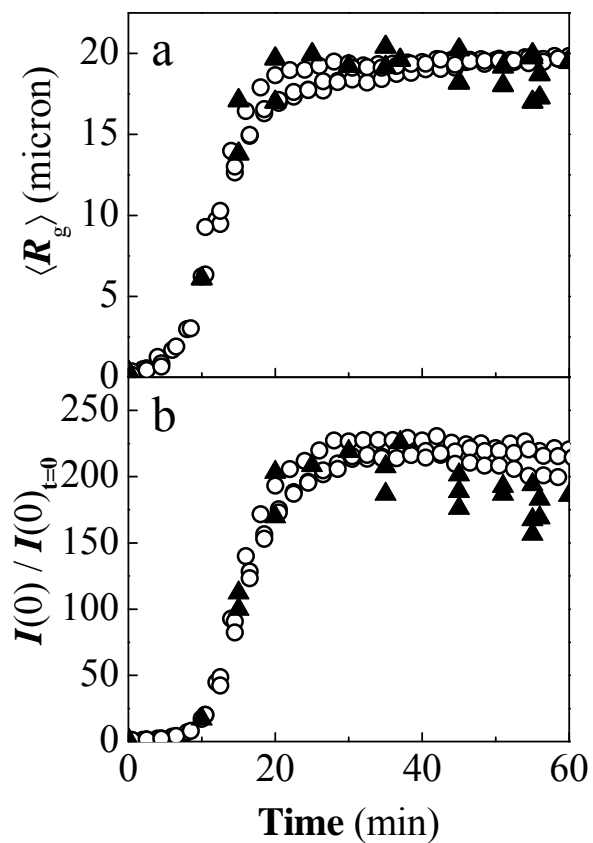


Figure 2.11: Comparison between on-line technique (open circles) and off-line (solid triangles) measurements of a) $\langle R_g \rangle$ and b) normalized $I(0)$. Batch experiment with stirring speed 200 rpm and $\phi = 4 \times 10^{-5}$

2.4.4. Effect of deposition

Another concern related to on-line measurement is the slow decay of the zero angle intensity at longer times. Since the zero angle intensity is directly proportional to the total mass of the system (at a given CMD), this decay of $I(0)$ at longer times (more than 40 - 50 min for the stirring speed 200 rpm) is most likely related to deposition of suspended polymer particles on the walls of the tank.

Moreover, deposition occurs also in the measuring cell of the SASLS instrument during long experiments. This effect was measured immediately after the dilution experiment by measuring the signal coming from deposits in the measuring cell. Comparison of the $I(q)$ obtained for steady state of the batch experiment (solid squares) together with $I(q)$ for steady state after the dilution (solid circles) and $I(q)$ corresponding to the deposits measured after the dilution when having pure water in the cell (solid triangles) is shown in Fig. 2.12 for the experiment done at stirring speed 635 rpm and solid volume fraction starting from 4×10^{-5} and then decreasing to 2×10^{-6} with continuous dilution. In the same graph we also show the net $I(q)$ for the steady state after dilution (open diamonds) calculated from the original $I(q)$ curve (solid circles) by subtracting the contribution of the deposits (solid triangles). As one can see the difference is small compared to the originally measured $I(q)$ (open diamonds vs. solid circles) and it only appears to be significant in the region of large values of q corresponding to the length scale of primary particles. Since the values of $I(0)$ and $\langle R_g \rangle$ are extracted from the region of $I(q)$ at small q values, which is not affected by the deposition, these are reliable results. A small increase (around 8 % for this particular case) was present in the slope of the power law region (SE), but we note that such variation is comparable to a typical spread between repetitions of the same experiment at identical conditions. Therefore we can conclude that the effect of deposition on the results obtained from the on-line measurement including dilution is not significant as long as the total duration of the measurement does not exceed 90-120 minutes, for the latex and light scattering cell used in this work. For longer experiments effects of deposition on the value of $I(0)$ measured on-line may be significant.

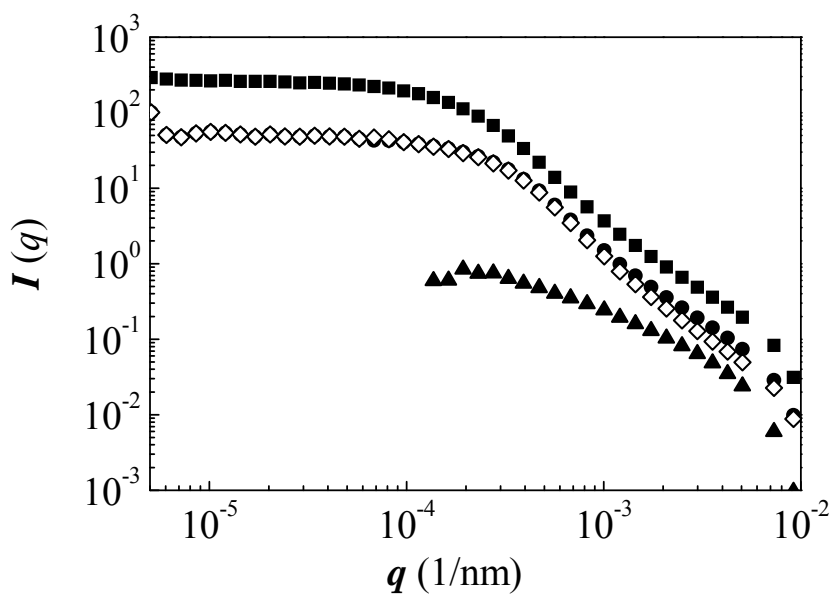


Figure 2.12: Scattered intensity $I(q)$ as a function of the scattered angle q , (solid square) steady state of the batch experiment at $\phi_0 = 4 \times 10^{-5}$, (solid circles) steady state after dilution $\phi_{\text{END}} = 2 \times 10^{-6}$, (solid triangle) deposits measured after the dilution experiment, (open diamond) intensity curve obtained by subtracting the scattering due to deposits from the scattering observed at the end of the dilution experiment. Stirring speed 635 rpm.

2.5. Summary of CFD description of the stirred tank coagulator

The fluid flow in the coagulator was characterized by computational fluid dynamic (CFD) simulations using a commercial software, Fluent v6.1, applying a standard $k-\varepsilon$ model²⁷⁻²⁹. The obtained values of the volume average turbulent energy dissipation rate $\langle \varepsilon \rangle$, turbulent kinetic energy $\langle k \rangle$, shear rate $\langle G \rangle$, and Kolmogorov micro-scale $\langle \eta \rangle$ are summarized in Table 2.2, covering the entire range of stirring speed investigated in this work. In Fig. 2.13 the shear rate distribution normalized by its volume average value, calculated for a stirring speed equal to 200 rpm, is shown. Since all experiments presented in this work were done under turbulent conditions, it was found that for the defined geometry the shape of the shear rate distribution is self-preserving, which is in agreement with Alexopoulos et al.³⁰ For the current geometry, where a Rushton type impeller is used, it is seen that the shear rate distribution is rather broad, covering approximately three orders of magnitude. In agreement with Derksen et al.³¹, who used a Large Eddy Simulation technique, the largest values of the shear rate (exceeding ten times the volume averaged values) are located at the tips of the impeller blades.

Table 2.2: Volume average values of the energy dissipation rate $\langle \varepsilon \rangle$, turbulent kinetic energy $\langle k \rangle$, shear rate $\langle G \rangle$, and size of the Kolmogorov eddies $\langle \eta \rangle$ (evaluated using the volume average energy dissipation rate) for the various stirring speed values used in the experiments

Stirring speed (rpm)	$\langle \varepsilon \rangle$ (m^2s^{-3})	$\langle k \rangle$ (m^2s^{-2})	$\langle G \rangle$ (s^{-1})	$\langle \eta \rangle$ (μm)*
200	3.04×10^{-2}	2.693×10^{-3}	108	120.6
417	0.268	1.231×10^{-2}	325	69.3
635	0.9319	2.938×10^{-2}	613	50.4
854	2.239	5.423×10^{-2}	958	40.3
1073	4.403	8.695×10^{-2}	1353	34.0

- minimum Kolmogorov micro-scale evaluated with CFD is approximately equal to $\langle \eta \rangle / 10$ for all stirring speeds

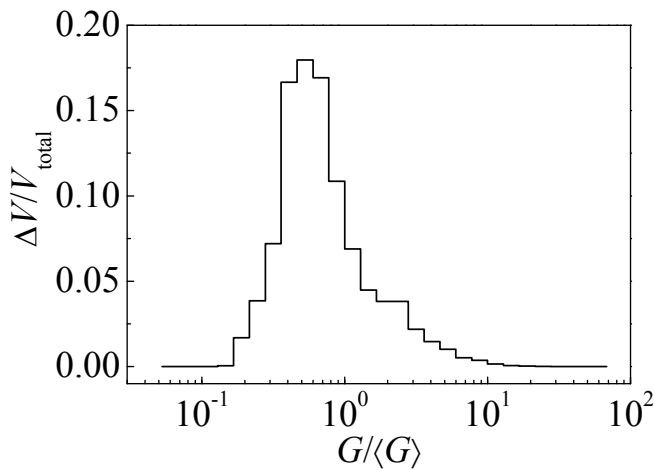


Figure 2.13: Histogram of the normalized shear rate distribution in the stirred tank calculated for a stirring speed equal to 200 rpm. G here refers to the local value of the shear rate in a volume segment ΔV

3. Effect of solid volume fraction

3.1. Introduction and literature review

Shear driven aggregation typically results in a self-accelerated growth up to a certain size, after which further growth gradually slows down and eventually a steady state cluster mass distribution (CMD) is established, see Figs. 2.10 and 2.11. Three hypotheses can be postulated to explain the attainment of a steady state CMD: vanishing aggregation efficiency with increase in aggregate size, destructive collision between aggregates, and breakage of aggregates due to hydrodynamic stresses. The first objective of the work presented in this chapter is to reveal which of these hypotheses is plausible.

The first hypothesis surmises that as hydrodynamic resistance to inter-aggregate flow increases with increase in aggregates size and/or fractal dimension, a time is reached when further aggregation is stopped and the CMD converge to a steady distribution. In other words a maximum aggregate size exists beyond which aggregates can not collide and form bigger aggregates due to fluid hindrance i.e. collision efficiency become zero. This view point is adopted in the simulations done by Brakalov³², and Han and Lawler¹³ assuming impermeable particles. Furthermore, some models assuming uniform porosity and relating permeability to the fractal dimension predict behavior close to that of an impermeable spheres when the fractal dimension grows beyond 2.3³³, a value that many suspensions aggregating under shear in natural and man-made systems exceed see next chapter and Wiesner³⁴. This hypothesis predicts that steady state CMD should be independent of solid volume fraction³².

The second hypothesis proposes that the increase in cluster mass during the course of aggregation leads to occurrence of destructive collisions between aggregates leading to their break-up. Stratford³⁵ and Iick and coworkers^{36,37} used this hypothesis to interpret the observation of steady state size distribution in their experiments. Serra and Casamitjana³⁸ used this hypothesis to interpret the independence of the steady state aggregate size of solid volume fraction when the shear rate was above a certain value and incorporated this mechanism in their model by using effective collision efficiency as a fitting parameter instead of calculating the collision efficiency independently.

The third hypothesis states that hydrodynamic stresses due to velocity gradients on the aggregate length scales can cause aggregate fragmentation and/or erosion^{39, 40}, thus limit the size by counteracting aggregation.

Each of these three hypotheses suggests a different approach to model an aggregating suspension. The first of them implies that some sort of maximum size criterion should be derived and incorporated in the model to make aggregation terms vanish for clusters of large sizes^{32, 41, 42}. The second hypothesis implies that breakage should be modeled as a second order process, because it requires the encounter of two entities³⁸. The third hypothesis entails that breakage is first order in aggregate concentration and that the steady state CMD is a dynamic equilibrium between a second order forward process (aggregation) and a first order backward process (breakage), thus the average sizes of aggregates should increase with increase in solid volume fraction. This hypothesis is adopted in many modeling and simulation studies⁴³⁻⁴⁶. These considerations clearly indicate the relevance of aggregation experiments with varying solid volume fraction in testing the aforementioned hypotheses.

However, the experimental evidences reported in the literature regarding the effect of solid volume fraction on flow-induced aggregation, although relatively scarce, do not lead to an unequivocal conclusion about which mechanism leads to the steady state CMD. Oles⁴⁷ and Wang et al.²³ investigated dilute suspensions of polystyrene latex (PSL) particles in Couette type flows, where the first one covered flow conditions crossing from laminar to turbulent using particles of 2.17 micron in diameter and the second one investigated laminar conditions using PSL particles of 9.6 micron in diameter. Another set of data published by Kusters et al.²⁶ described the behavior of the system using PSL particles with diameter of 0.8 micron coagulated under turbulent conditions in a stirred vessel. All of the above studies investigated systems at just two solid volume fractions and observed that the steady state cluster size either increased^{26, 47} or remained the same²³ when increasing the solid volume fraction was increased. Similarly, Kobayashi et al.⁴⁰, using PSL particles with diameter of 1.356 micron, observed that the characteristic size at steady state in breakage experiments performed under turbulent conditions in stirred vessel was monotonically increasing with solid loading over a wide range of solid volume fractions. On the other hand, Serra et al.⁴⁸, using a Taylor-Couette apparatus in both laminar and turbulent conditions with PSL particles with diameter of 2 and 5 micron, observed

that the steady state size either did not change or decreased when the solid volume fraction was increased.

The goal of the work presented in this chapter is to investigate the effect of solid volume fraction on the time evolution of the CMD under turbulent conditions in a stirred tank coagulator. In order to investigate the effect of the solid volume fraction on the steady state CMD over a wider range of values, we designed a novel experiment based on the perturbation of the steady state attained in a batch operated coagulator by decreasing the solid volume fraction using continuous dilution. The dilution experiment allows us to obtain more detailed information about the balance between aggregation and breakage at steady state, and its dependence on the solid volume fraction.

3.2. Batch experiments

Let us first consider the aggregation experiments operated in the batch mode (i.e. the dilution pump in Fig. 2.2 is switched off). In these experiments the aggregation starts from a well-stirred stable suspension of primary particles at the desired solid volume fraction and rotation speed, which is then fully destabilized by injecting the required amount of coagulant into the coagulator. The cluster growth process was monitored on-line by the SASLS instrument using the recirculation technique discussed in the previous chapter.

The effect of solid volume fraction on aggregation dynamics was investigated for values of ϕ in the range from 4.5×10^{-6} to 4×10^{-5} , for the same stirring speed of 635 rpm. The obtained results for both moments of the CMD are shown in Fig 3.1 as a function of the dimensionless time for shear aggregation $\tau = t \langle G \rangle \phi$. As one can see at the beginning of the process (dimensionless time smaller than two), the time evolution of both moments for all values of solid volume fraction plotted in dimensionless time τ reduces to a single curve, which indicates that the growth of aggregates in these systems is solely controlled by shear aggregation. As the aggregates grow further and their distribution approaches a steady state, the different experimental curves deviate from each other, thus indicating that the evolution of the measured moments of the CMD depends on the solid volume fraction. In the same figure we can see that steady state values of both moments increase with the solid volume fraction. The same trend, in terms of one single moment of the distribution, has been reported by Oles⁴⁷, Kusters et al.²⁶ and Kobayashi et al.⁴⁰ for primary particles with diameters of 2.17, 0.8 and 1.36 μm , respectively,

and for values of ϕ close to those considered in this work. It is worth mentioning that, at least in qualitative terms, these findings are consistent with the different dependency of aggregation and breakage kinetics on cluster concentration: second order for aggregation and first order for breakage, which balance each other at steady state.

In Fig. 3.2 we show the time evolution of the scaling exponent for the same experiments considered in Fig. 3.1a, b. It can be seen that changes in the solid volume fraction do not significantly affect time evolution of the SE . The low values of scaling exponent at the beginning of the process is caused by the presence of a significant fraction of the smaller aggregates, which scatter light differently compared to large clusters with fully developed fractal scattering behavior^{27, 49}. As the aggregates grow, the effect of these small non-fractal aggregates becomes less important and the value of SE increases. When both moments of CMD, $\langle R_g \rangle$ and $I(0)$, reach steady state then also SE approaches its steady state value, which is in this particular case around 2.2 for all the investigated solid volume fractions. A similar trend in SE was observed by Selomulya et al.^{50, 51} and Waldner et al.²⁷ for two different vessel geometries (Taylor-Couette device and stirred tank respectively), where larger values of SE were found in the case of Taylor-Couette compared to the stirred tank. It is worth emphasizing that the value of SE can not be assumed to be equal to the fractal dimension of the aggregates, since for this large size of primary particles light scattering is outside the range of validity of the RDG theory. However, the value of SE provides an indication of the structure of the population of aggregates once these are sufficiently large. Since its value for all investigated solid volume fractions is nearly the same, we conclude that the structure of aggregates, at least at steady state, is rather similar for all solid volume fractions considered at a given stirring speed.

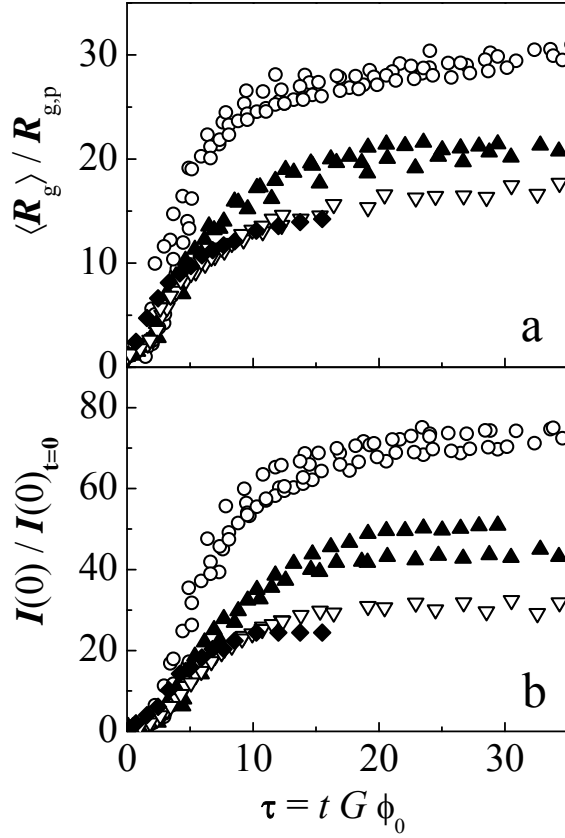


Figure 3.1: Time evolution of a) normalized $\langle R_g \rangle$ and b) normalized $I(0)$ for various values of the solid volume fraction and stirring speed of 635 rpm; (O) $\phi = 4 \times 10^{-5}$, (\blacktriangle) $\phi = 2 \times 10^{-5}$, (∇) $\phi = 1 \times 10^{-5}$, (\blacklozenge) $\phi = 4.5 \times 10^{-6}$.

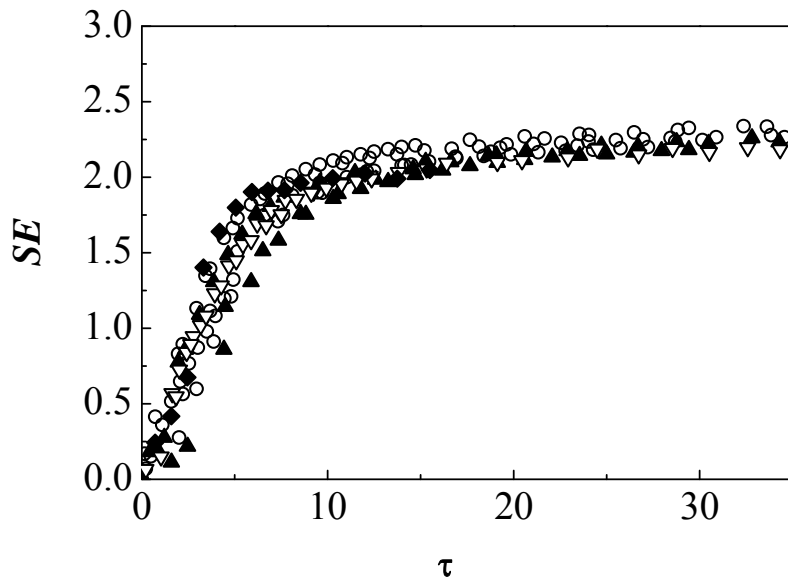


Figure 3.2: Time evolution of the scaling exponent SE for various values of the solid volume fraction and stirring speed 635 rpm; (\circ) $\phi = 4 \times 10^{-5}$, (\blacktriangle) $\phi = 2 \times 10^{-5}$, (∇) $\phi = 1 \times 10^{-5}$, (\blacklozenge) $\phi = 4.5 \times 10^{-6}$.

3.3. Development and validation of the dilution experiment

The objective of the dilution experiments is to collect in a simple and fast way many steady state CMDs as function of solid volume fraction. For this purpose the suspension in the coagulator is diluted after the attainment of the steady state CMD with a rate of dilution small enough to preserve perfect mixing in the tank *and* equilibrium between aggregation and breakage. This means that the dilution rate has to be selected in a way that macromixing timescale is smaller than those of both aggregation and dilution whereas the aggregation timescale has to be smaller than that of dilution. The first one of these two timescale criteria ensures that the flow pattern and concentration profile in the tank are close to those in an ideal CSTR⁵², so that the solid volume fraction is uniform in the tank and can be calculated easily and accurately. The second criterion ensures that dynamic equilibrium condition between aggregation and breakage is achieved at every single instant of time during the dilution experiment. In other words, the dilution rate is slow enough that aggregation and breakage processes can readjust the CMD almost instantaneously with respect to the gradually changing solid volume fraction. This provides directly the steady state CMD as a function of the solid volume fraction. In the next section we discuss the evaluation of the relevant timescales.

3.3.1. Time scale analysis

To ensure that the cluster mass distribution is homogeneously distributed within the tank, the characteristic time of mixing τ_B needs to be smaller than the characteristic time of aggregation τ_A . Macromixing time for a stirred tank can be calculated as⁵³:

$$\tau_B = 5.9 D_t (\langle \varepsilon \rangle D_i)^{-1/3} \quad (3.1)$$

where D_t is the tank diameter, D_i is the impeller diameter and $\langle \varepsilon \rangle$ is the volume averaged turbulent energy dissipation rate. Using tank diameter $D_t = 150$ mm, impeller diameter $D_i = 60$ mm and volume averaged turbulent energy dissipation rate (at rotation speed 635 rpm) $\langle \varepsilon \rangle = 0.9309 \text{ m}^2/\text{s}^3$, we obtain the value of τ_B equal to 2.5 s. We note that the corresponding turbulence timescales⁵⁴, such as the integral scale of turbulence k/ε and the Kolmogorov timescale $(\nu/\varepsilon)^{1/2}$, are on the order of microseconds. As we will see shortly, the aggregation timescale is much longer than the characteristic timescale of turbulence, so that in our conditions we are far from the micromixing limit.

When the characteristic timescale of macromixing, defined in Eq. 3.1, is much shorter than the aggregation timescale defined as⁵⁴:

$$\tau_A = \frac{1}{\alpha_A G (R_{c,i} + R_{c,j})^3 N} \quad (3.2)$$

where α_A is the aggregation rate prefactor, G is the shear rate, $R_{c,i}$ and $R_{c,j}$ are the radii of colliding aggregates and N is the number concentration of aggregates ($\phi / V_p i$), then we can assume homogeneous conditions in the tank with respect to the particles or distribution of clusters.

In order to estimate the aggregation timescale we need to determine the quantities appearing in Eq. 3.2. The value of the aggregation rate prefactor α_A was estimated from the initial kinetics of the process and it was previously found to be around 0.2 for the system investigated here²⁷. The volume averaged shear rate was calculated using the CFD software FLUENT and for the stirring speed 635 rpm it is equal to 613 s^{-1} , see Table 2.2. Since we do not have complete information about the CMD at steady state, in order to evaluate τ_A we used the value of $\langle R_g \rangle$ measured experimentally as collision radii $R_{c,i}$ and $R_{c,j}$. Finally, assuming the fractal dimension of aggregates at the steady state to be equal to the scaling exponent measured experimentally, which in this particular case is equal to 2.2, we can calculate the number concentration of aggregates N at steady state. The corresponding timescale of aggregation, τ_A from Eq. 3.2, is then equal to 10 s at the beginning of the dilution process at the solid volume fraction ϕ equal to 4×10^{-5} , increases to about 120 s for ϕ equal to 5×10^{-6} and is equal to about 300 s at the end of the dilution experiments when ϕ is equal to 2×10^{-6} . We note that since for the purpose of the evaluation of the timescale of aggregation the CMD at steady state was approximated as monodisperse the obtained values should be treated as upper bound of the real values.

In order to ensure that the tank is ideally macromixed during the dilution process, without dead zones or bypasses, we performed a residence time distribution experiment, where the tracer concentration in the tank was measured as a function of time for various dilution rates. Based on the time scale analysis and the residence time distribution experiment, it was found that the tank behaved like an ideal CSTR⁵² up to a dilution rate of 0.38 L/min for 635 rpm, which leads to a value of residence time τ_R defined as:

$$\tau_R = \frac{V_c}{\dot{Q}_d}. \quad (3.3)$$

equal to 400 s.

3.3.2. Experimental validation of the dilution experiment

Let us examine the dilution experiment shown in Fig 3.3., which starts from the steady state conditions corresponding to the solid volume fraction $\phi = 4 \times 10^{-5}$ and constant stirring speed of 635 rpm obtained in batch operation mode. The dilution rate was 0.3 l/min. It is seen that the values of both moments decrease steadily during dilution, but as soon as the dilution is interrupted both moments stop decreasing and remain constant almost immediately. The absence of time lag suggests that the dilution rate is sufficiently slow compared to the rates of aggregation and breakage that dynamic equilibrium is achieved instantaneously with respect to the dilution characteristic time.

In Fig. 3.4 we show the corresponding time evolution of the SE , where we can see that during dilution the value of SE does not change, which is consistent with the independence of SE from ϕ observed for batch experiments in Fig. 3.2. This indicates that the structure of the aggregates remains unchanged during dilution.

Another aspect that can be best investigated with this experimental setup is the reversibility of the equilibrium between the aggregation and breakage processes. If such equilibrium is reversible then the values of both moments of the CMD at steady state for a given solid volume fraction should be independent on the path through which this steady state was reached (at given stirring speed). This means that the same steady state CMDs should be obtained from either a batch experiment at the given solid volume fraction or from a dilution experiment starting from a higher initial solid volume fraction and then diluting the dispersion to the desired solid volume fraction.

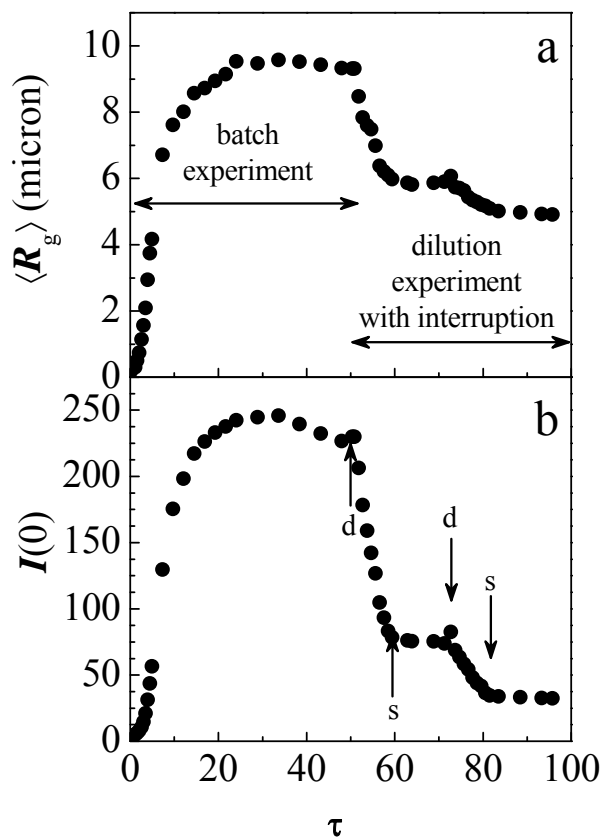


Figure 3.3: Time evolution of a) $\langle R_g \rangle$ and b) $I(0)$ for typical batch and dilution experiment for stirring speed 635 rpm and solid volume fraction $\phi = 4 \times 10^{-5}$; (d) and (s) indicates start and stop of dilution, respectively.

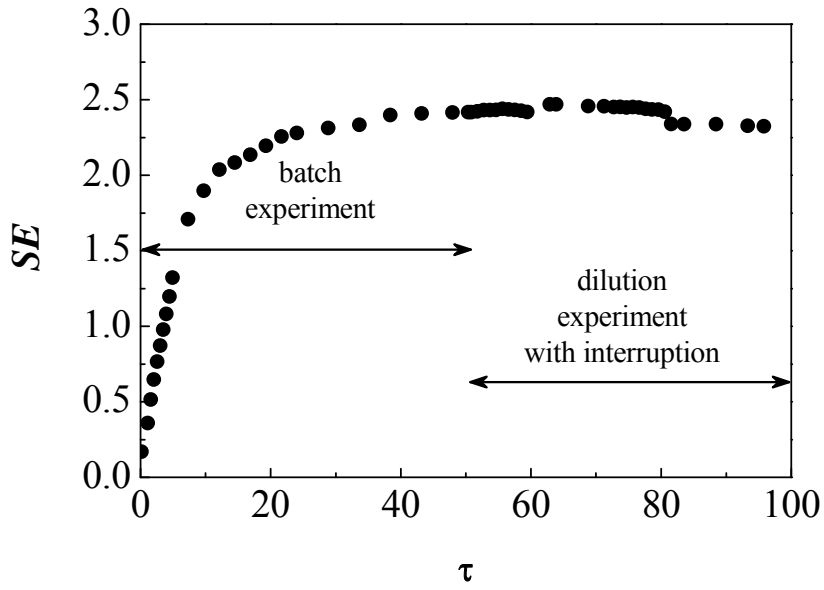


Figure 3.4: Time evolution of the SE during a batch experiment and the subsequent dilution experiment as described in Fig. 3.3, stirring speed 635 rpm and solid volume fraction $\phi = 4 \times 10^{-5}$.

The reversibility of the equilibrium between the aggregation and breakage processes is demonstrated by the experiments considered in Fig. 3.5, which shows the $I(0)$ values as a function of time for both experimental modes: batch and dilution. The dilution experiments were stopped at suitable times so that three plateaus can be seen corresponding to three pairs of solid volume fraction values which are identical but achieved through different paths. Nevertheless, it is clear that the $I(0)$ values, and therefore the corresponding CMDs, are identical, which indicates that the process is fully reversible. A similar observation was made by Kusters²⁶ in suspensions of colloidal polymer particles destabilized by strong electrolytes. On the other hand, for example when the coagulant is a precipitating solid (i.e., $\text{Al}(\text{OH})_3$) or a polymer, the suspension may exhibit irreversible aggregation dynamics⁵⁵⁻⁵⁷, where the coagulant affects the internal structure of the aggregates and changes their strength over time. The path independence supports also the soundness of the dilution concepts to collect steady state CMD as a function of ϕ .

Since we have demonstrated that in the dilution experiments the system is at each time at steady state, in the sense that aggregation and breakage equilibrate each other, we can plot the CMD characteristics as a function of the actual solid volume fraction inside the coagulator calculated using the washout function of an ideal CSTR⁵². Due to the reversibility of the process we expect that these values do not depend on the path followed to reach the specific solid volume fraction considered. This is indeed the case as it can be seen in Fig. 3.6 where all data obtained for different dilution rates as well as for different starting values of the solid volume fraction are shown to collapse in a single curve when plotted as a function of the solid volume fraction. In the same figure we also include the results of an experiment where dilution was performed at a relatively high flow rate of 0.66 L/min (open circles Fig. 3.6), which according to the time scale calculations in the previous section would be too large to ensure equilibrium conditions. It is seen that $\langle R_g \rangle$ does not deviate from the equilibrium while $I(0)$, which is a lower moment of the CMD, does. This is probably consistent with the common observation that the largest aggregates (which affect most the value of $\langle R_g \rangle$) break significantly faster with respect to smaller ones and therefore achieve sooner the equilibrium conditions.

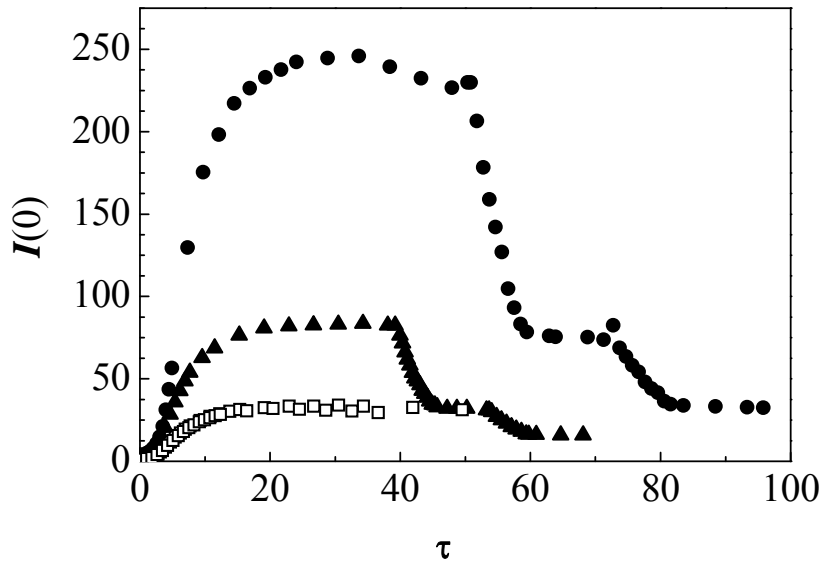


Figure 3.5: Time evolution of $I(0)$ for various values of the initial solid volume fraction for three batch and two dilution experiments; (\bullet) $\phi = 4 \times 10^{-5}$, dilution with $Q_d = 0.31$ L/min, interruptions at $\phi = 2 \times 10^{-5}$ and 1×10^{-5} ; (\blacktriangle) $\phi = 2 \times 10^{-5}$ dilution with $Q_d = 0.22$ L/min, interruption at $\phi = 1 \times 10^{-5}$ and 5×10^{-6} ; (\square) batch experiment with $\phi = 1 \times 10^{-5}$. Stirring speed 635 rpm.

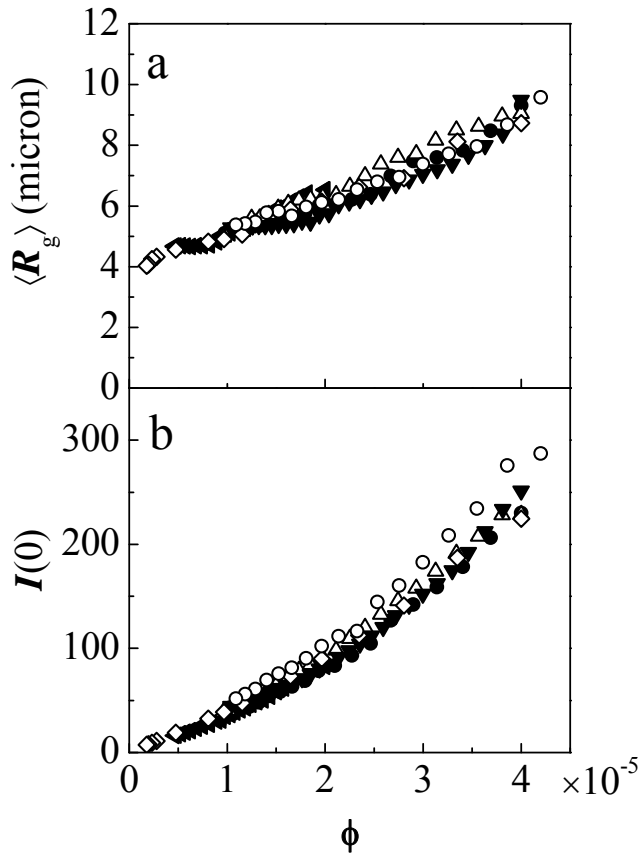


Figure 3.6: Average values of a) $\langle R_g \rangle$ and b) $I(0)$ as a function of the solid volume fraction in the stirred vessel during dilution for starting value of solid volume fraction equal to 4×10^{-5} and various dilution rate: (\circ) $Q_d = 0.66$ L/min, (\diamond) $Q_d = 0.38$ L/min, (\bullet) $Q_d = 0.31$ L/min with interruption, (\blacktriangledown) $Q_d = 0.21$ L/min, (\circ) $Q_d = 0.14$ L/min and starting value of the solid volume fraction $\phi = 2 \times 10^{-5}$ with dilution rate $Q_d = 0.21$ L/min (Ω), stirring speed equal to 635 rpm.

The conclusion above allows us to summarize all the results obtained in this work about the two moments of the CMD at steady state conditions. This is done in Fig. 3.7, where the normalized $\langle R_g \rangle$ and the normalized $I(0)$ (using theoretical values of $I(0)_{t=0}$ from Fig. 3.1a), obtained from both batch and dilution experiments and for two values of the stirring speed (200 and 635 rpm), are shown as a function of the solid volume fraction. We see that the data collapse on two pairs of curves, one for each stirring speed, with the only exception of the normalized $I(0)$ at 200 rpm and $\phi < 2 \times 10^{-5}$. In this case the normalized $I(0)$ values measured in batch experiments are smaller than the corresponding ones obtained in the dilution experiments. This deviation is most likely due to the deposition of aggregates on the walls of the vessel since a very long time (>3hours) was needed for these batch experiments at low stirring speed and solid volume fraction to reach steady state. Influence of deposition was previously discussed in section 2.4.4

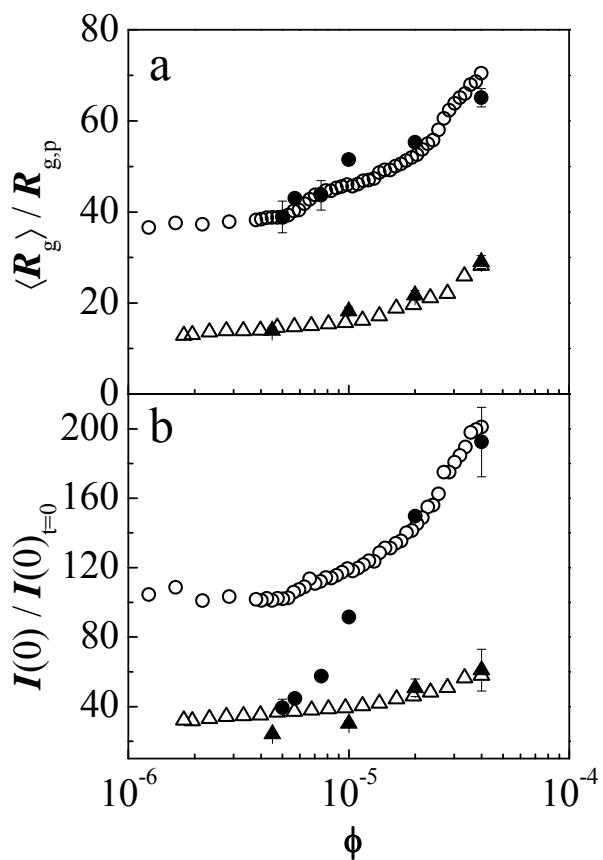


Figure 3.7: Comparison of the values of a) normalized $\langle R_g \rangle$, and b) normalized zero angle intensity $I(0)$ at steady state as a function of solid volume fraction obtained from batch (solid symbols) and dilution (open symbols) experiments; Circles refer to experiments at stirring speed equal to 200 rpm and triangles at 635rpm.

3.4. Critical aggregate size

A notable feature of the dilution experiment is the flattening of the declining trend in $\langle R_g \rangle$ vs. ϕ at low values of solid volume fraction. The data presented in Fig. 3.7 demonstrate that at very low solid volume fractions the value of normalized radius of gyration does not drop down to unity which would correspond to primary particles. Instead, it approaches a certain limiting value dependent on the applied rotation speed which is notably higher than the size of primary particles. This leveling off suggests that the size of aggregates at “infinite” dilution (applying extrapolation of the measured data to $\phi = 0$) is the critical aggregate size for breakage below which effect of breakage is negligible at least within the timescale of the experiment investigated here. A similar observation can be made from experimental results presented by Kobayashi et al.⁴⁰, where they show data indicating that the steady state cluster size approaches a well defined value in the limit of very low solid volume fractions.

In the case when the aggregation process starts from primary particles, one can use the moment ratio M^{ρ} defined as:

$$M = \frac{I(0)/I(0)_{t=0}}{\langle R_g \rangle / R_{g,p}} \quad (3.4)$$

to obtain additional information on breakage dynamics. For the system investigated in this work the moment ratio M initially decreases, reaches a minimum and then increases to the steady state value which depends on the particular operating conditions. The initial decrease of the moment ratio is caused by very fast broadening of the CMD for smaller value of the initial fractal dimension ($d_f < 2$), since at early stages the process is controlled by pure shear aggregation²⁸. As soon as the front of the CMD reaches a certain size where breakage becomes significant, the right hand side of the CMD slows its movement forward and a minimum in the moment ratio M is reached. Shortly after this point $\langle R_g \rangle$ approaches its steady state value and since there is still a large number of small aggregates in the system at this point they further aggregate and therefore $I(0)$ strongly increases towards its steady state value, where a dynamic equilibrium between aggregation and breakage is finally reached. This means that the position of the minimum in the moment ratio M can be used as an indication of when the front of the CMD reaches sizes where the corresponding aggregates are broken at observable rates⁹. However, the broad CMD during the initial aggregation period and the fact that only average quantities of the CMD are accessible limits the applicability of using the $\langle R_g \rangle$ when moment ratio reaches its

minimum to extract the critical aggregate size. In contrast, the CMD at steady state, i.e., during the dilution experiments, is comparatively narrow and therefore assessing the critical aggregate size from the dilution experiments gives more accurate estimates.

In Fig. 3.8 a,b we show the time evolution of $\langle R_g \rangle$ together with the time evolution of the corresponding moment ratio M for batch conditions for both stirring speeds (200 and 635 rpm) investigated here and for the solid volume fraction equal to 4×10^{-5} . A dashed line indicates the normalized $\langle R_g \rangle$ corresponding to the minimum in the moment ratio while the solid line indicates the normalized $\langle R_g \rangle$ obtained from infinite dilution.

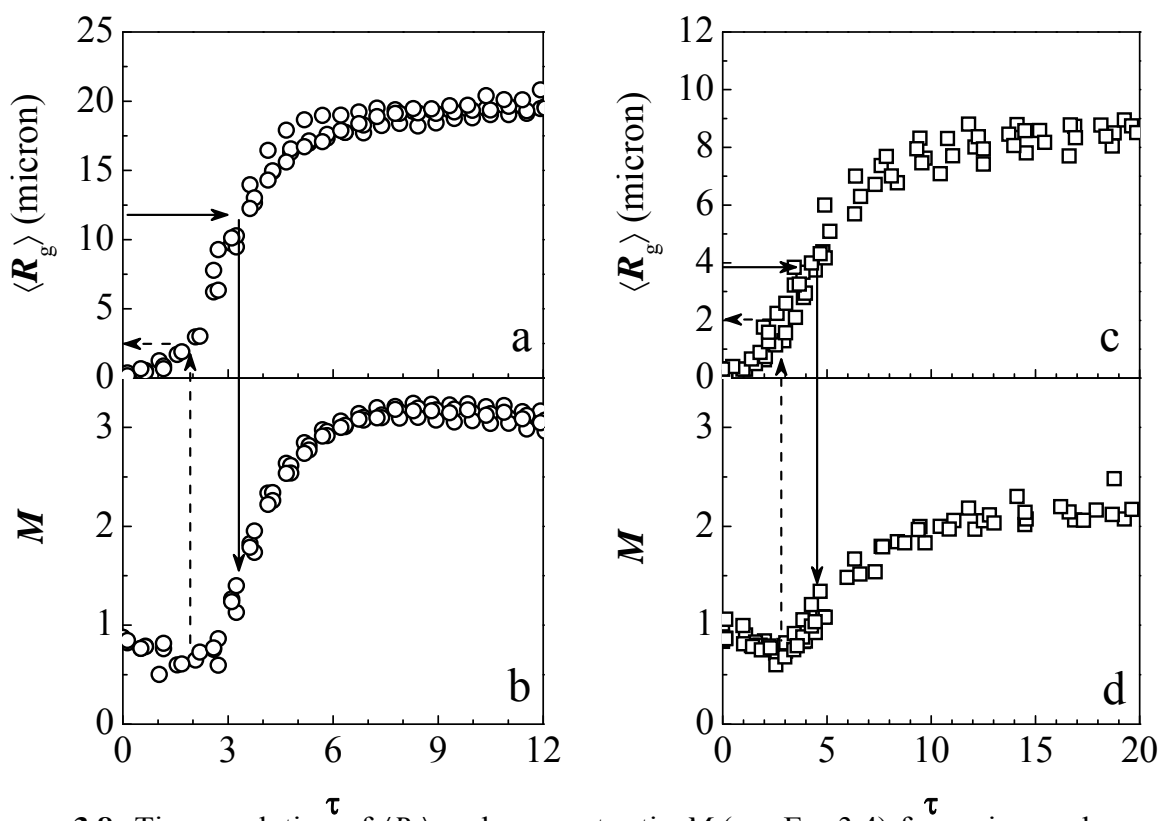


Figure 3.8: Time evolution of $\langle R_g \rangle$ and moment ratio M (see Eq. 3.4) for various values of the stirring speed: a), b) stirring speed 200 rpm; c), d) stirring speed 635 rpm; (dash-line) critical size of aggregates produced from pure aggregation, (solid line) critical size of aggregates obtained for the “infinite” dilution conditions.

3.5. Conclusions and summary

In this work we investigated the effect of the solid volume fraction on the aggregation and breakage processes in turbulent flow in a stirred tank coagulator. Aggregation of fully destabilized polystyrene particles in a batch coagulator yielded steady state distributions with the mean cluster size (in terms of the mean radius of gyration and the zero angle intensity measured by small angle static light scattering) monotonically increasing with the solid volume fraction. Using a combination of batch operation and continuous dilution with particle-free solution in the stirred tank, it was found that the steady state distributions were fully reversible upon changing the solid volume fraction. This indicates that the steady state distribution in this system is controlled by the dynamic equilibrium between aggregation and breakage. The reversibility of this dynamic equilibrium and timescale analysis were combined to design a novel efficient experimental technique to obtain the dependency of steady state cluster mass distribution over a wide range of solid volume fractions in a single experiment, i.e. the continuous dilution experiment. In addition, using this type of experiment at very low solid volume fractions it is possible to obtain a critical aggregate size below which breakage rates become negligible.

4. Effect of shear rate

4.1. Introduction

The shear rate, i.e. the velocity gradient, is one of the most accessible and important variables to control the outcome of flow-induced aggregation. This variable corresponds to the rotation speed in the coagulator used as a model system in the present work. By changing the rotation speed one changes the energy dissipation rate, with the local energy dissipation rate related to the local shear rate as per Eq. 1.5. From the local shear rate data obtained from CFD one can calculate a volume averaged shear rate that is sufficient to characterize aggregation for the diluted conditions studied in this thesis⁵⁴.

In this chapter, we present a thorough study of the effect of rotation speed on aggregate size and structure. We begin by investigating the dependency of aggregation efficiency on shear rate. Then we examine the structure of aggregate using two techniques, SASLS and analysis of CSLM images. The previous two aspects were studied using batch experiments similar to those discussed in section 3.2 but with varying the rotation speed from an experiment to another while conducting the whole series of experiments using the same solid volume fraction. Following these batch experiments, we carried out dilution experiments to study the dependency of the critical aggregate size on shear rate. Force balance was used to estimate the cohesive force holding the aggregate together at the critical aggregate size. Furthermore, we studied the response of the system to steps and ramps in the rotation speed in order to examine the reversibility of the system and provide an equivalent to the dilution experiments that can provide the dependency of CMD on a range of shear rates in one experiment, i.e., the ramp experiment. We finish the chapter by presenting the scaling between average size at steady state and the shear rate.

4.2. Batch experiments and aggregation efficiency

Since, at the beginning, the CMD is controlled only by aggregation, starting from a monodisperse distribution of primary particles and measuring the number concentration of doublets enables one to evaluate the dependency of the aggregation efficiency on the shear rate. Unfortunately, this dependency was experimentally investigated only for specific type of flow

and relatively large size of primary particles such as for laminar conditions using micro-tubes and primary particles of 2 μm in diameter⁵⁸ or for turbulent conditions generated by grid vibration and primary particle size equal to 3.9 μm ⁵⁹. Based on these measurements as well as on several theoretical studies^{8, 26, 60-62}, it was found, that the aggregation efficiency depends weakly on the shear rate with a power law exponent in the range between -0.23 and -0.14. As the aggregates grow and become large enough, another mechanism, i.e., breakage, becomes active and slows down the fast initial growth. Shortly after this, the process reaches a steady state, which predominantly depends on size and concentration of the primary particles, see previous chapter, composition of the liquid phase, see next chapter, type of coagulant, and value and distribution of the shear rate in the vessel. Such a steady state arises, when aggregation and breakage balance each other.

Let us first start with the aggregation experiments performed in batch mode, i.e., the dilution pump in Fig. 2.2 is switched off. In these experiments the effect of stirring speed (i.e., shear rate) in the range from 200 to 1073 rpm, see Table 2.1, on the initial aggregation kinetics as well as on the steady-state conditions was investigated. For all experiments aggregation started from a well-stirred stable suspension of primary particles at a solid volume fraction equal to 4×10^{-5} . By injecting the required amount of coagulant into the coagulator the particles became fully destabilized and aggregation started. The consequent cluster growth was monitored on-line by the SASLS instrument using the recirculation technique described in chapter 2. From the measured $I(q)$ the time evolution of the two moments of the CMD, namely the rms radius of gyration and the zero-angle intensity, as well as the scaling exponent, were evaluated.

The obtained results of the initial kinetics for both moments of the CMD are shown in Fig. 4.1 a, b as a function of the dimensionless time of shear aggregation, $\tau = t \langle G \rangle \phi$. It can be seen, that the initial growth rate of both moments of the CMD investigated here decreases with increasing shear rate. This differs from the results of our previous work²⁸, where, using the same primary particle size, we found that the values of the initial kinetics measured at different solid volume fractions fall on the same curve when plotted as a function of τ .

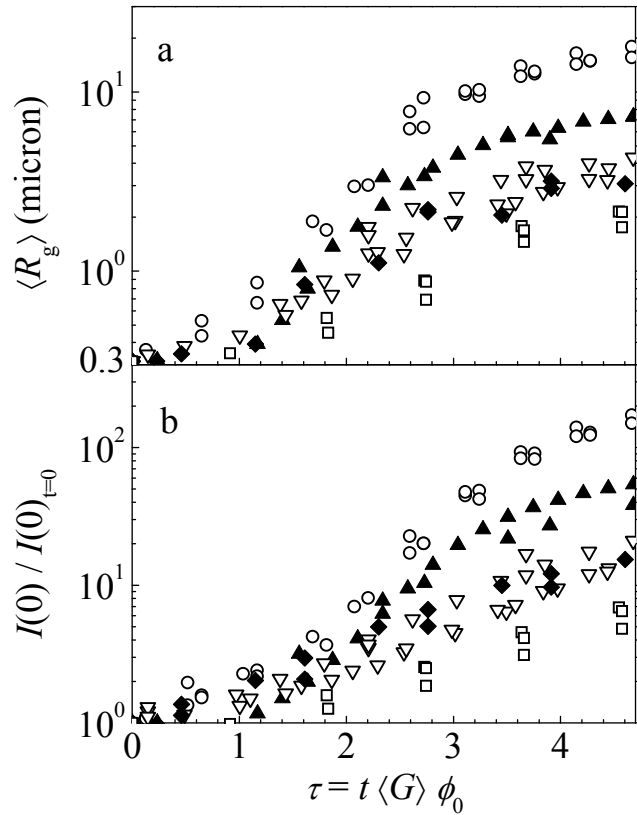


Figure 4.1: Average radius of gyration $\langle R_g \rangle$ (a) and normalized zero angle intensity $I(0)$ (b) as a function of dimensionless time, τ during batch experiments for a solid volume fraction equal to 4×10^{-5} and various values of the stirring speed; (○) 200 rpm, (▲) 417 rpm, (▽) 635 rpm, (◆) 854 rpm, (□) 1073 rpm

Based on those data we concluded that the initial kinetics is controlled only by one mechanism, i.e., shear aggregation, and breakage was not effective. However, the data shown in Fig. 4.1a, b where the shear rate has been varied and the kinetic curves do not overlap contradict this conclusion. There are three possible explanations of this observation. One could be, that for the system investigated here breakage starts to affect the system earlier, i.e., at smaller cluster sizes for higher stirring speeds. Another reason could be Brownian aggregation, which is, however, very weak for the large particles used in this work. The unimportance of Brownian aggregation is demonstrated later by estimation of Peclet number. A third reason could be, that the difference in the scaling of the initial kinetics is due to a weak inverse proportionality of collision efficiency to shear rate, which was actually found in several previous studies^{8, 26, 59-63}. This proportionality results in a dependency of the aggregation kinetics on the shear rate with an exponent slightly smaller than unity.

To estimate the effect of Brownian with respect to shear aggregation it is possible to calculate the Péclet number, $Pe = \frac{6\pi\mu\langle G\rangle R_p}{k_B T}$, defined as the ratio of time scales between diffusive and convective transport. Taking into account the size of primary particles, liquid properties as for water at 25 °C and values of the shear rate from Table 2.2, primary particle Péclet numbers in the range from 30 to 370 were obtained. This indicates that the effect of Brownian aggregation is negligible.

On the other hand, as can be seen in Fig. 4.1a, b the initial growth rate for both moments start to deviate almost immediately after the aggregation process started. Taking into account the breakage experiments of Sonntag and Russel^{64, 65} as well as our previous data²⁸, where maximum stable aggregates (not affected by breakage) of at least 2 microns in diameter were observed, we can conclude that the presence of breakage at the very beginning of the process is not realistic. In addition, this assumption is supported by our later results as will be seen from the discussion of the dilution experiments in the context of Fig. 4.10.

Therefore, the most realistic reason for the deviation of the initial kinetics from the same curve is due to the dependency of the collision efficiency on the shear rate. If this would be the case, then in order to obtain a scaling of the initial kinetics with respect to shear rate, a modified dimensionless time of the form $\tau_M = \alpha(N_F)t\langle G\rangle\phi$, where $\alpha(N_F) = C(A_H/\mu G R_p^3)^{-b}$, should be used. Such a scaling, using the prefactor, C , equal to 0.5 according to van de Ven and Mason⁶³,

a Hamaker constant, A_H , equal to 1×10^{-20} J⁶⁶, and a value of the exponent, b , equal to 0.18 is shown in Fig. 4.2a-d. The value of b was found to give the best scaling of the initial kinetics for both measured moments of the CMD. As one can see, using this modified “dimensionless” time, τ_M , better agreement of initial kinetics measured for various shear rates (at least within the experimental error) till approximately $\tau_M = 0.75$ is obtained. Moreover, comparing the obtained value of b with those published in the literature, either from numerical or experimental studies of initial aggregation kinetics, with values in the range from 0.14 to 0.23^{8, 26, 59-63}, we found good agreement. To provide additional support to this findings, we plot the time evolution of the moment ratio, M , defined in Eq. 3.2⁹ as a function of modified dimensionless time, τ_M . From its definition M , contains information about the change of the shape of the CMD, i.e., its broadness, while its time evolution would be significantly affected by the presence of Brownian aggregation or breakage^{9, 67}. For the system considered in Fig. 4.2a-d, the corresponding time evolution of M is shown in Fig. 4.3. It can be seen that, within the experimental error, the initial decay in M is identical for all investigated conditions, but once the minimum is reached the further time evolution differs for various stirring speeds. As discussed in detail by Soos et al.⁹, this behavior is typical for systems where Brownian aggregation, as well as breakage, is not relevant and the system is controlled only by one mechanism, i.e., shear aggregation. This further supports the conclusion that the deviation of the initial time evolution for both moments of the CMD shown in Fig. 4.2a-d is caused by an aggregation efficiency being inversely proportional to shear rate.

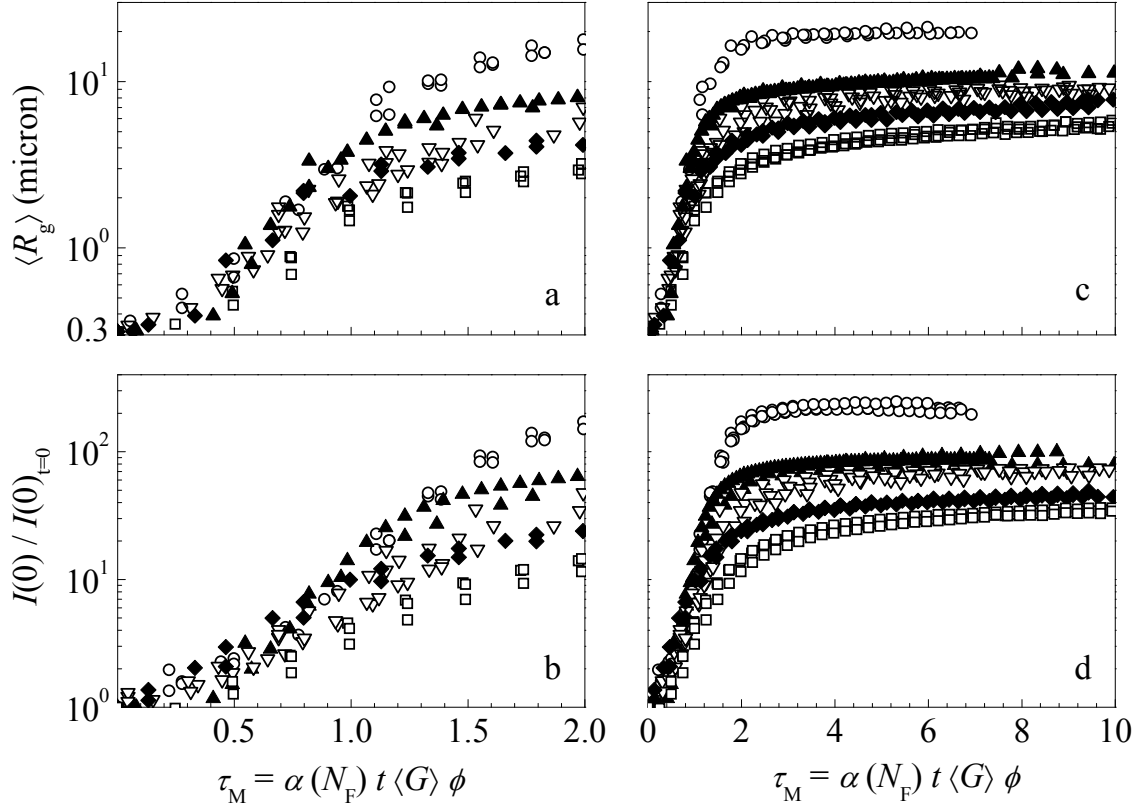


Figure 4.2: Average radius of gyration $\langle R_g \rangle$ (a,c) and normalized zero angle intensity $I(0)$ (b,d) as a function of dimensionless time, τ_M during batch experiments for a solid volume fraction equal to 4×10^{-5} and various values of the stirring speed; (○) 200 rpm, (▲) 417 rpm, (▽) 635 rpm, (◆) 854 rpm, (□) 1073 rpm

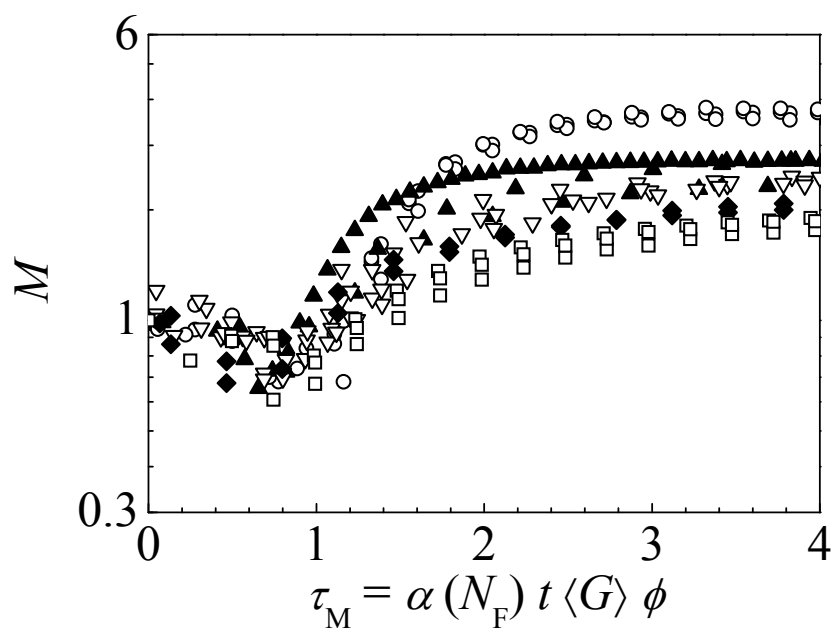


Figure 4.3: Moment ratio M , defined as the ratio between the normalized zero angle intensity and the normalized radius of gyration as a function of dimensionless time, τ_M for the batch experiments shown in Fig. 4.1 with a solid volume fraction equal to 4×10^{-5} and various values of the stirring speed; (○) 200 rpm, (▲) 417 rpm, (▽) 635 rpm, (◆) 854 rpm, (□) 1073 rpm

Thus, the shape of the CMD during the initial stage of the process is similar for all investigated shear rates until the point where the moment ratio reaches its minimum^{9, 67}. At this time, the largest clusters reach sizes where breakage becomes significant and, therefore, their growth rate decreases. However, since there is still a large number of small aggregates in the system, which can further aggregate, $I(0)$ increases sharply in time, and consequently also M increases. Shortly after this point both moments of the CMD approach their steady state. As can be seen from Fig. 4.2c, d the obtained steady-state values of both moments of the CMD strongly depend on shear rate, where a significant decrease of the steady-state values of both moments with increasing the stirring speed is found. It is worth mentioning that a similar dependency of the steady state on the applied shear rate, although mostly in terms of a single moment of the CMD, has been reported by many other authors for various sizes and concentrations of primary particle^{19-21, 23, 26, 40, 47, 48, 51, 68-73}

As mentioned earlier another piece of information that can be extracted from the light scattering measurement, i.e., from the slope of $S(q)$ vs. q in the log-log plot, is the scaling exponent, SE . Fig. 4.4 shows a comparison of $S(q)$ at steady state for three different stirring speeds (200, 635 and 1073 rpm) together with the measured form factor of the primary particles. It can be seen that an increase in stirring speed results in a decrease in the value of SE as well as in aggregate size, corresponding to a shift of the bending part of $S(q)$ towards smaller q -values, (see Fig. 4.4). The SE values for all the experiments shown in Fig. 4.2a-d are shown as a function of the dimensionless time, τ_M , in Fig. 4.5. It is seen that the time evolution of SE exhibits a rather similar shape for various stirring speeds with significant differences only in the steady-state values. Considering the time evolution of the two moments of the CMD, $\langle R_g \rangle$ and $I(0)$, shown in Fig. 4.2a-d, one can see that once both of them reach a steady state also the SE value approaches its steady-state value.

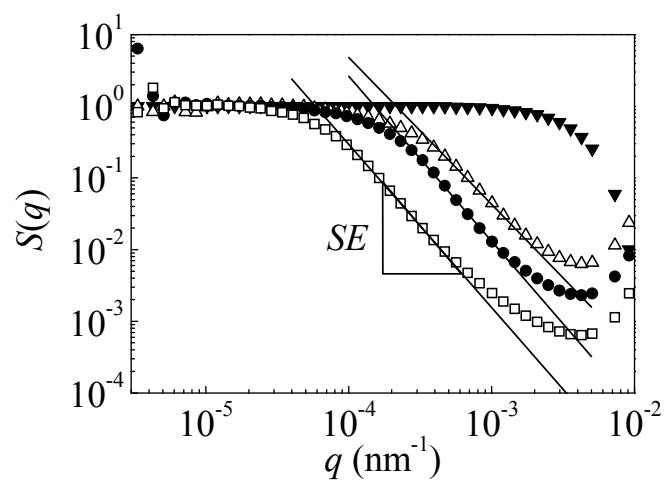


Figure 4.4: Comparison of the steady-state structure factors measured for a solid volume fraction equal to 4×10^{-5} and various stirring speeds; (\square) 200 rpm, (\bullet) 635 rpm and (\triangle) 1073 rpm. In the same figure is also plotted the form factor of the primary particles, $P(q)$ (\blacktriangledown).

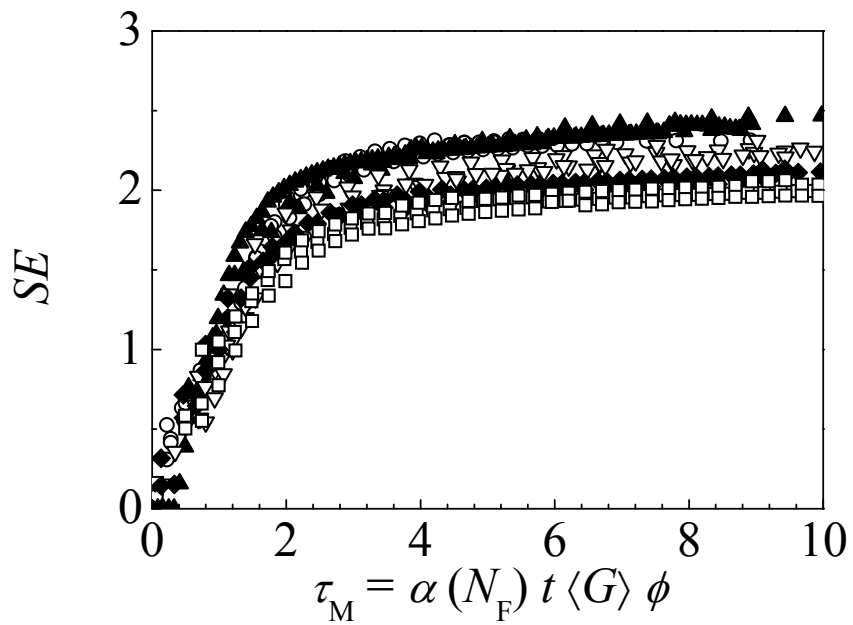


Figure 4.5: Values of the scaling exponent, SE as a function of the dimensionless time, τ_M for the batch experiments shown in Fig. 4.2 with a solid volume fraction equal to 4×10^{-5} and various values of the stirring speed; (\circ) 200 rpm, (\blacktriangle) 417 rpm, (∇) 635 rpm, (\blacklozenge) 854 rpm, (\square) 1073 rpm

The low value of the scaling exponent at the very beginning of the process, also observed by other authors^{27, 51}, is caused by the presence of a significant fraction of small non-fractal aggregates (singlets and doublets), whose scattering behavior is rather different from that of large fully developed fractal clusters⁴⁹. The same is true also for experiments performed at high stirring speeds, where breakage does not allow the formation of large clusters and an increasingly large fraction of small non-fractal aggregates leads to a decrease of SE with increasing stirring speed. A more detailed analysis of aggregate structures presented in the following section.

4.3. Analysis of aggregate structure

An open issue refers to the effect of the shear rate history on steady-state characteristics of aggregates. In one case, when a precipitated/polymeric flocculant was used^{55, 57, 72, 74-76}, it was found that the morphology and the size of aggregates strongly depend on how the shear rate was varied before reaching the steady state. In another case, when strong electrolyte was used as coagulant^{26, 28}, the effect of the shear rate on the reversibility of the steady state was not observed. This would indicate that in this case the morphology is the same, independent of the applied shear rate. However, although using strong electrolyte both, a shear rate independent morphology with fractal dimension in the range from 2.2 to 3^{19, 20, 43} dependency of the fractal dimension on the shear rate covering the range of values from 2 to 2.9 was also observed^{50, 51}. One possible reason for this discrepancy is that various researchers use different experimental techniques to analyze the structure of aggregates without paying enough attention to their suitability for the particular problem under examination.

Since the size of the primary particles is substantially larger than the laser wavelength of our SASLS instrument the structure of the aggregates cannot be accurately determined from the power-law region of the structure factor. Therefore, the structure was independently characterized through image analysis of 2D images of aggregates obtained by confocal laser scanning microscopy (CLSM). From 2D images one can obtain the projected surface area, A , and the perimeter, P , of the binary image of an aggregate. A and P scale according to Eq. 4.1¹⁸⁻²⁰

$$A \propto P^{2/d_{\text{pt}}} \quad (4.1)$$

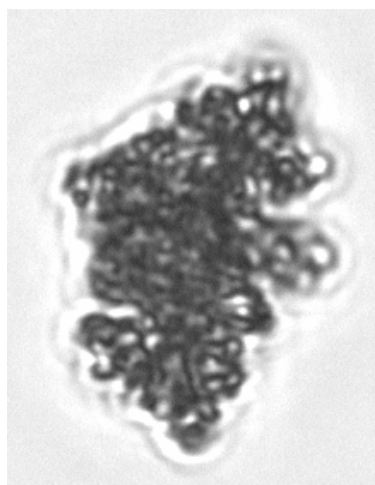
where d_{pf} is the perimeter fractal dimension. We used the correlation of Lee and Kramer, developed from analyzing aggregates with different size and structure generated by Monte Carlo method.²⁴ to relate d_{pf} and the mass fractal dimension, the one measured by light scattering.

In Figure 4.6a, b are shown examples of the images of aggregates obtained from CLSM and scanning electron microscopy (SEM) for a batch experiment at 200 rpm and a solid volume fraction equal to 4×10^{-5} . It can be seen that the obtained aggregates are highly compact with slightly elongated shape. As SEM pictures require drying of the samples, and this could lead to structural changes of the aggregates, in the following analysis we consider only CLSM images of the aggregates. The scaling of the projected area vs. perimeter of the aggregates, obtained by image analysis of approximately 60 pictures for each experiment, was used to characterize the aggregates structure. Results for three stirring speeds (200, 635, and 1073 rpm) are shown in Fig. 4.7a-c. We note that the results for 200 rpm include some experiments where the stirring speed was changed stepwise as it will be discussed later in the context of Fig. 4.11. As can be seen, all data can be well approximated by a power-law scaling, where according to Eq. 4.1 the slope is equal to $2/d_{pf}$. The obtained value of the perimeter fractal dimension is equal to 1.214 ± 0.025 over the whole range of stirring speeds investigated here. This is in agreement with values of perimeter fractal dimension measured by other authors using different sizes of primary particles^{18-20, 22, 23, 57}.

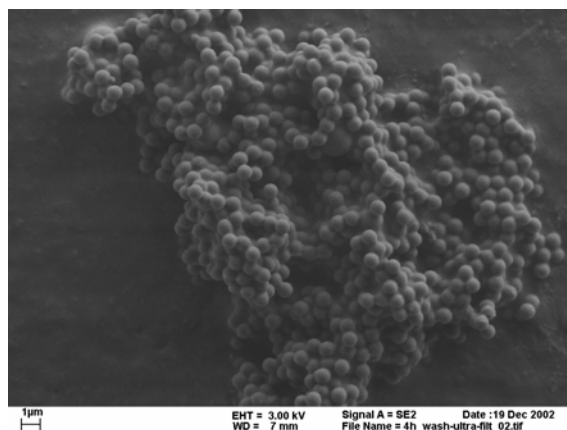
A comparison of the SE values obtained from a measured $S(q)$ with the fractal dimension d_f calculated from the d_{pf} value above using the correlation developed by Lee and Kramer²⁴ is shown in Fig 4.8. It can be seen that the SE values are significantly smaller than the d_f values obtained from CLSM image analysis in the whole range of stirring speed, and their difference tends to increase with increasing stirring speed. On the other hand, the d_f values estimated from the perimeter fractal dimension stay rather constant and equal to 2.62 ± 0.18 which is in agreement with the values published in the literature using different types of stirring devices and size of primary particles^{26, 47, 57}. It is worth noting that the fractal dimension is one of the parameters used in the modeling of coagulation processes and its knowledge, which can not be correctly obtained from the SASLS measurements for the system investigated here, is essential.

Another piece of information that can be obtained from image analysis is the shape of the aggregates. In Fig. 4.9a-c the distribution of the aspect ratio of the population of aggregates, defined as the ratio between major and minor axis of the best fitted ellipse, for three different

stirring speeds (200, 635, and 1073 rpm) is shown. It is seen that, in all cases the shape of the aggregates is non-spherical, with an aspect ratio covering the range from 1 to 2.6. This is in agreement with data published by Blaser⁷⁷⁻⁷⁹, for aggregates generated from silica and styrene/acrylate copolymer primary particles, yielding aspect ratios in the range from 1.6 to 2.86.



a



b

Figure 4.6: Examples of aggregates images obtained at steady state for a solid volume fraction equal to 4×10^{-5} and a stirring speed equal to 200 rpm; (a) raw image from CLSM (b) SEM picture

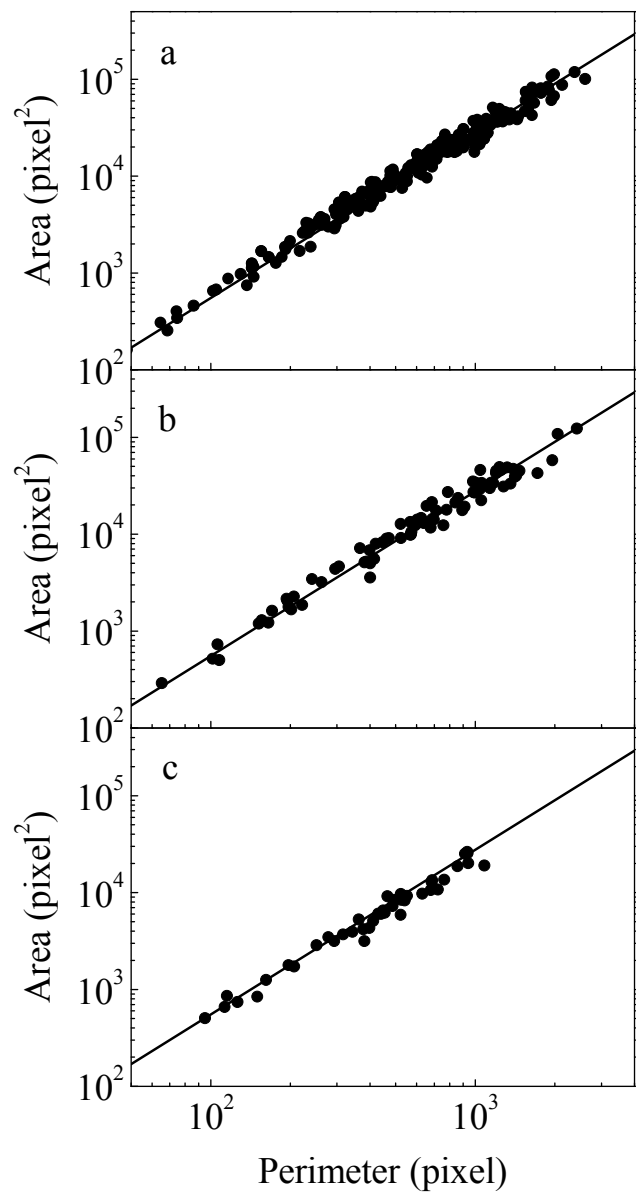


Figure 4.7: Relationship between area (A) and perimeter (P) obtained from CLSM image analysis of samples taken at steady state for a solid volume fraction equal to 4×10^{-5} and various stirring speeds; (a) 200 rpm, (b) 635 rpm and (c) 1073 rpm

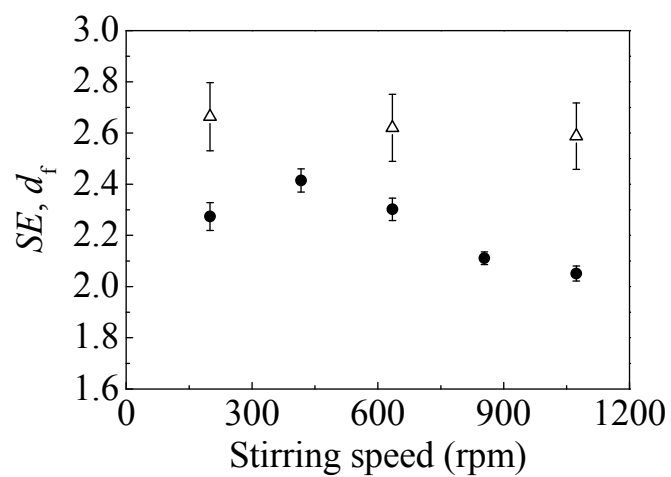


Figure 4.8: Comparison of the scaling exponent, SE , estimated from the power law region of the structure factor with the fractal dimension, d_f , (both at steady state) calculated from the perimeter fractal dimension obtained from image analysis, using the relation developed by Lee and Kramer²⁴ for a solid volume fraction equal to 4×10^{-5} and various values of the stirring speed; (●) SE , (△) d_f

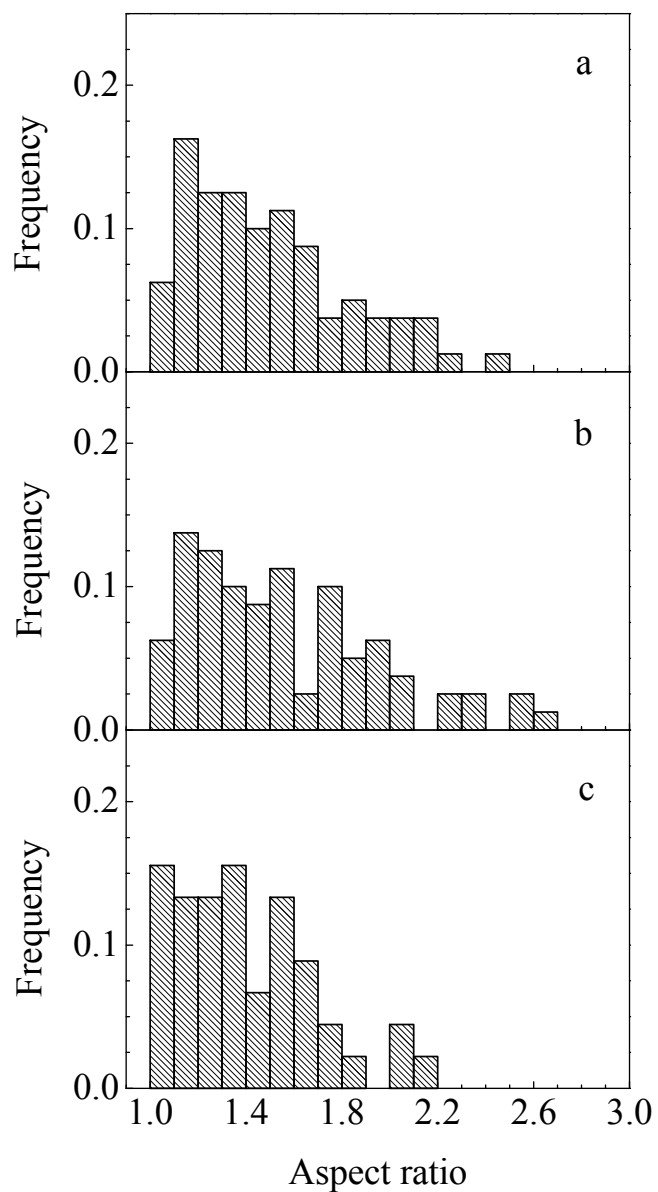


Figure 4.9: Comparison of the distributions of the aggregates aspect ratio at steady state estimated from the CLSM images for a solid volume fraction equal to 4×10^{-5} and various values of stirring speed; (a) 200 rpm, (b) 635 rpm and (c) 1073 rpm.

4.4. Dilution experiments and critical aggregate size

4.4.1. Force balance and estimation of Aggregate cohesive force

A simple model to interpret the breakup of an aggregate in liquid suspension is based on the assumption that breakage of an aggregate occurs when the hydrodynamic forces, F_{hyd} , acting on the aggregate overcome the cohesive forces holding it together, F_{coh} . This cohesive force comprises information about aggregate internal structure, i.e., about fragments size, and number and strength of individual bonds holding them together. These factors are affected by the hydrodynamic conditions in the vessel, the composition of the liquid phase (i.e., type of coagulant) and the primary particles material and surface properties. Therefore, the knowledge of the aggregate cohesive force is of fundamental importance. There are two ways how one can obtain this information: i) direct measurement by manipulation of micron scale aggregates or ii) indirect evaluation via a balance between the forces acting on the aggregate when breakage occurs.

Direct measurement of the aggregate cohesive force was performed by Yeung and Pelton⁸⁰ by pulling apart single aggregates of various sizes and structure. They have shown that the aggregate cohesive force does not depend on the size of the ruptured aggregates. Moreover, based on a conservation of mass approach they found that aggregates with smaller fractal dimension ($d_f = 1.8$) are broken into fragments with approximately equal mass, whereas aggregates with larger fractal dimension ($d_f = 2.4$) were broken into fragments with different masses.

A widely accepted method, to indirectly evaluate the aggregate cohesive force, is to run breakage experiments under dilute conditions, so that aggregation can be neglected, and to measure the size of the largest clusters which withstand given hydrodynamic conditions^{72, 81-83}. The cluster size together with the known hydrodynamic characteristics (i.e., the shear rate) is consequently used to evaluate the hydrodynamic force acting on the clusters. When the aggregate size is below the Kolmogorov micro-scale, defined as:

$$\eta = \left(\frac{\nu^3}{\varepsilon} \right)^{1/4} \quad (4.2)$$

where ν is the kinematic viscosity and ε is the energy dissipation rate, the maximum hydrodynamic force acting on a spherical particle under simple shear flow^{75, 82, 84} is equal to

$$F_{\text{hyd}}^{\text{VS}} = \frac{5}{8} \pi \mu d^2 G \quad (4.3)$$

where μ is the dynamic viscosity, d is the particle size, and G is the characteristic velocity gradient, or shear rate, related to the energy dissipation rate within the smallest eddies through $G = \sqrt{\varepsilon/\nu}$ ⁸⁵.

However, when the aggregate size is above the Kolmogorov micro-scale and the aggregates are in the inertial sub-range of turbulence, the hydrodynamic force acting on a spherical particle is equal to ^{75, 86}

$$F_{\text{hyd}}^{\text{IS}} = \frac{3}{2} \rho C_1 \varepsilon^{2/3} d^{8/3} \quad (4.4)$$

with C_1 equal to 0.73 ⁸⁷.

In chapter 3²⁸, see we have proposed a dynamic experiment using continuous dilution of the content of the tank in order to investigate aggregation/breakage dynamics. In particular, once the aggregation system reaches steady state, the content of the vessel is continuously diluted with a particle-free salt solution. The dilution rate is selected so that the characteristic time of mixing is smaller than both the characteristic times of aggregation and dilution, which ensures that the flow pattern and concentration profile in the tank during aggregation are close to those in an ideal continuous stirred tank reactor (CSTR) ⁵², i.e., the solid volume fraction is uniform in the entire tank. Moreover, to ensure that a dynamic equilibrium between aggregation and breakage is achieved at every single time during the dilution experiment, the aggregation time scale has to be smaller than that of dilution. Since in the experiments under consideration both these criteria are satisfied ²⁸, we obtain the steady-state CMD, in our case represented by its two moments, $\langle R_g \rangle$ and $I(0)$, as a function of the actual solid volume fraction in the vessel. In Fig. 4.10a, b these two moments are shown as a function of the solid volume fraction, ϕ , for various values of the stirring speed. These data were collected from dilution experiments starting from the steady-state conditions corresponding to a solid volume fraction, ϕ , equal to 4×10^{-5} .

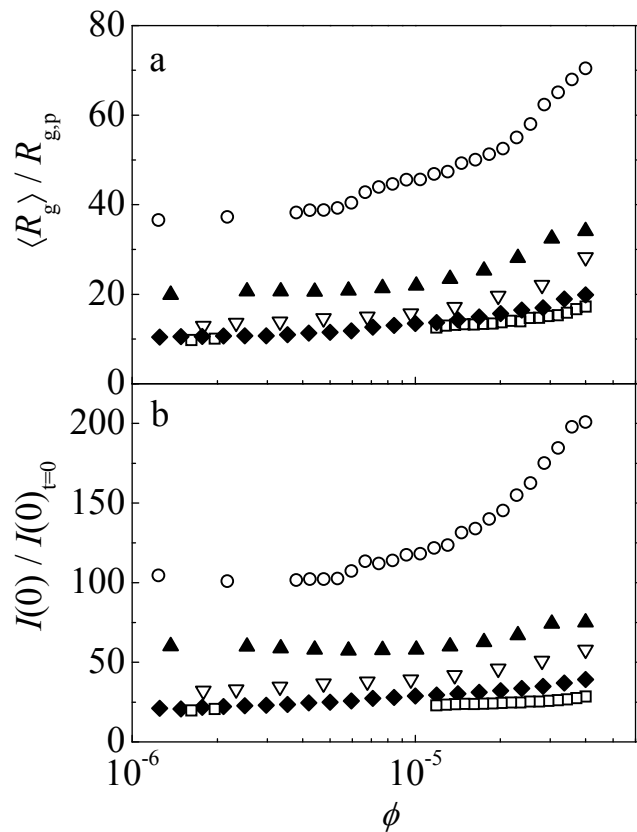


Figure 4.10: Normalized radius of gyration (a) and normalized zero angle intensity (b) as a function of the solid volume fraction for various values of the stirring speed at steady state; (○) 200 rpm, (▲) 417 rpm, (▽) 635 rpm, (◆) 854 rpm, (□) 1073 rpm

In Fig. 4.10b the zero angle intensity is normalized by the theoretical values of $I(0)_{t=0}$ which correspond to the actual solid volume fraction, taking into account the effect of multiple scattering²⁸. From the data in Fig. 4.10a, b, it is seen that as the solid volume fraction approaches zero both moments level off and approach a certain limit. Since in this case no aggregation is present, the size of the aggregates is solely determined by their strength, i.e., aggregates of smaller size cannot be broken by the given hydrodynamic conditions²⁸.

From these data we can estimate the aggregate cohesive force, but before this, it is necessary to determine whether aggregate breakage occurs in the viscous or in the inertial sub-range of turbulence. As one can see from the comparison of the aggregate sizes ($2\langle R_g \rangle$ using data from Fig. 4.10 at infinite dilution) with values of the corresponding Kolmogorov micro-scale (both average and minimum), under all conditions investigated in this work (see Table 2.2), the maximum size of the aggregates is within the viscous sub-range. Therefore, approximating the aggregate shape as spherical with very compact structure (Fig. 4.6) it is possible to approximate the absolute value of the aggregate cohesive force, defined as to be equal to the overall hydrodynamic force acting on a sphere of same diameter as the smallest stable aggregate as obtained from infinite-dilution experiment using Eq. 4.3. Since, at these stirring conditions mixing as well as breakage are very fast^{64, 65}, we can assume that every aggregate experienced at least once the highest values of the shear rate in the vessel, and therefore the maximum size of the aggregates is controlled by the highest value of the shear rate in the vessel. Using such aggregates diameter equal to $2\langle R_g \rangle$ as measured under infinite-dilution conditions and the highest value of the shear rate shown in Fig. 2.13, the value of aggregate cohesive force is equal to 6.2 ± 1.0 nN, independent of the aggregate size. It is worth noting that the obtained scatter in aggregate cohesive force results from the experimental error in the steady-state value of $\langle R_g \rangle$, which is equal to about 15 %. Values of the aggregate cohesive force measured by other authors, using different size and material of primary particles as well as different experimental units under conditions where aggregation can be neglected, range from 0.01 to 10 nN with no dependency on aggregate size^{40, 64, 83, 88, 89}. Comparing these values with the value of aggregate cohesive force obtain in our analysis we found good agreement.

It is worth noting that using precipitated salts or polymer as flocculant, as it is the case for the data reported by Tambo and Hozumi ⁷², Blaser ^{78, 79}, and the direct measurement of the rupture force presented by Yeung et al. ⁸⁰, the aggregates cohesive force is significantly higher and values two to three orders of magnitude larger than those obtained in this work were observed. This large increase in aggregate cohesive force is related to the fact that primary particles inside such flocs are kept together by a combination of van der Waals forces and solid or adhesive bridges formed by the precipitated salts or the polymeric flocculant.

4.5. System response to the step and ramp changes in the stirring speed

As discussed in the previous chapter, the steady state of the system is completely reversible with respect to variations of the solid volume fraction. In the following, we investigate the reversibility behavior of the system with respect to dynamic variations of the stirring speed. First, starting from a given steady state we monitor the response of the system to step changes in the stirring speed using the on-line light scattering measurement technique. The flow rate inside the loop, controlled by the circulation pump, is altered so as to keep the average shear rate in the loop smaller than that in the tank yet with the residence time too short to allow for significant aggregation in the loop. The obtained results for several step changes of the stirring speed are shown in Fig. 4.11a, b. It can be seen that the steady-state values of both moments of the CMD are independent of the applied shear rate history, proving complete reversibility of the steady state. This clearly appears by comparing the steady-state values achieved at 200 and 1073 rpm after different sequences of step changes.

Moreover, the results in Fig.4.11a, b show that increasing the stirring speed leads to a much faster response of the system than decreasing the stirring speed. This reflects the different kinetics of aggregation and breakage. Similar observations with respect to shear rate variations were reported by other authors using colloidal polymer particles destabilized with strong electrolytes ²⁶. On the other hand, as shown in ^{55-57, 76}, in systems where a precipitating solid (i.e., Fe(OH)₃) or a polymer are used as coagulant, the suspension may exhibit different aggregation dynamics, i.e., in such systems a full reversibility is not found. In this case, the coagulant may modify the internal structure of the aggregates, increase the aggregate cohesive force over time, and make them more resistant against shear stress.

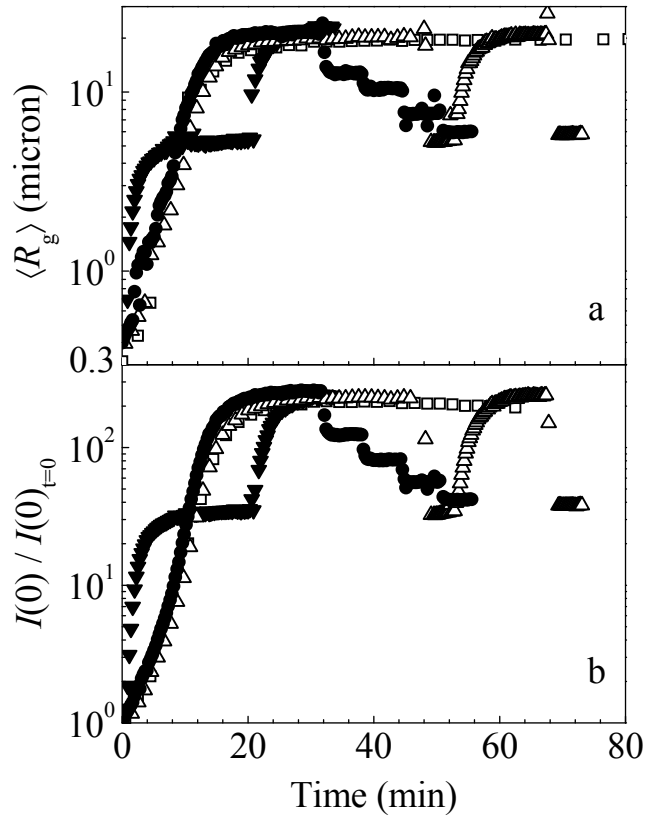


Figure 4.11: Time evolutions of the radius of gyration $\langle R_g \rangle$ (a) and normalized zero angle intensity $I(0)$ (b) during step changes of the stirring speed measured for a solid volume fraction equal to 4×10^{-5} ; (●) 200 – 417 – 635 – 854 – 1073 rpm, (□) 200 rpm, (▼) 1073 – 200 rpm, (△) 200 – 1073 – 200 – 1073 rpm

Having checked the complete reversibility of the steady state, and following the same concept as in the dilution experiment ²⁸, one would expect that when the stirring speed is changed slowly enough, the aggregation and breakage processes can readjust the CMD so as to reach a new steady state faster than any significant variation of the stirring speed occurs. Then, it is possible to obtain the steady-state CMDs as a function of stirring speed from only one experiment through a continuous, slow variation of the stirring speed. Let us consider the experiment in Fig. 4.11a, b where the stirring speed was reduced from 1073 to 200 rpm (solid down triangles) and estimate the characteristic time-scale of the various involved processes. The characteristic time-scale of aggregation at steady-state conditions, including the dependency of the collision efficiency on the shear rate obtained above, is given by Marchisio et al⁵⁴:

$$\tau_A = \frac{1}{\alpha(N_F) G (R_{c,i} + R_{c,j})^3 N} \quad (4.5)$$

where $\alpha(N_F)$ is the collision efficiency equal to $C(A_H/\mu G R_p^3)^{-b}$, $R_{c,i}$ and $R_{c,j}$ are the collision radii of aggregates, and N is the number concentration of aggregates, ($N = \phi_0/V_p i$). The value of the collision efficiency, $\alpha(N_F)$, using C equal to 0.5, ⁶³ a Hamaker constant, A_H , equal to 1×10^{20} J ⁶⁶, and b equal to 0.18, was calculated for each shear rate. The volume average shear rate was calculated using the CFD software FLUENT (see Table 2.2). Since we do not have complete information about the CMD at steady state, in order to evaluate τ_A we used the value of $\langle R_g \rangle$ measured experimentally as collision radii $R_{c,i}$ and $R_{c,j}$. The number concentration of aggregates, N , at steady state has been computed from their average mass, i , which was estimated using $\langle R_g \rangle$ as their average size and the value of fractal dimension (equal to 2.62) obtained from image analysis. The obtained values for the aggregation timescale, τ_A , are 13 s at 1073 rpm, 20 s at 635 rpm, 30 s at 417 rpm, and 60 s at 200 rpm. We note that, since in evaluating the time-scale of aggregation the CMD at steady state was approximated as monodisperse, the obtained values should provide an upper bound of the real one. Based on these data, it was concluded that a change of the stirring speed equal to 30 rpm/min is sufficiently slow to allow equilibration between aggregation and breakage to be reached at every single instant in time. The results of this experiment are shown in Fig. 4.12a, b. Initially, the system was stirred at 417 rpm until steady state was achieved, which happens at about $t = 30$ min. At this point the stirring speed was

increased at a rate of 30 rpm/min until 1073 rpm for about 20 min, indicated as “ramp1” in Fig. 4.12. The system was then kept unchanged for 5 min after which a similar but decreasing ramp was applied, indicated as “ramp2” in Fig. 4.12, to go back to the original stirring speed of 417 rpm. It is worth noting that when we stopped changing the stirring speed and kept it at 1073 rpm for 5 min (at $t = 50$ min), the change in the measured moments also stopped immediately, thus confirming that the change in stirring speed is dominating the system dynamics, while aggregation and breakage equilibrate each other at every single point in time. The fact that the changes in the CMD moments shown in Fig. 4.12 are symmetric in ramp1 and ramp2, indicates reversibility of the system for the selected acceleration/deceleration of the stirring speed. When the values of the two moments are in fact plotted as a function of the stirring speed, it is found that all the values obtained from experiments where the stirring speed was changed continuously (Fig. 4.12) or stepwise (Fig. 4.11) fall on a single curve. This is illustrated in Fig. 4.13a, b where the corresponding moments of the CMD, $\langle R_g \rangle$ and $I(0)/I(0)_{t=0}$, are plotted as a function of the volume average shear rate in the vessel, which is related to the stirring speed as reported in These results further confirm that the used rate of change of the stirring speed is slow enough so that the CMD readjusts faster to the new steady state than the stirring speed variation.

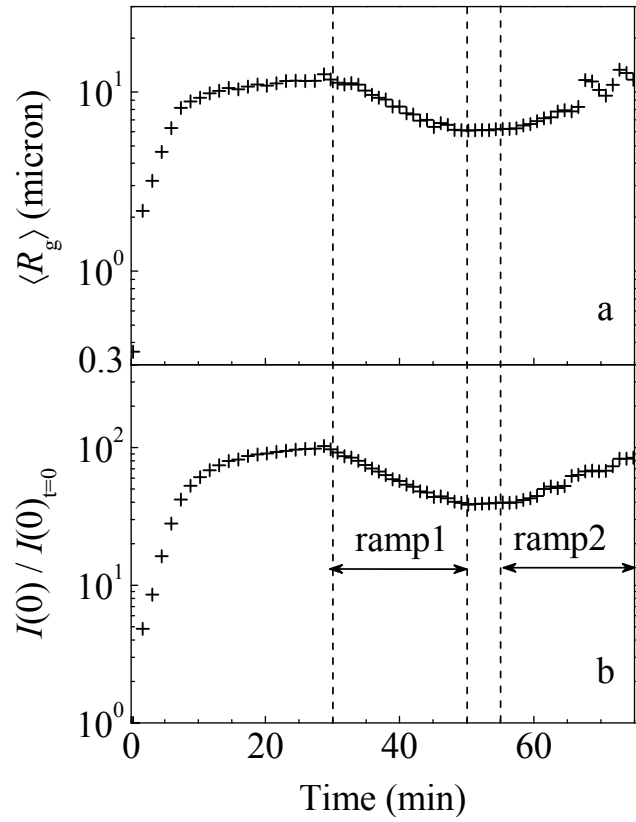


Figure 4.12: Time evolution of the radius of gyration $\langle R_g \rangle$ (a) and normalized zero angle intensity $I(0)$ (b) during ramp changes of the stirring speed $400 \rightarrow 1073 \rightarrow 400$ rpm with a change equal to 30 rpm/min, measured for a solid volume fraction equal to 4×10^{-5}

4.6. Scaling of moment of the steady state CMD with shear rate

The values of $\langle R_g \rangle$ and $I(0)/I(0)_{t=0}$ shown in Fig. 4.13 obtained from experiments with continuous variation (\oplus) and stepwise changes (\circ) of the stirring speed at a solid volume fraction equal to 4×10^{-5} allow us to estimate the scaling of these moments with respect to the shear rate. In order to account for the effect of the solid volume fraction the corresponding data of infinite dilution (as $\phi \rightarrow 0$) from Fig. 4.10 have also been reported in the same figure (\blacktriangle). It is seen that both experiments follow the same scaling given by $\langle R_g \rangle \propto \langle G \rangle^{-0.5}$. This is in agreement with the scaling of the maximum stable aggregate size with shear rate developed by Potanin⁹⁰. He assumed that an aggregate is composed of parts (fragments) connected by chains of particles. These chains form the aggregate skeleton and in order to break such an aggregate, it is necessary to break its skeleton. For the system investigated in this work, it can be assumed that the tangential forces are negligible and particles predominantly interact via central forces and, therefore, the internal structure deforms irreversibly even under the action of infinitesimally small forces. As only the straight chains of particles are able to resist the stretching of the aggregate the resistance of such an aggregate to external forces is reduced to the resistance of a single straight chain and, therefore to the van der Waals attraction force between two primary particles.

In addition to $\langle R_g \rangle$ also another moment of the CMD, the normalized zero-angle light scattering intensity, shows a certain proportionality to the volume average shear rate according to $I(0)/I(0)_{t=0} \propto \langle G \rangle^{-0.7}$ for both ϕ equal to 4×10^{-5} and $\phi \rightarrow 0$. Such a scaling of both moments of CMD indicates a negligible effect of the solid volume fraction on the steady-state shape of the CMD, at least under the conditions examined in this work.

When comparing the measured scaling of $\langle R_g \rangle$ as a function of the shear rate with literature data obtained under various operating conditions using different vessel geometries, different size and composition of primary particles^{26, 40, 44, 50, 51, 75, 76, 83, 89, 91}, we found good agreement. In the case of the zero-angle intensity the measured scaling obtained from our data can be compared only with two sets of data published by Sonntag and Russel^{64, 65} for aggregates produced under static conditions using primary particles with a diameter of 140 nm, which were subsequently broken in laminar Couette and converging flow, and by Selomulya et al.⁵¹, using a

Taylor-Couette apparatus under turbulent conditions and same size of primary particles as in this work. In the case of Sonntag and Russel's data ^{64, 65}, the obtained slopes (equal to -0.88 and -1.0, respectively), are slightly larger than the value measured in this work. On the other hand, Selomulya's data ⁵¹, indicate a scaling similar to the one obtained in this work with slope equal to -0.65. This variation in the slope of the $I(0)/I(0)_{t=0}$ vs. $\langle G \rangle$ is most probably caused by the different types of flow applied by various authors, where in the case of laminar flow larger values are observed compared to those for turbulent flow conditions.

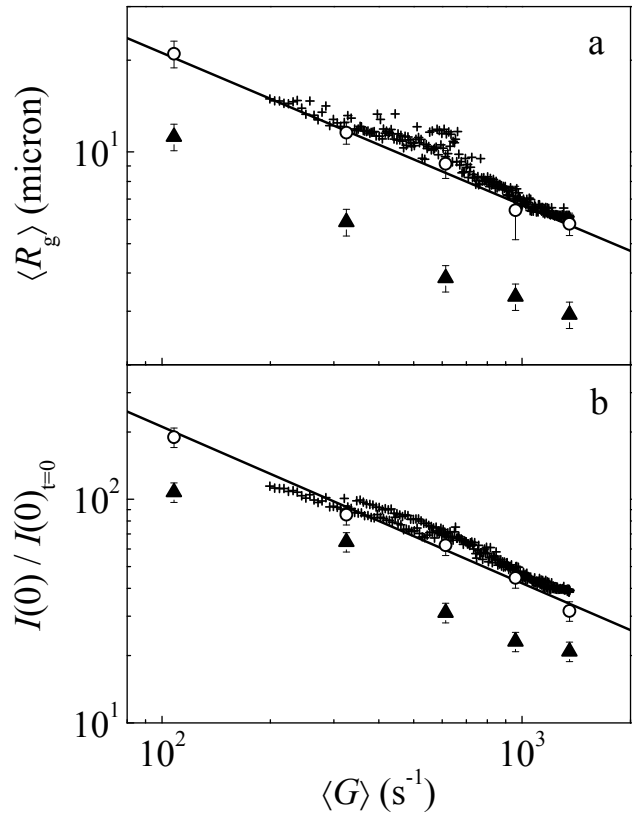


Figure 4.13: Moments of the CMD: ($\langle R_g \rangle$) (a) and normalized $I(0)$ (b)) at steady state as a function of the volume average shear rate for a constant stirring speed (\circ), for ramp changes of the stirring speed ($+$) at $\phi = 4 \times 10^{-5}$ and at infinite dilution (\blacktriangle) data from Fig. 4.10.

4.7. Conclusions and summary

In this chapter we investigated the aggregation and breakage of fully destabilized polystyrene particles with a diameter of 810 nm under turbulent conditions. A broad range of solid volume fraction from 1×10^{-6} to 4×10^{-5} as well as volume average shear rates ranging from 108 to 1350 s^{-1} were covered. On-line small-angle static light scattering was used to characterize the time evolution of the cluster mass distribution (CMD) in terms of its two independent moments, namely the root-mean-square (rms) radius of gyration and the average zero-angle intensity. In addition, the structure of the aggregates was monitored in terms of the time evolution of the scaling exponent. Since the size of primary particles is outside the Rayleigh-Debye-Gans limit, independent information about the aggregate structure was determined by image analysis of 2D images of aggregates over the whole range of stirring speed investigated in this work. It was found that, due to the large size of the primary particles, the value of the scaling exponent obtained from light scattering measurement significantly underestimates the fractal dimension of the aggregates. Based on the image analysis it was found that the aggregate structure as well as the aggregate shape does not change with respect to the applied stirring speed, with a fractal dimension equal to 2.62 ± 0.18 , and the aspect ratio of the aggregates in the range from 1 to 2.6 with most the aggregate having aspect ratio around 1.4.

It was found that the initial time evolution of both moments of the CMD is controlled only by one mechanism (shear aggregation). To obtain the same initial kinetics it is necessary to use a collision efficiency weakly dependent on the shear rate. According to this a modified dimensionless time defined as $\tau_M = \alpha(N_F)t\langle G \rangle \phi$, where $\alpha(N_F)$ is the collision efficiency equal to $C(A_H/\mu G R_p^3)^{-b}$, with an exponent, b , equal to 0.18 has to be used. Later in time, a second mechanism (breakage) starts to be active, thus the similarity above is lost and the process approaches a steady state, where both the dynamics as well as its final value strongly depend on the applied stirring speed. Once steady state was reached, the response of the system on stepwise and continuous (ramp) changes in stirring speed was investigated. It was found that the process is fully reversible and the steady-state values of both moments of the CMD do not depend on the shear rate history. In addition, to obtain the critical aggregates size below which breakage is negligible, another type of dynamic experiment – continuous dilution with particle-free solution – was performed. It was found that the values of the rms radius of gyration obtained at steady

state as well as at infinite-dilution conditions are proportional to the volume average shear rate according to $\langle R_g \rangle \propto \langle G \rangle^{-0.5}$ and the normalized zero-angle intensities are proportional to the volume average shear rate according to $I(0)/I(0)_{t=0} \propto \langle G \rangle^{-0.7}$. This indicates that the CMDs at steady state as well as at the end of dilution are very similar in shape. Relating the values of the aggregates size under infinite dilution to the maximum values of the shear rate in the vessel leads to a size-independent aggregate cohesive force equal to 6.2 ± 1.0 nN.

Finally, we can conclude that the presented technique provides a tool to measure in detail various parameters of systems undergoing aggregation and breakage and in this way to compare the performance of the process for different operating conditions.

5. Surface chemistry effects

5.1. Introduction and motivation

So far, Most of these studies focused on physical parameters such as the shear rate, solid volume fraction, primary particle size and equipment geometry^{17, 19-21, 26, 28, 47, 50, 51, 92, 93}. However, surface chemistry is known to play a paramount role in interactions among colloidal particles because it determines the nanoscale composition of the interparticle region, which in turn determines the force and the contact distance between the primary particles in the aggregate⁹⁴⁻⁹⁷. Therefore, chemical aspects are expected to influence greatly flow-induced aggregation and breakage. Nonetheless, research work on surface chemistry effects in flow-induced aggregation focused mainly on minerals^{98, 99}, especially the role of surfactant during flocculation. Effects of surface chemistry on flow-induced aggregation of polymer colloids remain largely unexplored, with few exceptions^{100, 101}. Furthermore, several papers addressing flow-induced aggregation do not report data such as composition and surface density of charge group^{19, 26, 38, 47, 50, 51}. This impedes the assessment of the role of surface chemistry in the reported experimental data. Overlooking this role might confound the results of studies investigating a specific parameter, e.g., primary particle size, using latexes that are not identical in their surface chemistry⁵¹.

This deficiency in the literature is due to the extrapolation to flow-induced aggregation of the view that for metastable colloidal suspensions in aqueous media with ionic strength above the critical coagulation concentration (CCC) no energy barrier exists, and van der Waals forces are bringing about rapid aggregation down to a distance of few angstroms imposed by Born repulsion, thus, the outcome of aggregation above the CCC should be universal at least for the same bulk material⁹³. However, this view is based on observations of aggregation in quiescent condition and is valid for systems where DLVO theory can represent the interparticle interactions. The validity of this extrapolation to aggregation in flow was never put to test. Furthermore, the structure of the double layer, i.e., depth and coverage of the counter-ions, co-ions and hydration water molecules adjacent to the surface, can still influence the interparticle forces within the aggregate above the CCC through various mechanisms such as: hydration repulsion¹⁰²⁻¹⁰⁵, hydrophobic attraction⁹⁴, steric hindrance, and ion bridging¹⁰⁶, which might influence flow-induced breakage of aggregates, a phenomena that is absent in quiescent systems.

The objective of the work presented in this chapter is to elucidate the possible effects that these mechanisms might have on aggregation and breakage of polystyrene particles in turbulent flow. As a starting point we decided to study the influence of two surface attributes: the degree of ionization of surface groups and the area per charge groups. The first attribute was studied by carrying out aggregation experiments of surfactant-free carboxyl latex at various pH values in salt concentration well above the CCC; in a fixed flow field and solid volume fraction. The second attribute was studied by repeating the experiments at various pH values for another surfactant-free carboxyl-modified latex with a smaller area per charge group albeit with smaller primary particle diameter. A sulphate latex with particle size similar to the carboxyl latex but with much larger area per charge group was also investigated. The bulk material of the three latexes is polystyrene. Other surface attributes, such as the amount and the spatial organization of polymer chains and surfactant molecules adsorbed on the surface, can play a fundamental rule in aggregation of particles and fragmentation of aggregates. Such attributes are decisive for unit operations such as selective flocculation that is usually carried out in flow conditions¹⁰⁷. However, these attributes are absent in the “model” systems investigated in this study, which allows us to focus on the effects of the surface area per charge group and the degree of ionization of surface charge groups.

5.2. Materials

Specifications of the latexes used were the following. The main latex used was a carboxyl polystyrene white latex purchased from Interfacial Dynamics Corporation (IDC), Portland, OR (USA) (Product-No: 7-300, CV: 3.2%, Batch-No: 2440, solid% = 4.3). The diameter of primary particles was found to be 300 nm with a narrow distribution. The area per carboxyl group on the surface was 162 Å². The second latex was surfactant-free sulphate white latex (Product-No: 1-300, CV:5.6%, Batch-No: 1919, solid% = 8.8) with a low surface density of charge group (1073 Å²/ sulfate group) and a narrowly distributed primary particle diameter around 320 nm. The third latex used was surfactant-free carboxyl modified polystyrene white latex (Product-No: 2-100, CV: 5.8%, Batch-No: 1909-1, solid% = 4). This latex was electrosterically stabilized by copolymerization with carboxylic acid, and therefore is reported by the vendor to have a fluffy surface layer and to be relatively hydrophilic. The diameter of primary particles was found to be

107 nm with a narrow distribution. The area per carboxyl group on the surface was almost half of that in the carboxyl latex, 82 \AA^2 .

Batch experiments were carried out employing the same equipment, experimental procedure and light scattering measurement technique as described in the previous chapters. The experiments proceeded as follows. First, the original surfactant-free charge-stabilized latex was diluted using deionized water to the desired concentration, and fed to the stirred tank. Then, the diluted dispersion of stable particles is stirred at high speed to double check their stability and destroy any loose aggregates that might exist. After few minutes the desired rotation speed is set. Aggregation begins with the injection of 60 ml of 4.9 molar aqueous MgCl_2 solution into the tank, along with the necessary amount of HCl or NaOH to obtain the desired pH. The resulting salt concentration in the tank is about five times the CCC. On-line light scattering measurements is started once the salt, and the acid or base, solution is injected.

As in the work described in the previous chapters, the dependency of the scattered light intensity $I(q)$ on the amplitude of scattering vector q is later analyzed to obtain two moments of the cluster mass distribution (CMD), $\langle R_g \rangle$ and $I(0)$ as well as the scaling exponent (SE) of the power law region in the structure factor $S(q)$, which approximates the fractal dimension d_f . However, for the structure factor to give us reliable values of the d_f , the size of the primary particles must be in the limit of the Rayleigh-Debye-Gans (RDG) theory, i.e., each primary particle in the aggregate scatters light independently from all the others. The validity of this assumption depends on the wave length of the light used, the primary particle size, the relative refractive index of the particle material and the suspending medium as expressed in the following inequalities

$$|m-1| \leq 1 \quad \text{and} \quad (4\pi R_p / \lambda) |m-1| \leq 1 \quad (5.1)$$

where m is the relative refractive index, $m=1.195$ for polystyrene in water, R_p is the radius of the primary particle, and λ is the laser wave length. These conditions are satisfied for the latexes used in the current work. However, detailed studies of d_f using both image analysis and light scattering showed that the SE is not always equal to the d_f obtained by analysis of images acquired by confocal laser microscope, see section 4.3. The agreement between both techniques is satisfactory only for primary particles with diameters less than 120 nm^{17} . Therefore only for

the latex of 100nm particle do we rely on light scattering to obtain information about the structure. For the 300 nm latex we use microscopy and image analysis.

5.3. Dependency of the CMD on the pH

Let us examine first the series of experiments at various pH values carried out using the carboxyl latex with primary particle diameter of 300nm, Fig. 5.1. The solid volume fraction (ϕ) was the same for all experiments at 20 ppm. All the experiments were done at a rotation speed of 200 rpm in the same stirred tank. The data shows a consistent trend in the sizes attained during experiments; the lower the pH the larger the size. This trend exhibits a significant jump between pH 6 (solid triangles) and pH 5 (open triangles) and saturation below pH 5 as the sizes attained at pH 3 (squares) and pH 4 (circles) and pH5 are practically the same. Another noticeable feature of Fig. 5.1 is the change in the shape of the time evolution of aggregate sizes. For pH larger than 6 the shape is sigmoidal similar to that observed in our earlier, chapters 3 and 4, At pH 6 a hump appears that becomes a clear peak in the size attained during experiments at lower pH. Closer examination of this feature, the overshoot in sizes, is presented later in this paper. Fig. 5.2 summarizes the dependency of the steady state size and the overshoot on the pH.

An important feature of the experiments illustrated in Fig. 5.1 is that initial aggregation kinetics, the first 5-7 minutes, where only pure aggregation is taking place²⁸ shows no clear dependency on pH, unlike the subsequent intervals of the time evolution of sizes. This independency of aggregation from the pH was checked in the static aggregation experiments shown in Fig. 5.3. This figure illustrates time evolution of $\langle R_g \rangle$ and $I(0)$ in quiescent conditions at salt concentration equal to the one used in the stirred tank for two experiments; one at pH 5 and the other at pH 8 (hexagons). The curves are almost identical, taking experimental error into account, which is in agreement with the prevailing understanding of static aggregation since the salt concentration was well above the CCC.

The absence of pH effect on pure aggregation, either in flow or in quiescent water, suggests that the observed dependency of sizes on the pH is due to the effects of pH on the breakage of aggregates. This can be understood in light of the fact that aggregation in absence of energy barrier is mainly due to the long range van der Waals forces. On the other hand, breakage is influenced also by forces of short range that hardly influences aggregation rate, yet they are crucial in determining the cohesive forces between particles upon contact.

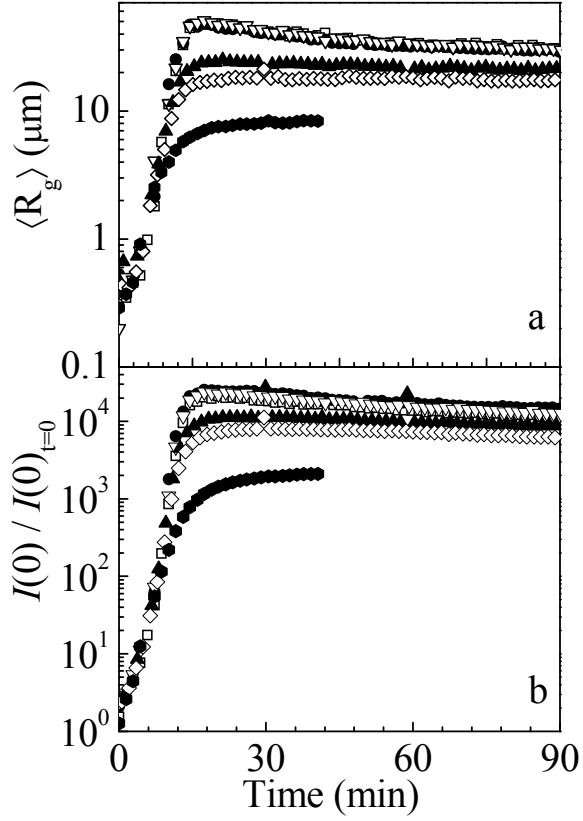


Figure 5.1: Time evolution of average radius of gyration $\langle R_g \rangle$ (a) and normalized zero angle intensity $I(0)$ (b) during aggregation of 300 nm carboxyl latex in batch experiments using a solid volume fraction of 20 ppm, and a stirring speed of 200 rpm, at various pH values; (●) pH 8, (◇) pH 7, (▲) pH 6, (▽) pH 5, (●) pH 4 and (□) pH 3

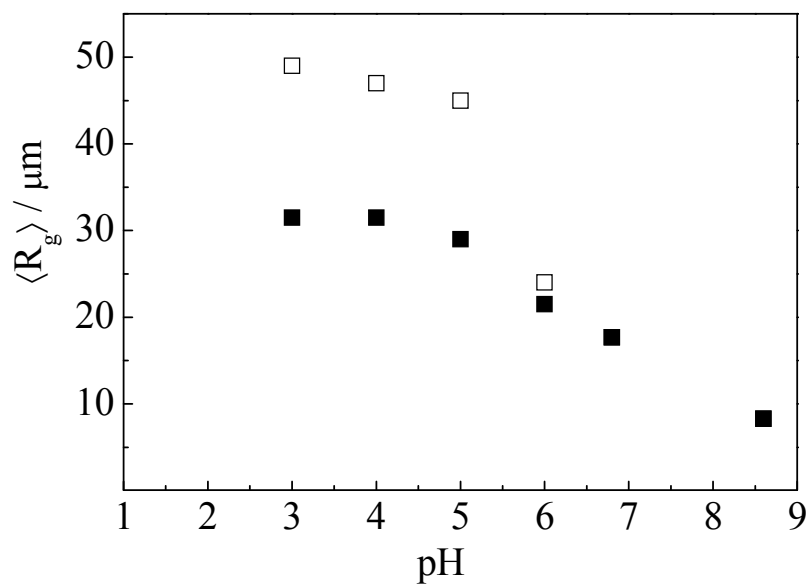


Figure 5.2: Steady state and peak values of average radius of gyration $\langle R_g \rangle$ at various pH; (■) steady state (□) peak.

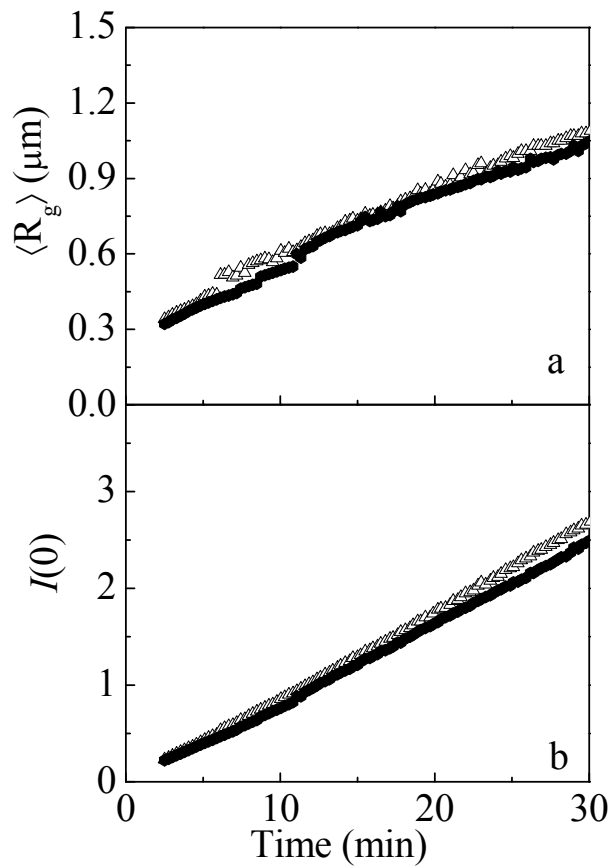


Figure 5.3: Time evolution of average radius of gyration $\langle R_g \rangle$ (a) and normalized zero angle intensity $I(0)$ (b) during static aggregation of 300 nm carboxyl latex at the same salt concentration of 100 mM, using a solid volume fraction of 20 ppm, at two pH values; (●) pH 8, (▽) pH 5

To explain the aforementioned results we envisage the surface of the particle as illustrated schematically in Fig. 5.5 In this figure a surface group is depicted as tiny protrusion from the surface. When it is protonated, situation A, no ions hold to it upon addition of the salt and fewer hydration water molecules surround it. While when this group is deprotonated, situation B, it attracts counter ions, co-ions, and more hydration water. With the increase in pH more surface groups become protonated, which can decrease the interparticle force upon contact through three mechanisms.

First, the hydrophilic repulsion increases with pH increase. This repulsion is due to the hydrogen bonds between the surface ionic groups and the dipolar water molecules, which arrange the interfacial water. Thus a repulsive force of entropic origin appears when two particles verge upon each other due to the overlap of the relatively more organized layers of high density interfacial water and the need to disrupt them and dehydrate the surface. This force extends up to a distance of few molecular diameters away from the surface. The term hydration pressure is sometimes used to refer to this force¹⁰⁸⁻¹¹¹. Evidences for the existence of repulsive hydration forces between polystyrene latex particles with ionic surface groups, similar to the latex used in the study, exist in the literature^{96, 112, 113}. Moreover, with the addition of salt, ion pairs form between surface groups and counter ions; such dipoles have a considerable ability to orient and structure water molecules around them¹⁰⁴. Therefore, hydration repulsion increases with the density of sites capable of ion pairing on the surface. Hiemstra and van Riemsdijk¹¹⁴ emphasize also the role of dipole formation, in their case between surface oxygen atoms and hydrogen atoms in the water molecules, in orientating interfacial water and enhancing the hydration repulsive forces. Kataoka et al¹¹⁵, used vibrational sum-frequency spectroscopy (VSFS) to elucidate the water structure at TiO₂ water interface as a function of pH. They report that the degree of organization, i.e., extent of the highly aligned interfacial water, increases monotonically as the pH increases. The reason given is that the de-protonation of more surface groups increases the electric field at the surface. In short, an additional repulsive force is expected to manifest itself during the breakage of aggregates of carboxyl latex particles. This force persists at salt concentration above the CCC, where the electrostatic repulsion is completely screened, and since it is of short range it does not influence aggregation significantly. For the same latex, this force becomes stronger at higher pH as more ionic groups are deprotonized; thus making the surface potential higher and allowing for the formation of more ion

pairs with the counterions. This force can make the breakage of aggregates easier and thus the sizes attained at high pH are smaller than those attained at low pH.

Second, the hydrophobic attraction decrease with pH increase. The apolarity of polystyrene is expected to give rise to short-range hydrophobic attraction of entropic origin¹⁰⁸. This hydrophobic attraction increases with increasing hydrophobicity and hydrophobic area¹¹⁰. Therefore, higher pH, for the same surface density of charge groups, will attenuate this attractive force. Because the higher pH leads to more ionized groups, which means more sites with enhanced hydrogen bonding ability, i.e., more hydrophilicity^{104, 115}. Moreover, the discrete nature of the surface charge group means a larger portion of the hydrophobic surface is shielded when more hydration water molecules surround the surface group.

Third, the steric limit on the minimum contact distance increases with pH increase. The unfeasibility of the overlap of surface charge groups gives a steric limit to the contact distance between two aggregated particles equal to twice the size of the surface protrusion. The overall Interaction potential may not necessarily be at its minimum at this distance. This limit increases with the increase the pH. The reasons for this is again the de-ionization of the surface groups and their consequent binding with counter ions, which increases the size of the surface protrusions represented by the surface groups and the counterions adhered to them, hence the steric limit to the interparticle distance upon aggregation.

This notion suggests that aggregates will be still responsive to the pH even after growth because the surface groups remains responsive to the solution composition. This was tested in experiments where the pH was changed after the CMD approached steady state. The data are shown in Fig. 5.5 for the same ϕ of 20 ppm and rotation speed of 200rpm. The triangles refer to an experiment where aggregation started at pH 5 then the pH was increased to 8. Once the base was added the sizes started to decrease as the figure illustrates. The sizes attained were close to, but still larger than, those attained in experiments starting from pH 8. The hexagons refer to experiments that were started at pH 8 then the pH was decreased to 5. The sizes exhibited remarkable growth to values almost identical to those attained in experiments at pH5, after the peak gradual decay also ensued to similar sizes.

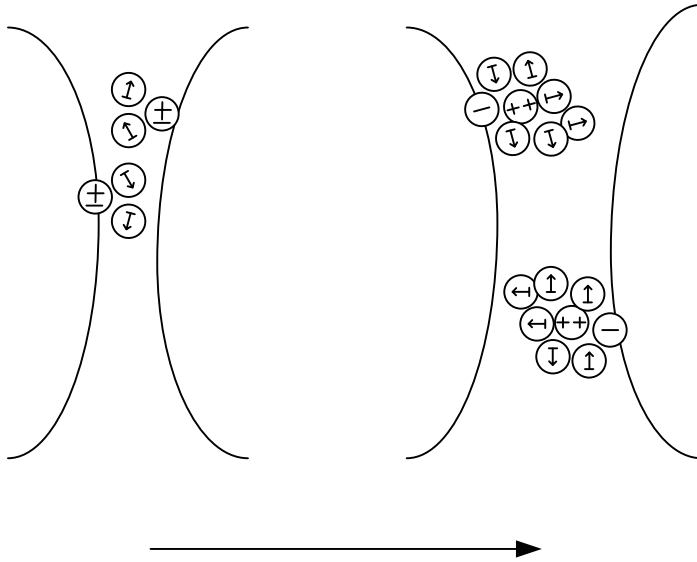


Figure 5.4: Sketch of the difference between an ionized surface group (a) and a deionized one (b) to illustrate the reason for strengthening the hydrophilic repulsion

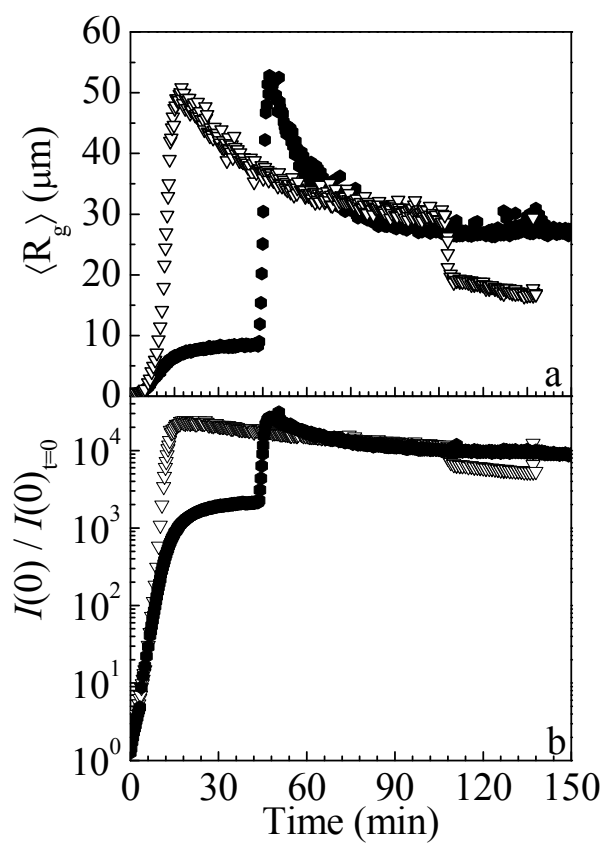


Figure 5.5: Response of average radius of gyration $\langle R_g \rangle$ (a) and normalized zero angle intensity $I(0)$ (b) to step changes in pH during aggregation of 300 nm carboxyl latex in batch experiments using a solid volume fraction of 20 ppm, and a stirring speed of 200 rpm; (●) pH 8 \square pH5, (▽) pH 5, (□) pH8

Moreover, this notion suggests that large area per group should have an effect similar to low pH; because, it means fewer centers of hydrophilic repulsion, less shielding of the hydrophobic surface and a less stringent steric limit on the distance upon contact. To verify this suggestion we examined the aggregation of sulphate latex with an area per charge group of 1073 \AA^2 at pH6. The results are shown in Fig. 5.6 (solid squares) along with experiments using the carboxyl latex (162 \AA^2 / carboxyl group) at the same pH (solid triangles). The differences in sizes are clear, although the particle size, ϕ , the rotation speed and the pH are the same for both experiments. As expected, the latex with large area per group exhibited much larger moments of the CMD. Plotting the experiment of the carboxyl latex at low pH of 3 in the same figure reveals an interesting feature. The differences between the latex of large area per group and that with small area per group are perfectly concealed with the decrease of pH for the carboxyl latex, since the carboxyl groups become protonated. These results are in agreement with our explanations of the dependency of sizes on the pH, and support the notion discussed previously.

To check the generality of the observations and the explanations put forward so far, we carried out experiments using another carboxyl latex at various pH values. This second latex is electrosterically stabilized and has a smaller particle size and area per charge group as detailed earlier. The results, shown in Fig. 5.7, are qualitatively similar to those obtained using carboxyl latex used in Figs. 5.1-4. The sizes obtained in experiments carried out at low pH are larger than those obtained in experiments at high pH, with an overshoot appearing for experiments below a certain pH. However, the sizes obtained are smaller than those obtained using the carboxyl latex for all pH values. This can be attributed to the smaller area per group in the carboxyl modified latex, and hence the more hydrophilicity, i.e., less hydrophobicity, of the surface. The notion of ionizable surface groups as a center of repulsive force, as an impediment of attractive force, and as a steric limit seems to hold here as well. It can explain the smaller sizes at the same conditions for latex with more groups per unit area as well as it could explain the increase in the size with the deionization of surface groups.

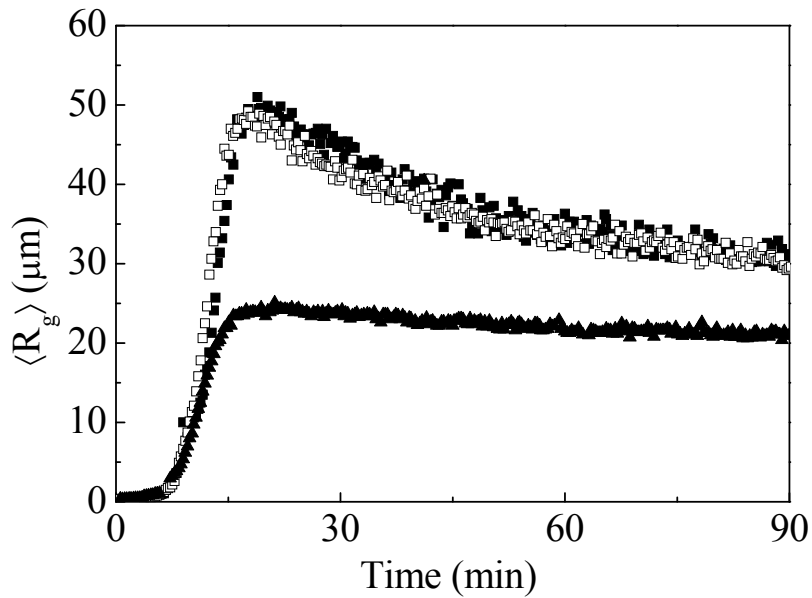


Figure 5.6: Comparison between the time evolution of average radius of gyration $\langle R_g \rangle$ during aggregation of 300 nm carboxyl latex and that during aggregation of 320 sulphate latex in batch experiments using a solid volume fraction of 20 ppm, and a stirring speed of 200 rpm. (\blacktriangle) 300nm carboxyl at pH 6, (\blacksquare) 320nm sulphate at pH 6, and (\square) 300nm carboxyl at pH 3

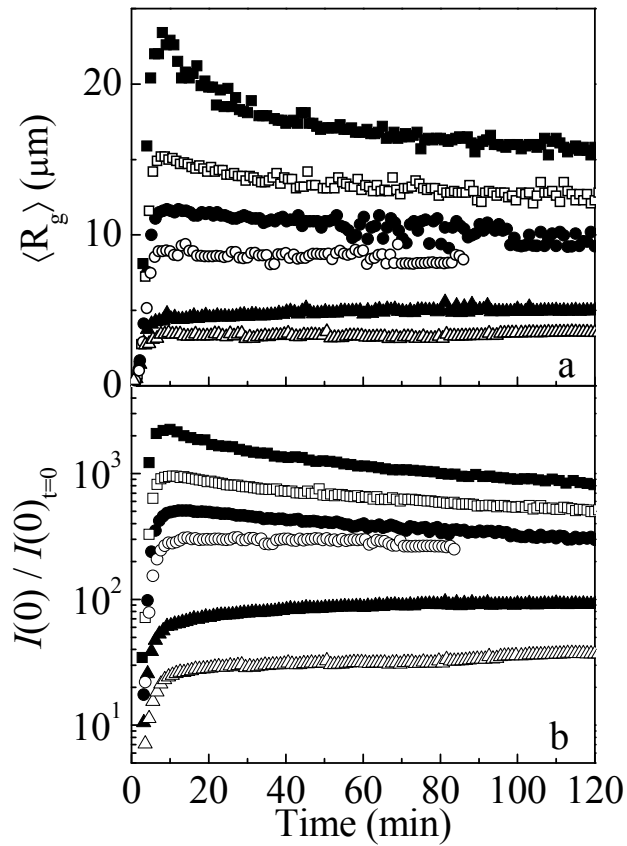


Figure 5.7: Time evolution of average radius of gyration $\langle R_g \rangle$ (a) and normalized zero angle intensity $I(0)$ (b) during aggregation of 100 nm carboxyl modified latex in batch experiments using a solid volume fraction of 20 ppm, and a stirring speed of 200 rpm, at various pH values; (8) pH 7, (▲) pH 6, (○) pH 5, (●) pH 4.6, (■) pH 4 and (□) pH 2

5.4. Phenomena leading to the overshoot

Now we focus on the qualitative change in the time evolution of aggregates sizes. As we have seen, in some experiments the time evolution follows a sigmoidal behavior that is perfectly understood and can be directly modeled. While in other experiment the aggregates grow to maximum sizes in relatively short time. Then slow decay ensues after this maximum is reached. For some experiments this decay leads to a steady state within the time span of the experiments, while for others the decay was so slow such that convergence to a steady state was not observed in the time span of few hours. Earlier works which encountered this behavior attributed it to restructuring, defined as reorganization of primary particles within the aggregate under hydrodynamic stresses. They suggest that particles aggregate to form open structures initially, thus they reach large sizes. These large open aggregates are later compacted gradually by sliding and rolling of some parts. This hypothesis can be tested by examining the aggregate structure at two time instances with similar CMD one before the overshoot and one after it; to check whether the structures of the aggregates is more compact after the hypothesized compaction that causes the decay from the overshoot.

For the aggregates of the smaller particles, $D_p = 100\text{nm}$, multi-angle static light scattering gives a faithful representation of the aggregate structure through the structure factor $S(q)$ as discussed earlier. For these aggregate one can get d_f from the slope of the power law region of the structure factor $S(q)$ vs q . in Fig. 5.8 are shown the structure factors at three time instance during an experiment where a clear overshoot is exhibited. These time instance are $t = 4$ min, $t = 90$ min and $t = 10$ min which correspond to the overshoot in size. $\langle R_g \rangle$ and $I(0)$ have similar values for $t = 4$ min and $t = 90$ min; therefore the CMDs at these two time instances can be assumed to be the same. The structure factors at these two time instances demonstrate no appreciable different in aggregate structure and give close values of d_f , which was 2.47 after 4 minutes and increase by less than 0.1 to 2.56 after 90 minutes. Moreover, d_f at the overshoot has a similar value, 2.54. The same examination was done for the aggregates of large primary particles with the difference that we obtained the fractal dimension from image analysis instead of the structure factor of light scattering. In Fig. 5.9 is shown the relation between the area and the perimeter of the aggregates obtained from three samples taken at three time instance during aggregation of the 300nm carboxyl latex at pH 5. The circles refer to 10 min the triangles to 30 min and the squares to 90 min. as we can see the images from the three samples have the same

scaling as indicated by the solid line. This means that the perimeter fractal dimension hardly changes during the peaking in size and the subsequent decay, in agreement with the results of light scattering. Based on these two examinations we conclude that restructuring alone can not interpret the overshoot behavior because the observed changes in the structure are too small to account for the changes in aggregate sizes.

Another hypothesis is that the overshoot is a manifestation of flow field heterogeneity. The reasoning here goes as follows: the aggregation in the relatively calm regions far from the impeller leads to large clusters initially when most of the population is primary particles. These large clusters cause an increase in the average sizes of the whole population. However, the circulation of the tank content through the impeller region leads to breakage of these large aggregates. The changes in the CMD means that repeating the growth to the same sizes is not possible and therefore the circulation in the tank cause decay and not oscillation in the average aggregate size. This hypothesis is seriously challenged by the data sets given in Figs. 5.1 and 5.7, where at the same rotation speed in the same tank we see an overshoot depending only on the pH i.e., the interparticle forces. Moreover, the timescale of macromixing in the coagulator used is two orders of magnitude smaller than the timescale of breakage²⁸. This mixing is fast enough for flow field heterogeneity to have an effect on breakage kinetics⁵⁴. These two arguments refute this hypothesis

Nevertheless, we proceeded to study the effect of the stirring speed on systems with an overshoot using the same latex at the same solid volume fraction and pH. The results of the experiments at various stirring speed are shown in Fig. 5.10, with a modified dimensionless time τ_M calculated as in the previous chapter. τ_M was calculated in a way that makes initial aggregation kinetics collapse on one curve. The power of the shear rate was 0.65. The same power dependency is obtained when the time is normalized with the mixing time. This figure also illustrates that the increase in shear rate suppresses the overshoot in agreement with the data of Rahmani et al⁷⁰ and selumolya et al⁵¹.

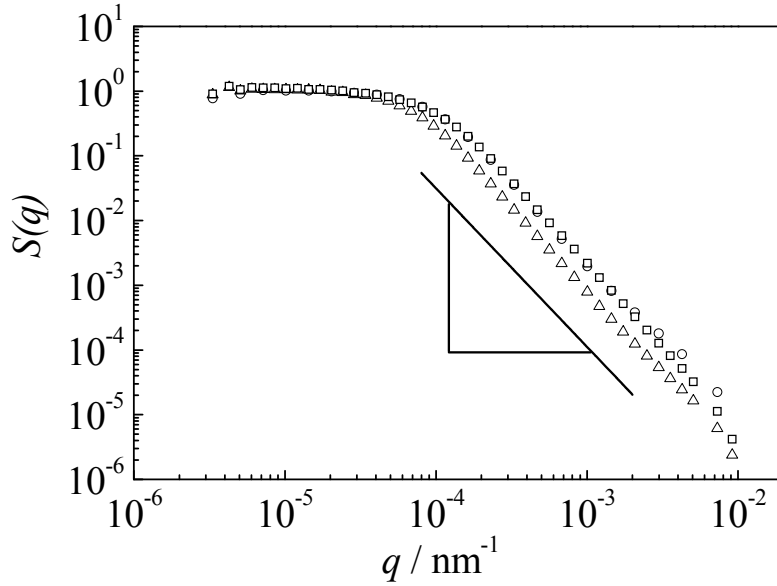


Figure 5.8: Structure factor of the CMD at three time instance during aggregation of 100 nm carboxyl modified latex in batch experiments using a solid volume fraction of 20 ppm, a stirring speed of 200 rpm, and pH 2; (○) 4 min, (△) 10 min, the overshoot, (□) 90 min. structure factors at 4 and 90 minutes were selected on purpose since the CMDs at these two time instance have very close $\langle R_g \rangle$ and $I(0)$.

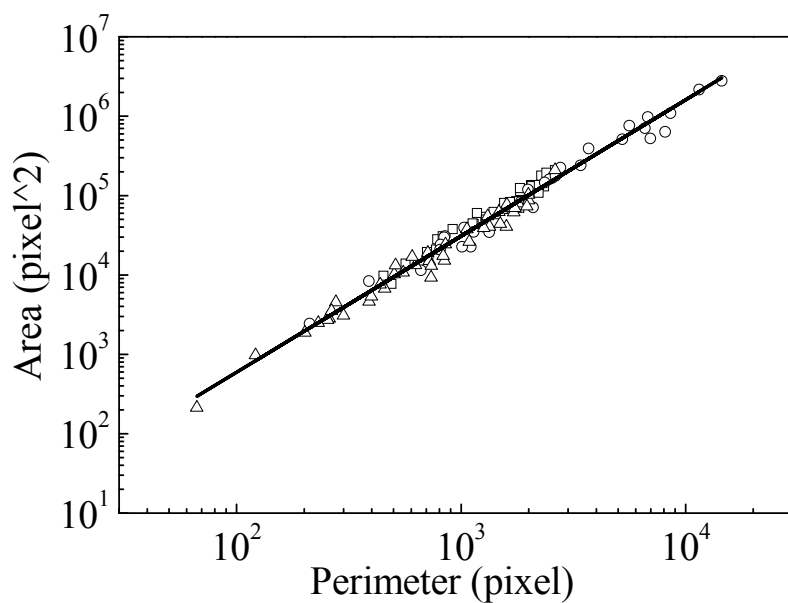


Figure 5.9: Area vs., perimeter of images of aggregates obtained at three time instance during aggregation of 300 nm carboxyl latex in batch experiments using a solid volume fraction of 20 ppm, a stirring speed of 200 rpm, and pH 5. (Δ) 10 min, (\circ) 30 min, the overshoot, (\square) 90 min. the solid line is fitting of a power law relation to obtain the perimeter fractal dimension d_{pf}

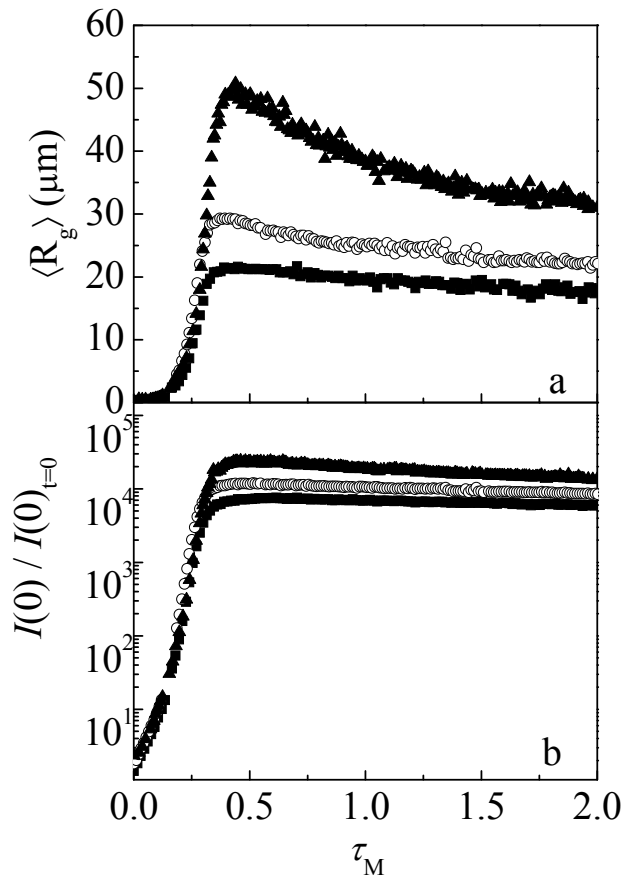


Figure 5.10: Average radius of gyration $\langle R_g \rangle$ (a) and normalized zero angle intensity $I(0)$ (b) as a function of modified dimensionless time $\tau_M = \phi t G^{-b}$ with $b=0.65$, during aggregation of 300 nm carboxyl latex in batch experiments using a solid volume fraction of 20 ppm, and pH 5, at various stirring speeds; (\blacktriangle) 200 rpm, (\circ) 300 rpm, and (\blacksquare) 400 rpm.

Against the failure of these two hypotheses we had to propose an original one and test it. Our hypothesis is based on the observation that appearance of the overshoot happens at the same conditions that lead to larger aggregate sizes, i.e., larger area per charge group or low pH. In other words the overshoot appears when the interparticle forces are high. Moreover, such a decay in the aggregate sizes can be accounted for by a gradual loss of the aggregates cohesive force. Based on these two observations we postulated that the high interparticle force and the short contact distance, due to low pH or larger area per group, lead to ductile separation upon breakage under hydrodynamic stresses. This ductile separation increases surface roughness which decreases interparticle force upon re-aggregation. Evidence of these two phenomena, ductile separation and decrease of interparticle forces with surface roughness, abound in the literature. See for example the reviews by Walz¹¹⁶ and Johnson¹¹⁷ and the experimental work of Schaefer et al¹¹⁸.

Schmitt et al¹¹⁹ report experimental measurements in which the attractive forces between polystyrene surfaces decrease with the number of contact-detachment events. Similar behavior was found by Du et al¹²⁰ for gold. Both groups attribute this decrease in attractive force to the ductile separation and consequent increase in surface roughness. Increase in the length of surface asperities and/or increase in the variance of the asperity length distribution can cause significant decrease in the attraction between surfaces by imposing a larger steric limit on the minimum distance upon contact¹¹⁷. Moreover, increase in surface roughness decreases the effective contact area of the surfaces which also reduces the cohesion forces¹¹⁹.

Du et al¹²⁰ propose a dimensionless parameter S to characterize whether the separation between two surfaces is brittle or ductile. This parameter reads

$$S = \frac{\Delta\gamma}{Z_o H} \quad (5.2)$$

where $\Delta\gamma$ is the adhesion energy, Z_o is the distance and H is the hardness. the hardness, H , and the elasticity, defined as Young's modulus E , are proportional quantities¹²¹. Du et al state that the transition from brittle to ductile separation happens when this parameter exceeds 1. This means that higher interparticle forces and or shorter interparticle distance can cause the transition from brittle to ductile separation.

Reitsma et al¹²² applied the analysis of Mauguis and Pollock derived for the contact between a deformable sphere and a rigid surface¹²³ to find out the load at the onset of elasto-

plastic deformation, P_e , and the load leading to full plastic deformation, P_p , for polystyrene particles of radius 115 nm pressed against silicon wafer. They report $P_e \approx 190$ pN and $P_p \approx 81$ nN using the mechanical properties of polystyrene. To check whether plastic deformation influences the particles in our systems after attainment of the overshoot, we can compare P_e and P_p with the forces that the hydrodynamic stresses apply on aggregates, F_h , as calculated in section 4.4.1, Eq 4.3, 4.4. From the analysis discussed in that section we get values of $F_h \approx 120$ nN for $d = 2 \langle R_g \rangle$ and ε corresponding to the maximum values encountered in the tank in the region close to the impeller see Fig. 2.13, where most of the breakage takes place. Such a value suggests that separation is ductile, therefore leads to deterioration of the surface.

A possible test to this hypothesis is to examine the regrowth capacity of the particles after a certain number of aggregation and breakage events. In the work presented in chapter 4, where only sigmoidal time evolution curves were observed, we found remarkable ability of the aggregates to regrow upon the reduction of the shear rate. Furthermore, it was demonstrated that the aggregation and breakage are reversible with respect to shear rate changes and that aggregate sizes are independent of shear rate history, see Fig. 4.11 and Fig. 4.12. This reversibility indicates that interparticle forces do not change with aggregation and breakage events. However, this will not be the case if surface deterioration takes place due to ductile separation. Therefore, we proceeded to test the regrowth and the reversibility of aggregation and breakage in systems where an overshoot appears. This was done by starting the experiment at a rotation speed of 400 rpm until the overshoot is passed and the decay starts then the rotation speed is decreased to 200 rpm. The step changes between these two rotation speeds were repeated. Results of this experiment are shown in Fig 5.11. The solid squares represent an experiment at 200 rpm throughout and the solid triangles represent an experiment at 400 rpm throughout. The regrowth experiment is represented by the open circles. As we can see, aggregate do not grow, upon reduction of the rpm, to the same sizes attained when the experiment is run at the lower rpm from the beginning. The difference persists after many cycles of increase and decrease in the rotation speed. Such behavior supports the notion that some loss of the interparticle force accompanies the aggregation and breakage events, which supports our aforementioned hypothesis that the decay after the overshoot is due to ductile separation which cause increase in surface roughness and contact hysteresis.

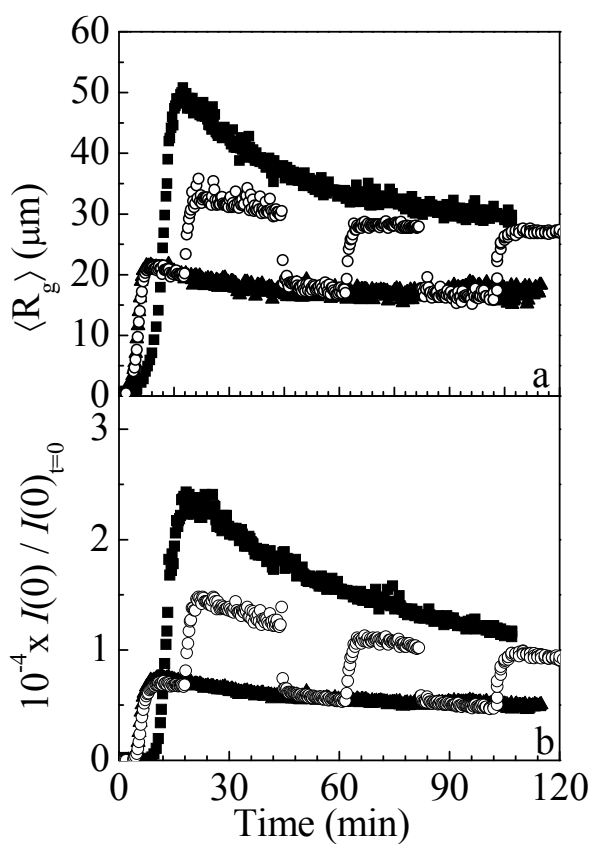


Figure 5.11: Response of average radius of gyration $\langle R_g \rangle$ (a) and normalized zero angle intensity $I(0)$ (b) to step changes in the stirring speed during aggregation of 300 nm carboxyl latex in batch experiments using a solid volume fraction of 20 ppm, at pH 5; (■)200 rpm, (○)400-200-400-200-400-200 rpm, (▲)400 rpm,

5.5. Conclusions and summery

Evidence of the strong influence of the structural forces, i.e., hydration repulsion and hydrophobic attraction, on flow-induced aggregation and breakage above the CCC are given in this work. Their influence is mainly on the interparticle forces and minimum distance, which determine the aggregate cohesive forces. This can explain the increase in aggregate sizes with the decrease in pH, or for latexes with larger area per charge group, even at salt concentrations above the CCC, where pure aggregation remains unchanged. This opens a window to manipulate the outcome of aggregation processes, in terms of average aggregate sizes, while having aggregation rate at its maximum due to having salt concentration above the CCC. Moreover, two different shapes of the time evolution curve were observed: one of them is sigmoidal while the other exhibits an overshoot in size after the initial growth period that is followed by slow decay. The transition from sigmoidal to appearance of overshoot was found to happen when the latex surface becomes more hydrophobic either due to lower pH or larger area per charge group. The appearance of the overshoot was explained as a result of the high aggregate cohesive force. The reasoning we propose is as follows. Strong aggregate cohesive forces enable the aggregate to grow to larger sizes; however the forces due to hydrodynamic stresses that break these large sizes are large enough to cause ductile separation. Thus breakage events cause deterioration in the surface and increase in the surface roughness. The increase in surfaces roughness leads to weaker interparticle forces, hence weaker aggregate cohesive forces when the fragments re-aggregate. The smaller aggregate cohesive forces mean that smaller aggregate sizes can survive. This sequence of aggregation-ductile separation- re-aggregation of rougher surfaces causes the slow decay in aggregate sizes. This decay stops when the interparticle forces and the aggregate sizes become small enough such that the hydrodynamic forces causing breakge are not large enough to induce ductile separation.

6. Comparison and experimental validation of aggregation efficiency models

6.1. Introduction

Considerable research efforts are dedicated to developing quantitative models for the rate function of flow-induced aggregation. These models are usually constructed as a product of a collision frequency, K_{ij}^{sh} , and an aggregation efficiency, α_{ij} . The collision frequency represents the rate function of flow-induced aggregation in a hypothetical situation where particle trajectories are not influenced by the presence of particles and interparticle forces are neglected, see Eq. 1.4. The aggregation efficiency accounts for these two effects. It represents the ratio between the actual aggregation rate function, which is affected by particle-fluid and particle-particle interactions, and the collision frequency. Although various models are used to represent the aggregation efficiency^{8, 11-14, 26, 71, 124-127} many of them are based on simplified empirical correlations or corrections stemming from single particle settling behavior^{127, 128}. Only three models address explicitly the effect of hydrodynamic interactions between a pair of aggregates in a flow on the aggregation efficiency using the analysis of the relative trajectories. In all of them it is assumed that the dispersion is sufficiently dilute such that multi-body interactions can be neglected. In addition, the flow around an aggregate is approximated as creeping as typically the Reynolds number on the aggregate length scale

$$\text{Re} = R^2 G / \nu \quad (6.1)$$

where R is the characteristic length of the aggregate, G is the shear rate and ν is the kinematic viscosity, is much smaller than one. Furthermore, effect of aggregate inertia can be neglected when the Stokes number $St = t_p G$, where t_p is the aggregate relaxation time defined as:

$$t_p = R^2 \left(\frac{2\rho_p}{\rho_f} + 1 \right) / 9\nu \quad (6.2)$$

where ρ_p and ρ_f are densities of the particle and the surrounding fluid, respectively, is significantly smaller than one. The Main difference between the above mentioned three models is in the treatment of the intra-aggregate flow. Adler and others^{11, 14, 32, 129} treat the aggregates as impermeable spheres, thus neglecting intra-aggregate flow in what is referred to as the

curvilinear model. On the other hand, Kusters et al.²⁶, and independently Torres et al.¹³⁰, visualize the porous aggregate as a sphere comprising impermeable core, which determines the hydrodynamic interactions, thus the aggregates' trajectories, and a completely permeable shell, which determines the collision radius. This model is referred to as the core-shell (CS) model. Recently, Bähler et al.^{8, 12} developed an aggregation efficiency model treating the aggregates as uniformly permeable spheres, which we refer to as the uniformly permeable sphere (UPS) model.

The aim of the work presented in this chapter is to assess the capabilities of these three models to describe aggregation of colloidal polymer particles in turbulent flow. First we review the different aggregation efficiency models, then we present comparisons of them against experimental data of initial aggregation kinetics obtained from batch experiments, and data of regrowth of pre-formed aggregate obtained from step experiments, see section 4.5. The data of all experiments used in this comparison is listed in Table 6.1.

6.2. Aggregation efficiency models

6.2.1. Rectilinear model and empirical fitting of a scalar efficiency

The easiest approach to model aggregation efficiency is to assume that the hydrodynamic resistance is compensated for by the van der Waals force, such that the effects of both cancel each other^{20, 70} which leads to a constant aggregation efficiency equal to one^{21, 38, 45, 70, 131}. This is equivalent to the original assumption of the rectilinear model of Smoluchowski who neglected both effects as illustrated in Fig. 6.1a. However, this point of view contradicts a considerable body of experimental data, that shows that the actual aggregation rate is a fraction of the collision frequency^{2, 9, 21, 27, 38, 42, 132}.

The simplest approach to account for this discrepancy is by introducing a uniform aggregation efficiency independent of the aggregate size, i.e., $\alpha_{ij} = \alpha$, with α as a fitting parameter. This approach is equivalent to assuming that k_0 , see Eq. 1.4, is an empirical fitting parameter. However, the inadequacy of this treatment, for a complicated physical phenomenon such as hydrodynamic retardation, leads to considerable disparity in the reported values of the prefactor. For example, Nopens et al.¹³² reported values of $k_0 \approx 0.001$ for aggregation of activated sludge, Soos et al.⁹ report values around 0.5 while fitting the data of Selomulya et al.⁷¹

for aggregation of fully destabilized polystyrene particles in turbulent Taylor-Couette flow, Kim and Kramer¹³³ report a value of 0.4 using the data of Li and Zhang¹²⁶ obtained in a jar-test device stirred with a paddle mixer, and Waldner et al.²⁷ reported values around 0.2 for aggregation of fully destabilized polystyrene particles under turbulent conditions in stirred tank fitted with Rushton impeller. Moreover, as it is clear from these studies, fitting of k_o requires experimental data of the time evolution of the CMD during the initial aggregation period, where breakage is not yet present. Such fitting requires knowledge of d_f during this early stage of aggregate growth. However, d_f cannot be accurately estimated initially because during this period of the process the CMD contains a significant portion of small non-fractal aggregates and the polydispersity of the CMD is changing²⁸. Therefore, the value of d_f together with that of the prefactor k_o are typically obtained by fitting of experimental data of the initial aggregation period²⁷. These two parameters are, however, linked in a way that many pairs of their values can be used to fit the same experimental data set without significant changes in the quality of the fit⁹. Therefore using such simplified approach depends strongly on experimental data and yields uncertain results and therefore is of little value as a predictive modeling approach.

6.2.2. Curvilinear model

In this model, the aggregation efficiency is calculated by integration of the relative velocity between two solid spheres, representing the aggregates, in a flowing fluid. The integration is repeated until the area enclosing the trajectories leading to collision, referred to as the capture area, denoted by X_c in Fig. 6.1b, is found. The system of differential equations describing this relative velocity contains two scalar functions, usually referred to as A and B ¹³⁴, to account for the disturbance of the relative velocity of the aggregates due to their interaction and for their influence on the fluid streamlines. Adler^{14, 129} calculated A and B for unequal spheres in simple shear flow where these functions depend only on the separation distance and the size ratio of the approaching spheres. Han and Lawler¹³ present a fitted correlation for the aggregation efficiency that summarizes Adler's results.

$$\alpha_{ij} = \frac{8}{(1 + \lambda_{ij})^3} 10^{(a(N_A) + b(N_A)\lambda_{ij} + c(N_A)\lambda_{ij}^2 + d(N_A)\lambda_{ij}^3)}, \quad (6.3)$$

where $\lambda_{ij} = R_{c,j}/R_{c,i}$, ($0 < \lambda_{ij} \leq 1$), $N_A = \frac{A_H}{8\mu R_{c,i}^3 G} = \frac{1}{8} i^{-3/d_f} N_F$ and a, b, c, d are functions of N_A .

Li and Zhang¹²⁶ give fitted correlations in the form of polynomials for these functions. It is important to note that these many fitted correlations and parameters are not empirical. They are essentially a compact way to represent the outcome of numerous trajectory calculations using hydrodynamic interaction functions derived by Adler^{14, 129}. Since permeability of the aggregates, and therefore intra-aggregate flow, is neglected, dependency of the aggregation efficiency function on the aggregate structure appears only implicitly via d_f in λ_{ij} , N_A and K_{ij} .

6.2.3. Core-shell model

Kusters et al²⁶ suggested that an aggregate can be envisioned as comprising an impermeable core and a completely permeable shell. The impermeable core determines the hydrodynamic interactions, thus the aggregate trajectory, while the permeable shell determines the capture area as illustrated in Fig. 6.1c. The size ratio between the impermeable core and the permeable shell depends on the aggregate structure. The more open the aggregate structure is, i.e., the smaller the value of d_f , the smaller the core-to-shell ratio becomes. In the parameterization study presented by Ducoste¹²⁵, the core radius corresponds to the hydrodynamic radius that is the radius of the solid sphere that would undergo the same drag as the aggregate, while the shell radius is represented by the collision radius of the aggregate. Hence, for a porous aggregate the collision and the hydrodynamic radii, $R_{h,i}$, are related through

$$R_{h,i} = R_{c,i} \left(\frac{1 - \xi_i^{-1} \tanh(\xi_i)}{1 + 1.5\xi_i^{-2} - 1.5\xi_i^{-3} \tanh(\xi_i)} \right), \quad (6.4)$$

where $\xi_i = R_{c,i} / \sqrt{\kappa_i}$ is the shielding ratio and κ_i is the permeability of the aggregate i . The same notion, i.e., impermeable core and a completely permeable shell, was suggested by Torres et al¹³⁰, but with a constant shielding ratio for all sizes. Happel's equation can be used to estimate the permeability

$$\kappa_i = \frac{3 - 4.5\phi_i^{1/3} + 4.5\phi_i^{5/3} - 3\phi_i^2}{9\phi_i \left(3 + 2\phi_i^{5/3} \right) C_s} 2R_p^2, \quad (6.5)$$

where $\phi_i = i^{(1-3/d_f)}$ is the solid volume fraction of an aggregate i and C_s is a coefficient to account for the contacts between primary particles within the aggregate, and for doublet it is equal to 0.7 while for triplets and larger clusters it is equal to 0.5²⁶. Having specified the core

radii, Adler's trajectory analysis can then be used to track the motion of the aggregates and find the capture area which depends on the permeability of the aggregate. Ducoste et al.¹²⁵, summarizes the results of Kusters²⁶ and gives the following semi-empirical relation for the aggregation efficiency,

$$\alpha_{ij} = \left[\left(\frac{6\pi R_{h,i}^3 (\lambda_{h,ij} + 1)^3}{8R_p^3 N_F} \right) \left(\frac{2\lambda_{h,ij} R_{h,i}}{R_p (\lambda_{h,ij} + 1)} \right) \right]^{-0.18} \quad (6.6)$$

which is, according to power equal to -0.18, strictly valid only for large size of primary particles as we have seen in chapter 4. The parameter $\lambda_{h,ij} = R_{h,j}/R_{h,i}$ characterizes the ratio between the hydrodynamic radii of colliding aggregates

6.2.4. Uniformly permeable sphere model

In this approach the permeability is introduced directly in the hydrodynamic problem of the relative motion between two porous aggregates in a flow, which is achieved by using Brinkman equation for the intra-aggregate flow⁸. Elaborating this approach leads to an expression for the relative velocity between two porous spheres representing the aggregates approaching each other, which is then used in trajectory analysis¹² to obtain the aggregation efficiency. Fitted correlations that summarize these calculations are given elsewhere¹². These correlations express the aggregation efficiency as a function of aggregates sizes, d_f , and N_F . The permeability is calculated via an empirical correlation between the permeability and d_f to describe the simulated settling data of Lattuada et al.¹⁰ calculated for aggregates produced by Monte Carlo simulation as well as the experimental data of Lasso and Weidman¹³⁵.

6.3. Comparison with experiments

The PBE presented in Eq. 1.1 was discretized using the fixed pivot method of Kumar and Ramakrishna¹³⁶. Based on the numerical sensitivity analysis by Soos et al⁶⁷, the fineness of the grid was adjusted to properly describe initial aggregation kinetics without any artifacts introduced by the numerical methods used in discretization and integration of the PBE. Moreover the size of the grid was tested by checking that no accumulation takes place in the largest pivot. The grid consisted of 281 pivots; the first 26 pivots are distributed linearly followed by a geometric grid with a geometric factor of 1.04.

Table 6.1: Experimental conditions of the experiments used in model evaluation. G is the volume averaged shear rate.

R_p nm	ϕ , ppm	rpm	G sec ⁻¹	N_F	Figure	Type of experiments
300	40	638	618	0.67	Fig. 6.2a,b,c,d	Initial growth
300	40	201	108	3.85	Fig. 6.3a,b	Initial growth
300	40	1085	1376	0.30	Fig. 6.3c,d	Initial growth
405	40	201	108	1.57	Fig. 6.4a,b	Initial growth
405	40	638	618	0.27	Fig. 6.4c,d	Initial growth
405	20	638	618	0.27		
405	10	638	618	0.27		
50	40	201	108	832	Fig. 6.5a,b	Initial growth
50	40	417	328	274	Fig. 6.5a,b	Initial growth
50	40	638-417	618-327	145-274	Fig. 6.7a,b	Regrowth
405	40	1085-201	1376-108	0.12-1.57	Fig. 6.8a,b	Regrowth

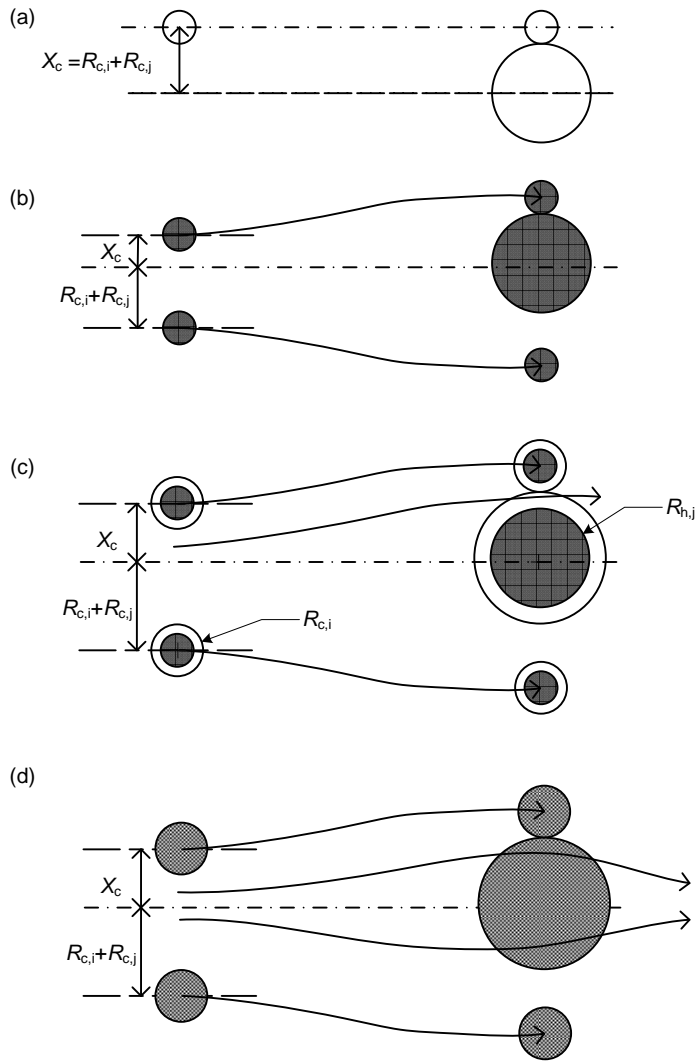


Figure 6.1 Schematic of the permeability assumptions in the different models. a) the rectilinear approach: completely permeable aggregates, the aggregation efficiency has a value of 1, b) curvilinear model, assuming impermeable spheres c) CS model, assuming impermeable core and completely permeable shell, d) UPS model, assuming uniformly permeable spheres.

As discussed earlier, d_f cannot be determined during initial growth precisely enough because of changing polydispersity and scattering by non-fractal objects. Therefore d_f was used as a fitting parameter whose value is limited to the range between 1.8 to 2.2^{27, 130, 137}. In addition to having d_f in the aforementioned range, appropriate model has to fulfill two more criteria. First, the model should predict experimental data, in terms of both measured moments of CMD, $\langle R_g \rangle$ and $I(0)$, up to a value of dimensionless time $\tau_x = tG\phi$ equal to two. This constrain is based on our previous studies²⁹ where it was shown that below this time breakage is not influential. Second criteria is that model should not under predict any of the two moments of the CMD for $\tau_x > 2$, which reflects the fact that when any of the moments is under predicted without presence of breakage, introducing it to the PBE will leads to even larger under prediction of experimental data.

6.3.1. Initial aggregation experiments

An example of the comparison of model predictions with experimental data using all above mentioned models is presented in Fig. 6.2a-d for N_F equal to 0.67 (corresponding to diameter of primary particles equal to 600 nm, and volume averaged shear rate equal to 618 sec⁻¹). As can be seen from Fig. 6.2a b when using the model of Saffman and Turner assuming completely permeable sphere with α_{ij} equal to 1 and k_o equal to 1.294 we see significant over prediction even for unrealistically large value of d_f equal to 2.8. The main reason for this over prediction is the complete omission of hydrodynamic retardation in this model. Moreover, this sever over prediction suggests that van der Waals forces cannot overcome hydrodynamic retardation in a way that each of them cancels the other. This over prediction was observed consistently for all the data sets considered in this study. An improvement can be gained by discarding the value of k_o driven from theory and using k_o as a fitting parameter. As can be seen a good agreement can be obtained in this way as shown by the solid line in Fig. 6.2 a,b, using $k_o = 0.22$ and $d_f = 1.9$. However, the introduction of another fitting parameter makes this approach heavily dependent on experiments and their quality, and thus it will not be treated further. Fig. 6.2 a,b also illustrates predictions calculated by the curvilinear model (dashed line) which however seriously under predicts the values of $\langle R_g \rangle$ and $I(0)$ for $\tau_x > 2$, even for $d_f = 1.8$ which is considered as the smallest value in flow-induced aggregation. We note that such behavior was

observed consistently for all the data sets used in this study. It suggests that neglecting permeability is not an appropriate assumption especially for aggregates of larger sizes, since the hydrodynamic retardation is substantially overestimated compared to experimental observation. From the aforementioned findings we can already draw conclusion that both the rectilinear and curvilinear model fail to predict aggregation kinetics and therefore are excluded from further discussion.

Predictions of initial kinetics for the remaining two models that incorporate permeability, the CS model and the UPS model is presented in Fig. 6.2 c, d using k_o equal to 1.29 for the CS model, plotted as dashed line, and k_o equal to 0.36 for the UPS model, illustrated as solid line. For both of them only d_f was used as fitting parameter. As can be seen both models predict correctly the experimental values of both moments up to a value of τ_x equal to 2. A noticeable aspect of the shown simulations is that each model required a different value of d_f to fit satisfactorily the same data set: $d_f = 2$ in the case of the UPS model (solid line) and $d_f = 1.8$ for the CS model (dashed line). Similar results were obtained also for other values of N_F parameters (see Figure 6.3-5). Therefore, based on the presented comparison we can conclude that both models predict the initial aggregation kinetics reasonably well and no preference to one or other model can be drawn. This suggests that a different kind of experiment has to be used to properly discriminate between the CS and the UPS models. The difference in d_f values hints that this other kind of experiment must enable accurate measurement of d_f .

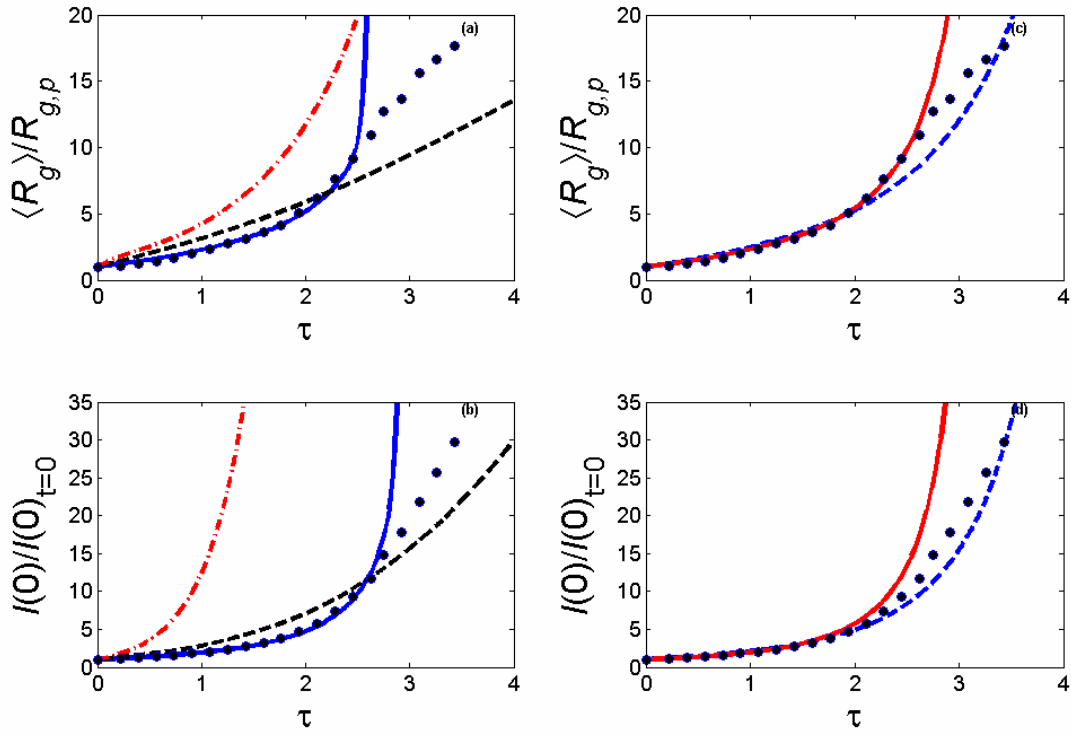


Figure 6.2: Initial growth for 600 nm latex, $N_F = 0.67$ (for details see Table 6.1). a) normalized $\langle R_g \rangle$ and b) normalized $I(0)$. Solid circles: experimental data; dashed-dotted line: collision efficiency of unity, $k_o = 1.294$, and $d_f = 2.8$; solid line: empirical fitting of $k_o = 0.22$ and $d_f = 1.9$; dashed line: curvilinear model with $d_f = 1.8$. c) normalized $\langle R_g \rangle$ and d) normalized $I(0)$. Solid circles: experimental data; solid line: UPS model with $d_f = 2.0$; dashed line: CS model with $d_f = 1.8$.

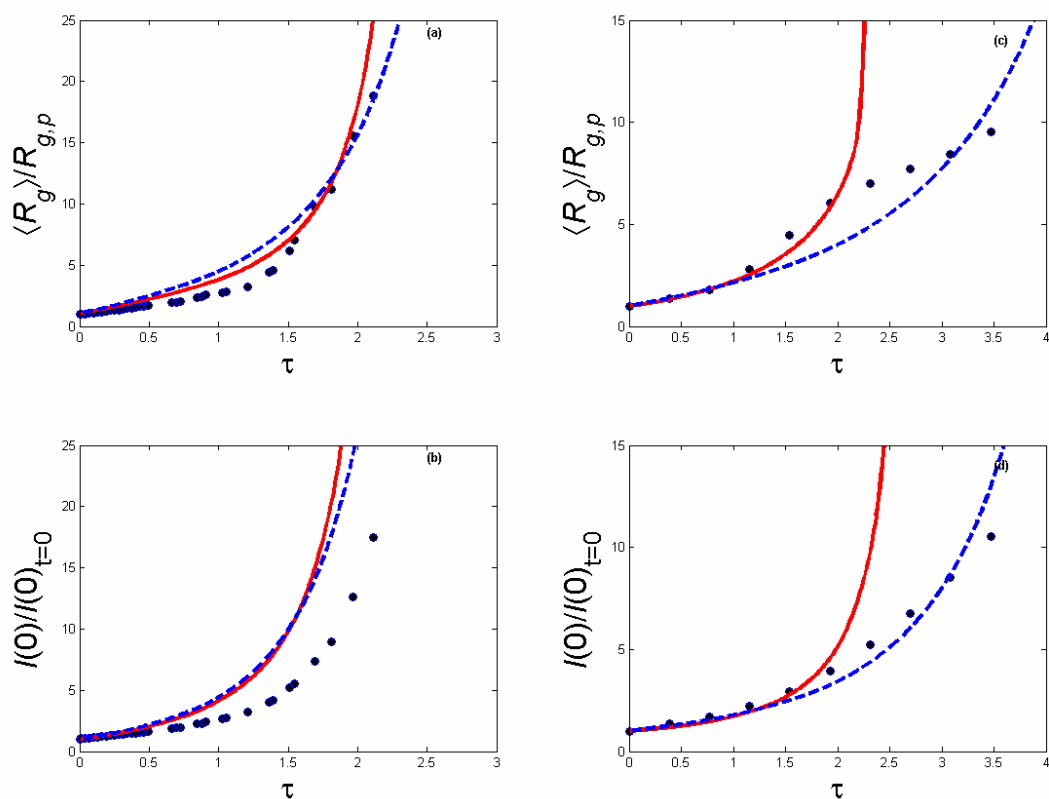


Figure 6.3: Initial growth using 600 nm latex. a) normalized $\langle R_g \rangle$ and b) normalized $I(0)$ for $N_F = 3.85$, solid circles: experimental data; solid line: UPS model $d_f = 2.0$; dashed line: CS model $d_f = 1.8$. c) normalized $\langle R_g \rangle$ and d) normalized $I(0)$ for $N_F = 0.30$, solid circles: experimental data; solid line: UPS model $d_f = 1.9$; dashed line: CS model $d_f = 1.8$.

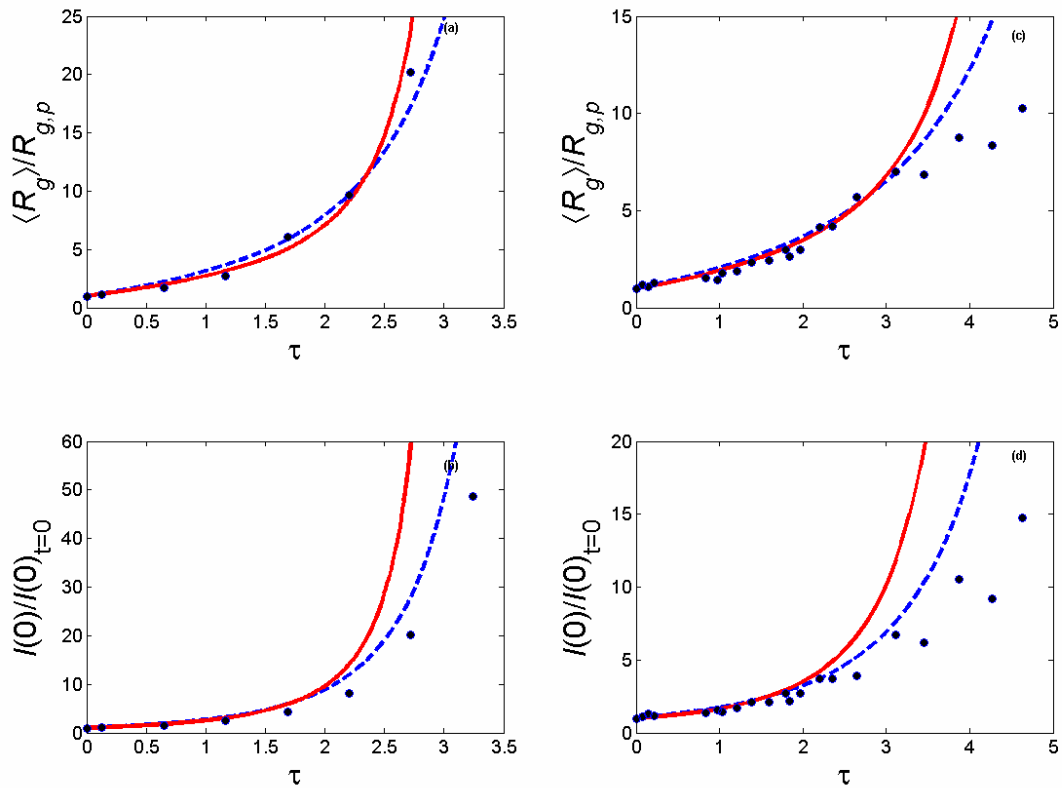


Figure 6.4: Initial growth for 810 nm latex. a) normalized $\langle R_g \rangle$ and b) normalized $I(0)$ for $N_F = 1.57$. solid circles: experimental data; solid line: UPS model, $d_f = 2.04$; dashed line: CS model $d_f = 1.80$. c) normalized $\langle R_g \rangle$ and d) normalized $I(0)$ for $N_F = 0.27$, solid circles: experimental data; solid line: UPS model, $d_f = 2.16$; dashed line: CS model $d_f = 1.84$.

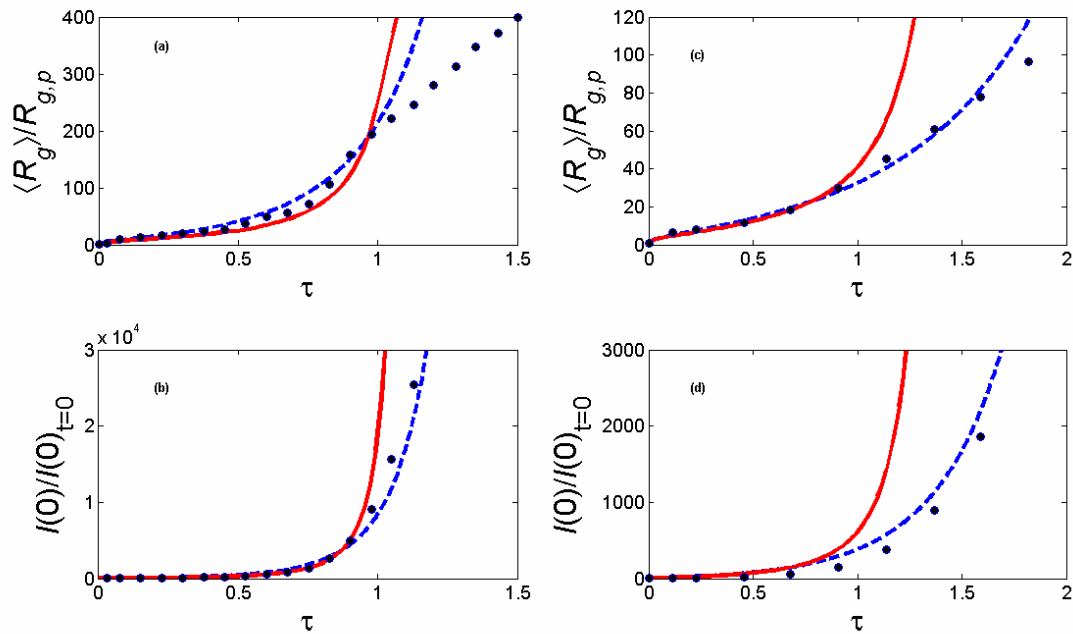


Figure 6.5: Initial growth for 100 nm latex. a) normalized $\langle R_g \rangle$ and b) normalized $I(0)$ for $N_F = 832$. solid circles: experimental data; solid line: UPS model, $d_f = 2.2$; dashed line: CS model $d_f = 2.1$. c) normalized $\langle R_g \rangle$ and d) normalized $I(0)$ for $N_F = 274$, solid circles: experimental data; solid line: UPS model, $d_f = 2.2$; dashed line: CS model $d_f = 2.1$.

6.3.2. Regrowth experiments

Given the inadequacy of initial aggregation kinetics data to discriminate between the CS and the UPS models, we used data obtained using step experiments. This data represent regrowth kinetics of aggregates previously grown at higher stirring speed after applying sudden reduction of stirring speed. The data used in the chapter were obtained for primary particles with diameters of 100 and 810 nm, see Table 6.1. Due to non RDG behavior of primary particles with d_p equal to 810 nm for which d_f cannot be determined directly from light scattering data, d_f was determined by image analysis of 2D projections of aggregates and found to be equal to 2.62 ± 0.18 independent of the rotation speed as described in details in chapter 4. The d_f value, within the experimentally measured interval, that yields the best fit of experimental data was used in comparing simulations and experiments. On the other hand, according to Ehrl et al²⁹ for size of primary particles equal to 120 nm (which are within RDG limit) aggregates growth large enough that d_f can be reliably approximated by the slope of the power-law of $S(q)$ vs q , see Fig 6.6, which is for this particular case equal to 2.7 and is constant during the regrowth as evidenced by the three $S(q)$ curves in Fig. 6.6 measured at different time instances during regrowth.

To model these experiments we proceeded as follows. First, a steady state CMD before the regrowth experiment that has the same values of $\langle R_g \rangle$ and $I(0)$ as those measured experimentally was constructed. This constructed CMD was obtained by incorporating breakage in the PBE, Eq. 1.1. The complete PBE then reads¹²

$$\frac{dN_k(t)}{dt} = \frac{1}{2} \underbrace{\sum_{i,j=1}^{k-1} K_{ij} N_i(t) N_j(t)}_{\text{Aggregation}} - N_k(t) \underbrace{\sum_{i=1}^{\infty} K_{ik} N_i(t)}_{\text{Aggregation}} - \underbrace{B_k N_k(t) + \sum_{i=k+1}^{\infty} \Gamma_{ik} B_i N_i(t)}_{\text{Breakage}} \quad (6.7)$$

where B_i is the breakage rate of aggregate i and Γ_{ik} is the daughter distribution function, i.e., the number of aggregates k formed from the breakage of an aggregate i .

In the present work, a power-law breakage kernel rate function is adopted

$$B_i = \gamma G^\lambda R_i^\nu \quad (6.8)$$

where γ , λ , ν are empirical parameters.

Babler and Morbidelli¹² provide a dimensionless form of the population balance equation in which breakage prefactor is expressed as a dimensionless parameter θ

$$\theta = \frac{4\pi\gamma R_p^\nu G^{\lambda-1}}{3k_0 \phi} \quad (6.9)$$

Thus the integration of Eq. 6.7 requires a value of θ , ν , d_f and a definition of $\Gamma_{i,k}$. in our simulations only breakage into two fragments is assumed with the size ratio between the daughter and the mother used as a fitting parameter. Table 6.2 gives the values of the parameters for the two regrowth experiments to construct CMDs with the experimentally measured values of $\langle R_g \rangle$ and $I(0)$

Table 6.2 Parameters used in constructing CMD

Parameter	100 nm latex, Fig. 6.7.	810 nm latex, Fig. 6.8
d_f	2.7	2.5
ν	3	3
θ	1.6×10^{-5}	4.2×10^{-3}
Size ratio	0.25	0.25

The constructed CMD was subsequently used as an initial condition for regrowth experiment upon lowering the stirring speed where the regrowth kinetics is dominated by aggregation. Breakage starts to influence the CMD only when the average sizes grow to be larger than the critical sizes for breakage at the lower stirring speed. Furthermore, breakage was set to zero in the regrowth experiment to avoid confounding the performance of the aggregation and breakage kernels and to exclude the influence of fitting parameters in the breakage kernel on our comparison. Setting the breakage to zero means that the calculated regrowth rate is an upper bound of the experimentally measured one, thus the calculated values of $\langle R_g \rangle$ and $I(0)$ at later times are much larger than the ones measure during the regrowth.

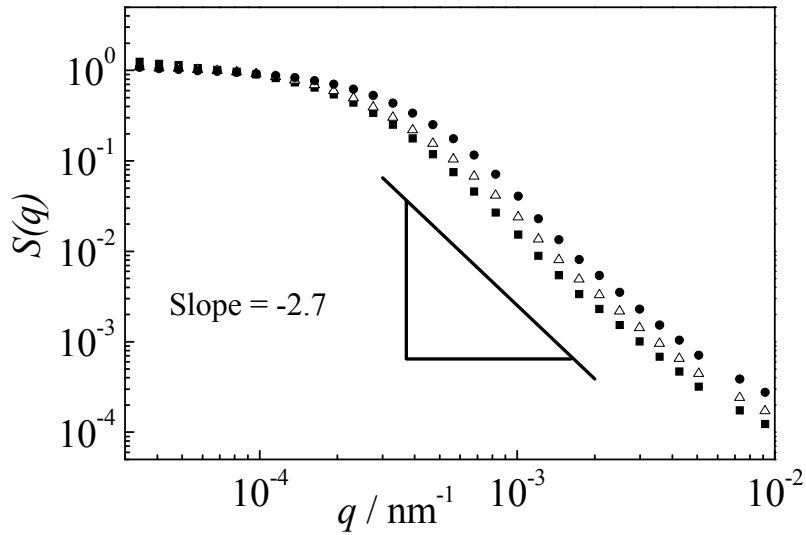


Figure 6.6: $S(q)$ vs q at three time instances during the regrowth experiment using 100nm latex: (●) first steady state before the step change in rpm corresponding to $t = 25$ min in Fig. 3, (△) an intermediate measurement during the regrowth corresponding to $t = 27.5$ min in Fig. 3 and (■) second steady state corresponding to $t = 30$ min in Fig. 3. The slope of the power-law region of $S(q)$ vs q is for all cases the same and equal to 2.7.

In Fig. 6.7 are compared the measured and calculated regrowth kinetics upon the reduction of the stirring speed from 638 rpm to 417 rpm using primary particles of 100 nm corresponding to change of N_F from 145 to 274 at $t = 27$ min. The predictions of the by UPS model are the solid line and those of the CS model are the dashed lines. d_f equal to 2.7 (see Fig. 6.8) combined with weighted exponent z in Eqs. 20 and 21 equal to 1.78, were used for both models. The difference in the models performance is striking where the CS model clearly underestimating aggregation efficiency for clusters, while agreement with predictions using the UPS model (solid line) is good. The same behavior is manifested in the comparison of regrowth kinetics for 810 nm latex shown in Fig. 6.10, where the stirring speed was reduced from 1000 rpm to 200 rpm at $t = 28$ min, corresponding to the change of N_F from 0.12 to 1.57. In the simulations of this experiment the best agreement with experiment was found with d_f equal to 2.5 as obtained from image analysis, see chapter 4 combined with weighted exponent z equal to 1.55 as measured by light scattering²⁹. Again the UPS model (solid line) shows good agreement with experiments while the CS model (dashed line) clearly underestimates the regrowth of aggregates.

From the comparison with the regrowth experiments one can conclude that the UPS model is better able to represent aggregation efficiency over the range of sizes and aggregate structures observed experimentally. The CS model, although equivalent in performance to the UPS model for the initial aggregation kinetics, significantly underestimates aggregate growth for larger aggregates. This suggests that the core-shell notion where the core radius is the hydrodynamic radius is not appropriate to describe aggregation efficiency. This can be ascribed to the fact that the hydrodynamic radius becomes very close to the collision radius with increase in the fractal dimension. Our findings also suggests that modeling the aggregate as a uniformly porous is a more realistic description and is capable of describing the experimental data examined in this study.

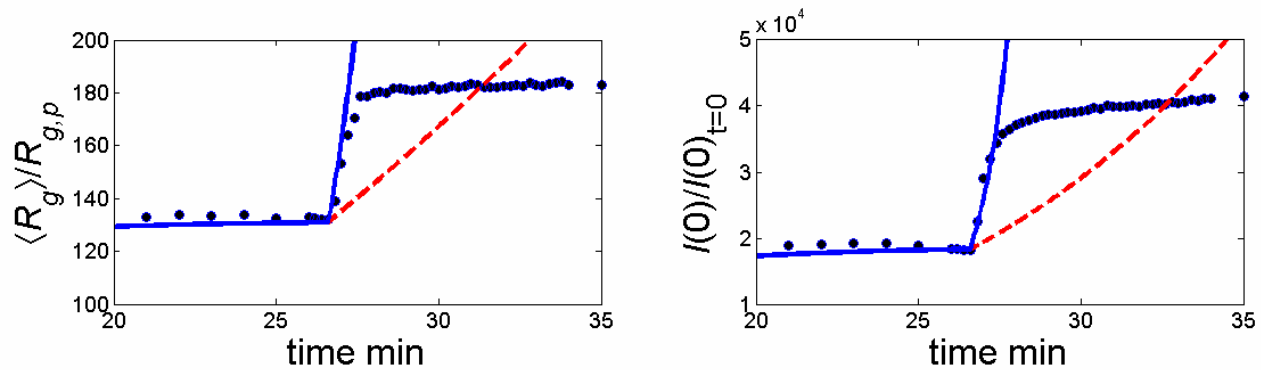


Figure 6.7: 3 Regrowth experiments using the 100 nm latex. Solid circles: experimental data; solid line: UPS model with $d_f = 2.7$; dashed line: CS model with $d_f = 2.7$. Initial aggregation until the first steady state at 638 rpm, $G = 618 \text{ sec}^{-1}$, $N_F = 145$, rotation speed was reduced afterwards to 417 rpm $G = 328 \text{ sec}^{-1}$, $N_F = 274$.

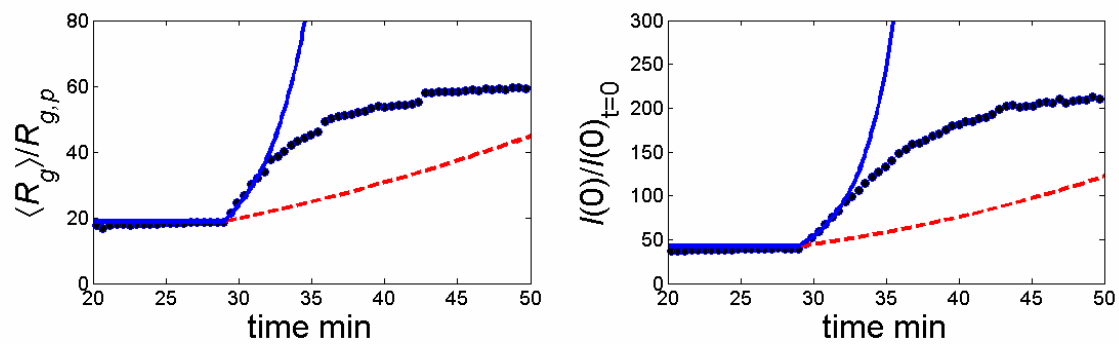


Figure 6.8: Regrowth experiments using the 810 nm latex. Solid circles: experimental data; solid line: UPS model with $d_f = 2.5$; dashed line: CS model with $d_f = 2.5$. Initial aggregation until the first steady state at 1085 rpm, $G = 1376 \text{ sec}^{-1}$, $N_F = 0.12$, rotation speed was reduced afterwards to 201 rpm $G = 108 \text{ sec}^{-1}$, $N_F = 1.57$.

6.4. Conclusions and summary

Hydrodynamic retardation and colloidal interactions play an important role in aggregation. Therefore, neglecting them and assuming an aggregation efficiency of unity fails to represent the experiments. Moreover, treating the aggregates as impermeable spheres in order to estimate the hydrodynamic retardation leads to serious under prediction of aggregation rate, due to overestimation of hydrodynamic retardation. To properly describe hydrodynamic retardation in the models of aggregation efficiency it is therefore required to incorporate the permeability of the aggregate. It was found that initial kinetics data can not be used as a base for discrimination between various models that incorporate permeability, i.e., the Core-Shell (CS) model and the Uniform permeable sphere (UPS) model. For this discrimination it is required to use another type of experiments: the regrowth experiments. In this kind of experiment the regrowth kinetics starting from a steady state distribution of aggregates upon sudden decrease in the rotation speed is measured. The value of the fractal dimension can be reliably estimated during the regrowth experiment. The comparison with this kind of experiments demonstrated clearly that the UPS model is more suitable than the CS model to model aggregation efficiency, which suggests that the assumption of a uniformly permeable sphere^{8, 12}, is closer to reality than the core-shell notion²⁶.

7. Conclusions

Experimental procedures inspired from stimulus response technique were demonstrated to be powerful, and simple, tools to study flow-induced aggregation and breakage. Using these procedures, as well as batch experiments, we could come to the following conclusions about flow-induced aggregation and breakage.

First, the steady state CMD in the system studied is controlled by dynamic equilibrium between aggregation (with second order kinetics in cluster concentration) and breakage (with first order kinetics in cluster concentration). This was revealed by the study of the dependency of the CMD on the solid volume fraction presented in chapter 3. In this chapter, we designed the dilution experiment using time scale analysis and verified the concept experimentally using various tests. This experimental procedure enables us to get the steady state CMD as a function of the solid volume fraction in one experiment. Further, dilution experiment gives us the critical aggregate size below which breakage is negligible in a given flow field by diluting to infinitesimally small concentrations. From this critical size we can estimate the aggregate cohesive forces.

Second, the structure of aggregates does not change with respect to the applied stirring speeds investigated in this work, which correspond to a volume average shear rates between 108 and 1376 sec^{-1} . This was revealed by the study of effect of the stirring speed on aggregates size and structure presented in chapter 4. In this study, we characterized the aggregate structure using the fractal dimension and the aspect ratio of the aggregates obtained from image analysis. The fractal dimension was found to be equal to 2.62 ± 0.18 , and the aspect ratio of the aggregates was in the range from 1 to 2.6 with most the aggregate having an aspect ratio around 1.4. The scaling exponent obtained from light scattering was found to be an inaccurate measure of the structure for aggregates of large particles. This study also demonstrated the reversibility of the moments of the CMD to step changes in the stirring speed. Furthermore, the ramp experiments were developed in an analogous way to the dilution experiments. From the ramp experiments and from dilution experiments conducted at various stirring speeds, It was found that the values of the rms radius of gyration obtained at steady state as well as at infinite-dilution conditions are proportional to the volume average shear rate according to $\langle R_g \rangle \propto \langle G \rangle^{-0.5}$ and the normalized

zero-angle intensities are proportional to the volume average shear rate according to $I(0)/I(0)_{t=0} \propto \langle G \rangle^{-0.7}$. This indicates that the CMDs at steady state as well as at the end of dilution are very similar in shape. Relating the values of the aggregates size under infinite dilution to the maximum values of the shear rate in the vessel leads to a size-independent aggregate cohesive force equal to 6.2 ± 1.0 nN.

Third, structural forces, i.e., hydration repulsion and hydrophobic attraction, have strong influence on flow-induced breakage even above the CCC. This was demonstrated in the experimental study presented in chapter 5. In this study batch experiments using carboxyl latexes at different pH values and using latex with different surface chemistry were conducted. These experiments showed that for the same size of primary particles, initial kinetics is not affected by the different surface chemistry of used particles. On the contrary, steady state size is strongly dependent on the surface and solution chemistries. This finding opens a window to manipulate the outcome of aggregation processes, in terms of average aggregate sizes, while having aggregation rate at its maximum due to having salt concentration above the CCC. Another important conclusion of this study was that the appearance of an overshoot in aggregate size is not due to restructuring or flow field heterogeneity; both of these hypotheses were refuted by the experiments presented in chapter 5. We postulate that this overshoot appears when the aggregate cohesive forces are high enough such that aggregate breakage is accompanied by ductile separation. We conducted an experiment to test this hypothesis; said experiment did not refute the ductile separation hypothesis.

Fourth, aggregation efficiency models must take intra-aggregate flow into account to provide realistic prediction of aggregation rate. Treating the aggregate as a uniformly permeable sphere and calculating the intra-aggregate flow according to Brinkman equation yield excellent agreement with experimental data. On the other hand, the simpler core-shell assumption was shown to be deficient as the aggregation rates calculated according to this assumption are much lower than the experimentally observed ones in the re-growth experiment.

References

1. Gregory, J., *Particles in Water Properties and Processes*. CRC Press Taylor&Francis Group: Boca Raton FL, 2006.
2. Elimelech, M.; Gregory, J.; Jia, X.; Williams, R. A., *Particle Deposition and Aggregation Measurement, Modelling and Simulation*. Butterworth-Heinemann: 1995.
3. Svarovsky, L., *Solid-Liquid Separation*. Butterworth-Heinemann: UK, 2001.
4. Hunter, R. J., *Foundations of Colloid Science*. 2 ed.; Oxford University Press: New York, 2001.
5. Melis, S.; Verduyn, M.; Storti, G.; Morbidelli, M.; Baldyga, J., Effect of fluid motion on the aggregation of small particles subject to interaction forces. *AIChE Journal* **1999**, 45, (7), 1383-1393.
6. von Smoluchowski, M., Experiments on a mathematical theory of kinetic coagulation of colloid solutions. *Zeitschrift Fur Physikalische Chemie--Stoichiometrie Und Verwandtschaftslehre* **1917**, 92, (2), 129-168.
7. Saffman, P. G.; Turner, J. S., On the Collision of Drops in Turbulent Clouds. *Journal of Fluid Mechanics* **1956**, 1, (1), 16-30.
8. Babler, M. U.; Sefcik, J.; Morbidelli, M.; Baldyga, J., Hydrodynamic interactions and orthokinetic collisions of porous aggregates in the Stokes regime. *Physics of Fluids* **2006**, 18, (1).
9. Soos, M.; Sefcik, J.; Morbidelli, M., Investigation of aggregation, breakage and restructuring kinetics of colloidal dispersions in turbulent flows by population balance modeling and static light scattering. *Chemical Engineering Science* **2006**, 61, (8), 2349-2363.
10. Lattuada, M.; Wu, H.; Morbidelli, M., Hydrodynamic radius of fractal clusters. *Journal of Colloid and Interface Science* **2003**, 268, (1), 96-105.
11. Vanni, M.; Baldi, G., Coagulation efficiency of colloidal particles in shear flow. *Advances in Colloid and Interface Science* **2002**, 97, (1-3), 151-177.
12. Babler, M. U.; Morbidelli, M., Analysis of the aggregation-fragmentation population balance equation with application to coagulation. *Journal of Colloid and Interface Science* **2007**, 316, (2), 428-441.
13. Han, M. Y.; Lawler, D. F., The (Relative) Insignificance of G in Flocculation. *Journal American Water Works Association* **1992**, 84, (10), 79-91.
14. Adler, P. M., Heterocoagulation in Shear-Flow. *Journal of Colloid and Interface Science* **1981**, 83, (1), 106-115.
15. Sorensen, C. M., Light scattering by fractal aggregates: A review. *Aerosol Science and Technology* **2001**, 35, (2), 648-687.
16. Johnson, C. S., *Laser light scattering*. Dover Publication Inc.: New York, 1990.
17. Erhl, L.; Soos, M.; Morbidelli, M., Strength, Structure, and Light Scattering Properties of Aggregates for Different Primary Particle Sizes obtained under Turbulent Conditions in Stirred Tank. *Langmuir* **accepted**.
18. Mandelbrot, B. B.; Passoja, D. E.; Paullay, A. J., Fractal Character of Fracture Surfaces of Metals. *Nature* **1984**, 308, (5961), 721-722.
19. Serra, T.; Casamitjana, X., Structure of the aggregates during the process of aggregation and breakup under a shear flow. *Journal of Colloid and Interface Science* **1998**, 206, (2), 505-511.
20. Spicer, P. T.; Keller, W.; Pratsinis, S. E., The effect of impeller type on floc size and structure during shear-induced flocculation. *Journal of Colloid and Interface Science* **1996**, 184,

(1), 112-122.

21. Spicer, P. T.; Pratsinis, S. E., Shear-induced flocculation: The evolution of floc structure and the shape of the size distribution at steady state. *Water Research* **1996**, 30, (5), 1049-1056.
22. Soos, M.; Wang, L.; Fox, R. O.; Sefcik, J.; Morbidelli, M., Population balance modeling of aggregation and breakage in turbulent Taylor-Couette flow. *Journal of Colloid and Interface Science* **2007**, 307, (2), 433-446.
23. Wang, L. G.; Vigil, R. D.; Fox, R. O., CFD simulation of shear-induced aggregation and breakage in turbulent Taylor-Couette flow. *Journal of Colloid and Interface Science* **2005**, 285, (1), 167-178.
24. Lee, C.; Kramer, T. A., Prediction of three-dimensional fractal dimensions using the two-dimensional properties of fractal aggregates. *Advances in Colloid and Interface Science* **2004**, 112, (1-3), 49-57.
25. Perry, R. H.; Green, D. W., *Perry's chemical engineers' handbook*. McGraw-Hill: New York, 1998.
26. Kusters, K. A.; Wijers, J. G.; Thoenes, D., Aggregation kinetics of small particles in agitated vessels. *Chemical Engineering Science* **1997**, 52, (1), 107-121.
27. Waldner, M. H.; Sefcik, J.; Soos, M.; Morbidelli, M., Initial growth kinetics and structure of colloidal aggregates in a turbulent coagulator. *Powder Technology* **2005**, 156, (2-3), 226-234.
28. Moussa, A. S.; Soos, M.; Sefcik, J.; Morbidelli, M., Effect of solid volume fraction on aggregation and breakage in colloidal suspensions in batch and continuous stirred tanks. *Langmuir* **2007**, 23, (4), 1664-1673.
29. Soos, M.; Moussa, A. S.; Ehrl, L.; Sefcik, J.; Wu, H.; Morbidelli, M., Effect of shear rate on aggregate size and morphology investigated under turbulent conditions in stirred tank. *Journal of Colloid and Interface Science* In Press, Accepted Manuscript.
30. Alexopoulos, A. H.; Maggioris, D.; Kiparissides, C., CFD analysis of turbulence non-homogeneity in mixing vessels - A two-compartment model. *Chemical Engineering Science* **2002**, 57, (10), 1735-1752.
31. Derksen, J.; Van den Akker, H. E. A., Large eddy simulations on the flow driven by a Rushton turbine. *AIChE Journal* **1999**, 45, (2), 209-221.
32. Brakalov, L. B., A Connection between the Orthokinetic Coagulation Capture Efficiency of Aggregates and Their Maximum Size. *Chemical Engineering Science* **1987**, 42, (10), 2373-2383.
33. Chellam, S.; Wiesner, M. R., Fluid-Mechanics and Fractal Aggregates. *Water Research* **1993**, 27, (9), 1493-1496.
34. Wiesner, M. R., Kinetics of Aggregate Formation in Rapid Mix. *Water Research* **1992**, 26, (3), 379-387.
35. Stratford, M.; Coleman, H. P.; Keenan, M. H. J., Yeast Flocculation - a Dynamic Equilibrium. *Yeast* **1988**, 4, (3), 199-208.
36. Burban, P. Y.; Lick, W.; Lick, J., The Flocculation of Fine-Grained Sediments in Estuarine Waters. *Journal of Geophysical Research-Oceans* **1989**, 94, (C6), 8323-8330.
37. Tsai, C. H.; Iacobellis, S.; Lick, W., Flocculation of Fine-Grained Lake-Sediments Due to a Uniform Shear-Stress. *Journal of Great Lakes Research* **1987**, 13, (2), 135-146.
38. Serra, T.; Casamitjana, X., Effect of the shear and volume fraction on the aggregation and breakup at particles. *AIChE Journal* **1998**, 44, (8), 1724-1730.
39. Rwei, S. P.; Manaszloczower, I.; Feke, D. L., Characterization of Agglomerate Dispersion by Erosion in Simple Shear Flows. *Polymer Engineering and Science* **1991**, 31, (8),

558-562.

40. Kobayashi, M.; Adachi, Y.; Ooi, S., Breakup of fractal flocs in a turbulent flow. *Langmuir* **1999**, 15, (13), 4351-4356.
41. Torres, F. E.; Russel, W. B.; Schowalter, W. R., Floc Structure and Growth-Kinetics for Rapid Shear Coagulation of Polystyrene Colloids. *Journal of Colloid and Interface Science* **1991**, 142, (2), 554-574.
42. Koh, P. T. L.; Andrews, J. R. G.; Uhlherr, P. H. T., Modeling Shear-Flocculation by Population Balances. *Chemical Engineering Science* **1987**, 42, (2), 353-362.
43. Spicer, P. T.; Pratsinis, S. E., Coagulation and fragmentation: Universal steady-state particle-size distribution. *AIChE Journal* **1996**, 42, (6), 1612-1620.
44. Flesch, J. C.; Spicer, P. T.; Pratsinis, S. E., Laminar and turbulent shear-induced flocculation of fractal aggregates. *AIChE Journal* **1999**, 45, (5), 1114-1124.
45. Chung, C. B.; Park, S. H.; Han, I. S.; Seo, Y. H.; Yang, B. T., Modeling of ABS latex coagulation processes. *AIChE Journal* **1998**, 44, (6), 1256-1265.
46. Zhang, J. J.; Li, X. Y., Modeling particle-size distribution dynamics in a flocculation system. *AIChE Journal* **2003**, 49, (7), 1870-1882.
47. Oles, V., Shear-Induced Aggregation and Breakup of Polystyrene Latex-Particles. *Journal of Colloid and Interface Science* **1992**, 154, (2), 351-358.
48. Serra, T.; Colomer, J.; Casamitjana, X., Aggregation and breakup of particles in a shear flow. *Journal of Colloid and Interface Science* **1997**, 187, (2), 466-473.
49. Lattuada, M.; Wu, H.; Morbidelli, M., A simple model for the structure of fractal aggregates. *Journal of Colloid and Interface Science* **2003**, 268, 106-120.
50. Selomulya, C.; Amal, R.; Bushell, G.; Waite, T. D., Evidence of shear rate dependence on restructuring and breakup of latex aggregates. *Journal of Colloid and Interface Science* **2001**, 236, (1), 67-77.
51. Selomulya, C.; Bushell, G.; Amal, R.; Waite, T. D., Aggregation mechanisms of latex of different particle sizes in a controlled shear environment. *Langmuir* **2002**, 18, (6), 1974-1984.
52. Froment, G. F.; Bischoff, K. B., *Chemical Reactor Analysis and Design*. John Wiley & Sons: New York, 1990.
53. Nienow, A. W., On impeller circulation and mixing effectiveness in the turbulent flow regime. *Chemical Engineering Science* **1997**, 52, (15), 2557-2565.
54. Marchisio, D. L.; Soos, M.; Sefcik, J.; Morbidelli, M., Role of turbulent shear rate distribution in aggregation and breakage processes. *AIChE Journal* **2006**, 52, (1), 158-173.
55. Clark, M. M.; Flora, J. R. V., Floc Restructuring in Varied Turbulent Mixing. *Journal of Colloid and Interface Science* **1991**, 147, (2), 407-421.
56. Francois, R. J., Strength of Aluminum Hydroxide Flocs. *Water Research* **1987**, 21, (9), 1023-1030.
57. Spicer, P. T.; Pratsinis, S. E.; Raper, J.; Amal, R.; Bushell, G.; Meesters, G., Effect of shear schedule on particle size, density, and structure during flocculation in stirred tanks. *Powder Technology* **1998**, 97, (1), 26-34.
58. Van De Ven, T. G. M., On the role of ion size in coagulation. *Journal of Colloid and Interface Science* **1988**, 124, (1), 138-145.
59. Brunk, B. K.; Koch, D. L.; Lion, L. W., Observation of coagulation in isotropic turbulence. *Journal of Fluid Mechanics* **1998**, 371, 81-107.
60. Zeichner, G. R.; Schowalter, W. R., Use of Trajectory Analysis to Study Stability of Colloidal Dispersions in Flow Fields. *AIChE Journal* **1977**, 23, (3), 243-254.

61. Feke, D. L.; Schowalter, W. R., The Effect of Brownian Diffusion on Shear-Induced Coagulation of Colloidal Dispersions. *Journal of Fluid Mechanics* **1983**, 133, (AUG), 17-35.
62. Brunk, B. K.; Koch, D. L.; Lion, L. W., Turbulent coagulation of colloidal particles. *Journal of Fluid Mechanics* **1998**, 364, 81-113.
63. van de Ven, T. G. M.; Mason, S. G., The microrheology of colloidal dispersions, VII. Orthokinetic doublet formation of spheres. *Colloids and Polymer Science* **1977**, 255, 468-479.
64. Sonntag, R. C.; Russel, W. B., Structure and Breakup of Flocs Subjected to Fluid Stresses .1. Shear Experiments. *Journal of Colloid and Interface Science* **1986**, 113, (2), 399-413.
65. Sonntag, R. C.; Russel, W. B., Structure and Breakup of Flocs Subjected to Fluid Stresses .2. Theory. *Journal of Colloid and Interface Science* **1987**, 115, (2), 378-389.
66. Israelachvili, J. N., *Intermolecular and Surface Forces*. Academic Press: London, 1991.
67. Soos, M.; Sefcik, J.; Morbidelli, M., Master curves for aggregation and gelation: Effects of cluster structure and polydispersity. *Industrial & Engineering Chemistry Research* **2007**, 46, (6), 1709-1720.
68. Bouyer, D.; Line, A.; Cockx, A.; Do-Quang, Z., Experimental analysis of floc size distribution and hydrodynamics in a jar-test. *Chemical Engineering Research & Design* **2001**, 79, (A8), 1017-1024.
69. Gardner, K. H.; Theis, T. L.; Young, T. C., The significance of shear stress in the agglomeration kinetics of fractal aggregates. *Water Research* **1998**, 32, (9), 2660-2668.
70. Rahmani, N. H. G.; Masliyah, J. H.; Dabros, T., Characterization of asphaltene aggregation and fragmentation in a shear field. *AIChE Journal* **2003**, 49, (7), 1645-1655.
71. Selomulya, C.; Bushell, G.; Amal, R.; Waite, T. D., Understanding the role of restructuring in flocculation: The application of a population balance model. *Chemical Engineering Science* **2003**, 58, (2), 327-338.
72. Tambo, N.; Hozumi, H., Physical Characteristics of Flocs .2. Strength of Floc. *Water Research* **1979**, 13, (5), 421-427.
73. Tolpekin, V. A.; Duits, M. H. G.; van den Ende, D.; Mellema, J., Aggregation and breakup of colloidal particle aggregates in shear flow, studied with video microscopy. *Langmuir* **2004**, 20, (7), 2614-2627.
74. Biggs, C. A.; Lant, P. A., Modelling activated sludge flocculation using population balances. *Powder Technology* **2002**, 124, (3), 201-211.
75. Coufort, C.; Bouyer, D.; Liné, A., Flocculation related to local hydrodynamics in a Taylor-Couette reactor and in a jar. *Chemical Engineering Science* **2005**, 60, 2179-2192.
76. Bouyer, D.; Coufort, C.; Liné, A.; Do-Quang, Z., Experimental analysis of floc size distributions in a 1-L jar under different hydrodynamics and physicochemical conditions. *Journal of Colloid and Interface Science* **2005**, 292, 413-428.
77. Blaser, S. The hydrodynamical effect of vorticity and strain on the mechanical stability of flocs. PhD thesis No. 12851, ETH Zurich, Zurich, 1998.
78. Blaser, S., Flocs in shear and strain flows. *Journal of Colloid and Interface Science* **2000**, 225, 273-284.
79. Blaser, S., Break-up of flocs in contraction and swirling flows. *Colloids and Surfaces A* **2000**, 166, 215-223.
80. Yeung, A. K. C.; Pelton, R., Micromechanics: A new approach to studying the strength and breakup of flocs. *Journal of Colloid and Interface Science* **1996**, 184, (2), 579-585.
81. Higashitani, K.; Inada, N.; Ochi, T., Floc breakup along centerline of contractile flow to orifice. *Colloids and Surfaces* **1991**, 56, 13-23.

82. Boller, M.; Blaser, S., Particles under stress. *Water Science and Technology* **1998**, 37, (10), 9-29.
83. Kobayashi, M., Breakup and strength of polystyrene latex flocs subjected to a converging flow. *Colloids and Surfaces A* **2004**, 235, 73-78.
84. Coufort, C.; Line, A., Forces on spherical particles in terms of upstream flow characteristics. *Chemical Engineering Research & Design* **2003**, 81, (A9), 1206-1211.
85. Pope, S. B., *Turbulent flows*. Cambridge University Press: Cambridge, 2000.
86. Thomas, D. N.; Judd, S. J.; Fawcett, N., Flocculation modelling: A review. *Water Research* **1999**, 33, (7), 1579-1592.
87. Hinze, J. O., *Turbulence, an introduction to its mechanism and theory*. McGraw-Hill: New York, 1959.
88. Hodges, C. S.; Cleaver, J. A. S.; Ghadiri, M.; Jones, R.; Pollock, H. M., Forces between polystyrene particles in water using the AFM: Pull-off force vs particle size. *Langmuir* **2002**, 18, (15), 5741-5748.
89. Kobayashi, M.; Juillerat, F.; Galletto, P.; Bowen, P.; Borkovec, M., Aggregation and charging of colloidal silica particles: Effect of particle size. *Langmuir* **2005**, 21, (13), 5761-5769.
90. Potanin, A. A.; Muller, V. M., Simulation of Aggregation During the Flow of Colloidal Dispersions. *Colloid Journal* **1995**, 57, (4), 519-525.
91. Bouyer, D.; Line, A.; Do-Quang, Z., Experimental analysis of floc size distribution under different hydrodynamics in a mixing tank. *AIChE Journal* **2004**, 50, (9), 2064-2081.
92. Serra, T.; Colomer, J.; Logan, B. E., Efficiency of different shear devices on flocculation. *Water Research* In Press, Corrected Proof.
93. Selomulya, C.; Bushell, G.; Amal, R.; Waite, T. D., Aggregate properties in relation to aggregation conditions under various applied shear environments. *International Journal of Mineral Processing* **2004**, 73, (2-4), 295-307.
94. Christenson, H. K.; Claesson, P. M., Direct measurements of the force between hydrophobic surfaces in water. *Advances in Colloid and Interface Science* **2001**, 91, (3), 391-436.
95. Ninham, B. W., On progress in forces since the DLVO theory. *Advances in Colloid and Interface Science* **1999**, 83, (1-3), 1-17.
96. Lopez-Leon, T.; Jodar-Reyes, A. B.; Bastos-Gonzalez, D.; Ortega-Vinuesa, J. L., Hofmeister effects in the stability and electrophoretic mobility of polystyrene latex particles. *Journal of Physical Chemistry B* **2003**, 107, (24), 5696-5708.
97. Israelachvili, J.; Wennerstrom, H., Role of hydration and water structure in biological and colloidal interactions. *Nature* **1996**, 379, (6562), 219-225.
98. Gruy, F.; Cournil, M.; Cugniet, P., Influence of nonwetting on the aggregation dynamics of micronic solid particles in a turbulent medium. *Journal of Colloid and Interface Science* **2005**, 284, (2), 548-559.
99. Song, S. X.; Lopez-Valdivieso, A.; Reyes-Bahena, J. L.; Bermejo-Perez, H. I.; Trass, O., Hydrophobic flocculation of galena fines in aqueous suspensions. *Journal of Colloid and Interface Science* **2000**, 227, (2), 272-281.
100. Le Berre, F.; Chauveteau, G.; Pefferkorn, E., Perikinetic and orthokinetic aggregation of hydrated colloids. *Journal of Colloid and Interface Science* **1998**, 199, (1), 1-12.
101. Lazar, L.; Hesp, S. A. M., Controlled aggregation of polymer latices part 3. Influence of temperature and surface chemistry. *Particulate Science and Technology* **2000**, 18, (2), 143-162.
102. Vakarelski, I. U.; Higashitani, K., Dynamic features of short-range interaction force and

adhesion in solutions. *Journal of Colloid and Interface Science* **2001**, 242, (1), 110-120.

103. Vakarelski, I. U.; Ishimura, K.; Higashitani, K., Adhesion between silica particle and mica surfaces in water and electrolyte solutions. *Journal of Colloid and Interface Science* **2000**, 227, (1), 111-118.

104. Manciu, M.; Ruckenstein, E., Role of the hydration force in the stability of colloids at high ionic strengths. *Langmuir* **2001**, 17, (22), 7061-7070.

105. Huang, H. H.; Manciu, M.; Ruckenstein, E., The effect of surface dipoles and of the field generated by a polarization gradient on the repulsive force. *Journal of Colloid and Interface Science* **2003**, 263, (1), 156-161.

106. Pantina, J. P.; Furst, E. M., Colloidal aggregate micromechanics in the presence of divalent ions. *Langmuir* **2006**, 22, (12), 5282-5288.

107. Mathur, S.; Singh, P.; Moudgil, B. M., Advances in selective flocculation technology for solid-solid separations. *International Journal of Mineral Processing* **2000**, 58, (1-4), 201-222.

108. van Oss, C. J.; Giese, R. F., Role of the properties and structure of liquid water in colloidal and interfacial systems. *Journal of Dispersion Science and Technology* **2004**, 25, (5), 631-655.

109. Swanton, S. W., Modeling Colloid Transport in Groundwater - the Prediction of Colloid Stability and Retention Behavior. *Advances in Colloid and Interface Science* **1995**, 54, 129-208.

110. Israelachvili, J. N., Adhesion Forces between Surfaces in Liquids and Condensable Vapors. *Surface Science Reports* **1992**, 14, (3), 109-159.

111. Grasso, D.; Subramaniam, K.; Butkus, M.; Strevett, K.; Bergendahl, J., A review of non-DLVO interactions in environmental colloidal systems. *Reviews in Environmental Science and Biotechnology* **2002**, 1, (1), 17-38.

112. DelgadoCalvoFlores, J. M.; PeulaGarcia, J. M.; MartinezGarcia, R.; CallejasFernandez, J., Experimental evidence of hydration forces between polymer colloids obtained by photon correlation spectroscopy measurements. *Journal of Colloid and Interface Science* **1997**, 189, (1), 58-65.

113. Valle-Delgado, J. J.; Molina-Bolivar, J. A.; Galisteo-Gonzalez, F.; Galvez-Ruiz, M. J., Study of the colloidal stability of an amphoteric latex. *Colloid and Polymer Science* **2003**, 281, (8), 708-715.

114. Hiemstra, T.; Van Riemsdijk, W. H., On the relationship between charge distribution, surface hydration, and the structure of the interface of metal hydroxides. *Journal of Colloid and Interface Science* **2006**, 301, (1), 1-18.

115. Kataoka, S.; Gurau, M. C.; Albertorio, F.; Holden, M. A.; Lim, S. M.; Yang, R. D.; Cremer, P. S., Investigation of water structure at the TiO₂/aqueous interface. *Langmuir* **2004**, 20, (5), 1662-1666.

116. Walz, J. Y., The effect of surface heterogeneities on colloidal forces. *Advances in Colloid and Interface Science* **1998**, 74, 119-168.

117. Johnson, K. L., Mechanics of adhesion. *Tribology International* **1998**, 31, (8), 413-418.

118. Schaefer, D. M.; Carpenter, M.; Gady, B.; Reifenberger, R.; Demejo, L. P.; Rimai, D. S., Surface-Roughness and Its Influence on Particle Adhesion Using Atomic-Force Techniques. *Journal of Adhesion Science and Technology* **1995**, 9, (8), 1049-1062.

119. Schmitt, F. J.; Ederth, T.; Weidenhammer, P.; Claesson, P.; Jacobasch, H. J., Direct force measurements on bulk polystyrene using the bimorph surface forces apparatus. *Journal of Adhesion Science and Technology* **1999**, 13, (1), 79-96.

120. Du, Y.; Chen, L.; McGruer, N. E.; Adams, G. G.; Etsion, Z., A finite element model of

loading and unloading of an asperity contact with adhesion and plasticity. *Journal of Colloid and Interface Science* **2007**, 312, (2), 522-528.

121. Podczeczek, F., *Particle-particle Adhesion in Pharmaceutical Powder Handling*. Imperial College Press: London, 1998.

122. Reitsma, M.; Craig, V.; Biggs, S., Elasto-plastic and visco-elastic deformations of a polymer sphere measured using colloid probe and scanning electron microscopy. *International Journal of Adhesion and Adhesives* **2000**, 20, (6), 445-448.

123. Maugis, D.; Pollock, H. M., Surface Forces, Deformation and Adherence at Metal Microcontacts. *Acta Metallurgica* **1984**, 32, (9), 1323-1334.

124. Adler, P. M., Streamlines in and around Porous Particles. *Journal of Colloid and Interface Science* **1981**, 81, (2), 531-535.

125. Ducoste, J., A two-scale PBM for modeling turbulent flocculation in water treatment processes. *Chemical Engineering Science* **2002**, 57, (12), 2157-2168.

126. Li, X. Y.; Zhang, J. J., Numerical simulation and experimental verification of particle coagulation dynamics for a pulsed input. *Journal of Colloid and Interface Science* **2003**, 262, (1), 149-161.

127. Thill, A.; Moustier, S.; Aziz, J.; Wiesner, M. R.; Bottero, J. Y., Flocc restructuring during aggregation: Experimental evidence and numerical simulation. *Journal of Colloid and Interface Science* **2001**, 243, (1), 171-182.

128. Veerapaneni, S.; Wiesner, M. R., Hydrodynamics of fractal aggregates with radially varying permeability. *Journal of Colloid and Interface Science* **1996**, 177, (1), 45-57.

129. Adler, P. M., Interaction of Unequal Spheres .1. Hydrodynamic Interaction - Colloidal Forces. *Journal of Colloid and Interface Science* **1981**, 84, (2), 461-474.

130. Torres, F. E.; Russel, W. B.; Schowalter, W. R., Flocc structure and growth kinetics for rapid shear coagulation of polystyrene colloids. *Journal of Colloid and Interface Science* **1991**, 142, (2), 554-574.

131. Sommer, M.; Stenger, F.; Peukert, W.; Wagner, N. J., Agglomeration and breakage of nanoparticles in stirred media mills - a comparison of different methods and models. *Chemical Engineering Science* **2006**, 61, (1), 135-148.

132. Nopens, I.; Koegst, T.; Mahieu, K.; Vanrolleghem, P. A., PBM and activated sludge flocculation: From experimental data to calibrated model. *AIChE Journal* **2005**, 51, (5), 1548-1557.

133. Kim, J.; Kramer, T. A., Adjustable discretized population balance equations: Numerical simulation and parameter estimation for fractal aggregation and break-up. *Colloids and Surfaces a-Physicochemical and Engineering Aspects* **2007**, 292, (2-3), 173-188.

134. Batchelor, G. K.; Green, J. T., Hydrodynamic Interaction of 2 Small Freely-Moving Spheres in a Linear Flow Field. *Journal of Fluid Mechanics* **1972**, 56, (NOV28), 375-&.

135. Lasso, I. A.; Weidman, P. D., Stokes Drag on Hollow Cylinders and Conglomerates. *Physics of Fluids* **1986**, 29, (12), 3921-3934.

136. Kumar, S.; Ramkrishna, D., On the solution of population balance equations by discretization .2. A moving pivot technique. *Chemical Engineering Science* **1996**, 51, (8), 1333-1342.

137. Torres, F. E.; Russel, W. B.; Schowalter, W. R., Simulations of coagulation in viscous flows. *Journal of Colloid and Interface Science* **1991**, 145, (1), 51-73.

CURRICULUM VITAE

EDUCATION

- III. Qualification **Dr. Sc.** ETH Zurich
- Institute Swiss Federal Institute of Technology Zurich.
 - Dates March 2004- February 2008.
 - Thesis **Experimental Investigation and Population Balance Modeling of Aggregation and Breakage of Polymer Colloids in Turbulent Flow.**
- II. Qualification **DEA**, Diploma of Advanced Studies, in Chemical Engineering
- Institute Rovira i Virgili University, School of Chemical Engineering, Spain.
 - Dates October 2001- October 2003.
 - Dissertation **Conceptual Design of Azeotropic Distillation Sequences**
- I. Qualification **B. Eng (Hons)** in Chemical Engineering. (5-yr. Curriculum)
- Institute Cairo University, Faculty of Engineering, Egypt.
 - Dates September 1995-July 2000.
 - Dissertation **Production of Methanol from Natural Gas: Process Design and Methanol Synthesis Loop Design and Optimization.**

WORK EXPERIENCE

- III. Employer Procter & Gamble Service GmbH
- Position Research engineer
 - Dates April 2008-onward
- II. Employer ETH Zürich, Institut Für Chemie- und Bioingenieurwissenschaften.
- Position PhD student/Teaching assistant
 - Dates March 2004 - March 2008
- I. Employer Central Metallurgical Research and Development Institute, Egypt.
- Position Research assistant.
 - Dates September 2000-June 2001.

PUBLICATIONS IN PEER-REVIEWED JOURNALS

- 1- A. S. Moussa, L. Jiménez “**Entrainer Selection and Systematic Design of Heterogeneous Azeotropic Distillation Flowsheets**” *Ind. Eng. Chem. Res.* 2006, 45, 4304-4315.
- 2- A. S. Moussa, M. Soos, J. Sefcik, M. Morbidelli “**Effect of Solid Volume Fraction on Aggregation and Breakage of Colloidal Suspensions in Batch and Continuous Stirred Tank**” *LANGMUIR*, 2007, 23, 1664-1673.
- 3- M. Soos, A. S. Moussa, L. Ehrl, J. Sefcik, H. Wu, M. Morbidelli “**Effect of Shear Rate on Aggregate Size and Morphology under Turbulent Conditions in Stirred Tank**” *J. Colloid Interface Sci*, 2008, 319, 577-589
- 4- M. Soos, A. S. Moussa, L. Ehrl, J. Sefcik, H. Wu, M. Morbidelli “**Dynamic Response Studies on Aggregation and Breakage Dynamics of Colloidal Dispersions in Stirred Tank**” *Journal of Dispersion Science & Technology*, accepted for publication 2008.

- 5- A. S. Moussa, M. U. Bähler, M. Soos, M. Morbidelli “**Comparison and Experimental Validation of Aggregation Efficiency Models**” submitted to *J. Colloid Interface Sci.*
- 6- A. S. Moussa, M. Soos, M. Lattuada, M. Morbidelli “**Effect of pH on Flow-induced Aggregation of Fully-Destabilized Polystyrene Latex**” manuscript in preparation.

COMMUNICATIONS IN INTERNATIONAL CONFERENCES

- 1- A. S. Moussa, L. Ehrl, M. Soos, M. Lattuada, M. Morbidelli “**Influence of structural forces and contact hysteresis on flow-induced aggregation and breakage of polymer nanoparticles**”, 11th NSTI Nanotech 2008, 1-5.6.2008, Boston-USA.
- 2- A. S. Moussa, L. Ehrl, M. Soos, M. Lattuada, M. Morbidelli “**Effect of pH on Flow-induced Aggregation of Fully-Destabilized Polystyrene Latex**” AICHE international annual meeting, 4-9.11. 2007, Salt Lake city-USA.
- 3- L. Ehrl, M. Soos, A. S. Moussa and M. Morbidelli “**Characterizing Steady-State Size And Structure Of Aggregates Outside The Limits Of The Rayleigh-Debye-Gans Theory With Small-Angle Static Light Scattering And Image Analysis**” AICHE international annual meeting, 4-9.11.2007, Salt Lake city-USA.
- 4- L. Ehrl, M. Soos, A. S. Moussa, and M. Morbidelli “**Effect Of Primary Particle Size On Steady-State Aggregates Size And Structure Under Turbulent Conditions In Stirred Tank**” AICHE international annual meeting, 4-9.11.2007 , Salt Lake city-USA.
- 5- A. S. Moussa, M. U. Bähler, M. Soos, M. Morbidelli “**Comparison and Experimental Validation of Aggregation Efficiency Models**” 21st Conference of the European Colloid and Interface Society, 10-14.9.2007, Geneva-Switzerland.
- 6- M. Soos, A. S. Moussa, L. Ehrl, J. Sefcik, H. Wu, and M. Morbidelli “**Aggregation and Breakage of Nanoparticle Clusters under Various flow conditions**” PARTEC 2007, 27-29.3.2007, Nuremberg-Germany.
- 7- M. Soos, A. S. Moussa, L. Ehrl, J. Sefcik, H. Wu, and M. Morbidelli “**Dynamic Response Studies of Aggregation and Breakage Dynamics in Colloidal Dispersions in Stirred Tanks.**” 1st International Conference on Industrial Processes for Nano and Micro Products, 03.04.-04.04.2007, London, UK
- 8- A. S. Moussa, M. Soos, J. Sefcik, M. Morbidelli “**Aggregation and Breakage of Polystyrene Particles under Turbulent Conditions: Dynamic Experiments**” 5th World Congress on Particle Technology, 23-27.4. 2006, Orlando-USA.
- 9- A. S. Moussa, L. Jiménez “**Synthesis and Optimization of Pressure Swing Distillation Sequences**” 16th International Congress of Chemical and Process Engineering, 22-26.8.2004, Prague - Czech Republic.
- 10- A. S. Moussa, L. Jiménez “**Synthesis of Heterogeneous Distillation Sequences: General Procedure and Case Studies**” 16th International Congress of Chemical and Process Engineering, 22-26.8.2004, Prague - Czech Republic.

I would like to express my appreciation of the Swiss nation for building and sustaining this magnificent school, and for keeping it open to people from all around the globe.

